Multi-scale modelling of rainfall hazard and related uncertainties - Application to the Cévennes region

Victor Melese

Communauté
UNIVERSITÉ Grenoble Alpes

THÈSE

Pour obtenir le grade de

DOCTEUR DE LA COMMUNAUTÉ UNIVERSITÉ GRENOBLE ALPES

Spécialité : **Océan, Atmosphère, Hydrologie (CEOAH)**

Arrêté ministériel : 25 mai 2016

Présentée par

Victor MÉLÈSE

Thèse dirigée par **Juliette BLANCHET**

préparée au sein du **Institut des Geosciences de l'Environnment**
dans l'Ecole Doctorale **Terre Univers Environnement**

Modélisation multi-échelle de l'aléa pluviométrique et incertitudes associées - Application à la région des Cévennes.

Thèse soutenue publiquement le **15 février 2019**,
devant le jury composé de :

Juliette BLANCHET
Chargée de Recherche, Institut des Geosciences de l'Environnment, Grenoble, Directeur de thèse

Christian ONOF
Maître de conférence, Imperial College London, Rapporteur

Mathieu RIBATET
Maître de conférence, Université de Montpellier, Rapporteur

Anne-Catherine FAVRE
Professeure, Institut National Polytechnique de Grenoble (G-INP), Présidente

Benjamin RENARD
Chargé de recherche, Institut national de recherche en sciences et technologies pour l'environnement et l'agriculture (IRSTEA) Lyon, Examinateur

Mathieu VRAC
Directeur de recherche, Laboratoire des Sciences du Climat et de l'Environnement (LSCE), Saclay, Examinateur

Résumé

La thèse présentée s'intéresse à la modélisation de l'aléa pluviométrique dans la région du Sud-Est de la France centrée sur les Cévennes. Cette région connait régulièrement des crues rapides et très localisées appelées crues éclair qui ont des impacts socio-économiques considérables. Une mesure statistique de l'aléa est la fréquence d'occurrence ou, de manière équivalente, la période de retour. La pluie étant un phénomène qui s'accumule non uniformément dans le temps et dans l'espace, l'aléa pluviométrique est une variable multi-échelle. Ainsi, cette thèse vise à en proposer une modélisation intégrée pour la région du Sud-Est de la France, c'est à dire valide pour le continuum d'échelles spatio-temporelles.

Une première difficulté liée à la modélisation de l'aléa pluviométrique pour le continuum d'échelles est qu'elle nécessite de modéliser la distribution statistique des extrêmes pluviométriques pour toute échelle alors que seules certaines échelles sont échantillonnées, aussi bien en temps qu'en espace. Plusieurs études ont démontré que la pluie possède des propriétés fractales. Les modèles dits d'invariance par changement d'échelle résultent de ces propriétés et sont donc basées sur des hypothèses physiques. Ils proposent des relations entre les différentes distributions d'intensités maximales correspondantes à différentes échelles spatio-temporelles.

Une seconde difficulté liée à la modélisation de l'aléa pluviométrique est le fait que les périodes de retour d'intérêt sont souvent de l'ordre de quelques centaines d'années alors que les séries temporelles pluviométriques à disposition sont souvent bien plus courtes. Ainsi la quantification de l'aléa pluviométrique nécessite une extrapolation à l'aide de modèles statistiques. Ces modèles n'étant pas parfaits, les incertitudes liées à leur estimation doivent être quantifiées pour éviter une sous-estimation de l'aléa pluviométrique.

Cette thèse vise donc à proposer un cadre d'estimation de l'aléa pluviométrique basé sur les propriétés d'invariance de la pluie, valide pour le continuum d'échelles spatio-temporelles, et permettant une quantification des incertitudes liées aux estimations des périodes et niveaux de retour.

Après une introduction générale de la problématique au Chapitre I, le Chapitre II se concentre sur l'étude de l'aléa pluviométrique pour le continuum d'échelles temporelles. Les relations Intensité-Durée-Fréquence (IDF) lient l'intensité, l'échelle d'agrégation temporelle et la période de retour. Un modèle IDF basé sur une hypothèse d'invariance par changement d'échelle, appelée *simple scaling*, et couplé à une loi de valeurs extrêmes généralisée (GEV) est considéré. Ce modèle permet notamment d'obtenir des estimations de niveaux de retour pour le continuum d'échelles temporelles et de périodes de retour. Deux cadres d'estimation de ce modèle sont comparés. Le premier est un cadre fréquentiste dans lequel les estimations sont obtenues par maximum de vraisemblance et les incertitudes sont obtenues grâce (i) à la normalité asymptotique de l'estimateur par maximum de vraisemblance et (ii) par une méthode de rééchantillonnage. Le second est un cadre bayésien dans lequel les estimations et les incertitudes sont directement obtenues à partir de la loi *a posteriori*. Ces deux cadres sont appliqués en 406 pluviomètres horaires couvrant une région d'environ 100 000 km^2 situé dans le Sud-Est de la France incluant les Cévennes. Le modèle et les incertitudes associées sont estimées en chaque pluviomètre pour la gamme d'échelle temporelle allant de 3 h à 120 h et pour la période 1980-2015. Les résultats montrent que le cadre bayésien est le cadre d'inférence le plus propice à la quantification de l'aléa pluviométrique notamment car l'estimation des incertitudes y est plus flexible et plus stable au nombre de données que dans le cadre fréquentiste.

Dans le Chapitre III la dimension surfacique est ajoutée. Une extension des relations IDF sont les relations Intensité-Durée-Aire-Fréquence (IDAF) dans lesquelles la dimension surfacique est prise en compte. Un nouveau modèle IDAF couplé à une loi de Gumbel est proposé. Ce modèle se base sur des hypothèses d'invariance par changement d'échelle surfacique et temporelle et propose une relation entre les différentes distributions d'intensités maximales correspondantes à différentes échelles spatio-temporelles. Un outil intrinsèque aux relations IDAF est le coefficient d'abattement spatial appelé ARF (pour *Areal Reduction Factor*). Pour une durée fixée, il caractérise le changement de la distribution des intensités maximales pluviométriques lorsque la surface augmente. Ce modèle est appliqué à des réanalyses radar couvrant une région d'environ 13 000 km^2, centrée sur les Cévennes, sur la période 2008-2015. Il est estimé en chaque pixel pour les échelles surfaciques allant de 1 km^2 à 2025 km^2 et pour les échelles temporelles allant de 3 h à 48 h. Malgré des incertitudes liées à l'échantillonnage des événements de convection profonde dans la plaine, l'étude permet de distinguer différents régimes de pluies extrêmes surfaciques sur la partie montagneuse de notre région d'étude ainsi que de quantifier l'aléa pluviométrique surfacique soulignant que celui-ci est fortement dépendant des échelles considérées.

Enfin, le Chapitre IV propose un cadre d'analyse multi-échelle de l'aléa pluviométrique lié à un événement donné, encore appelé, par anglicisme, la sévérité d'un événement. La sévérité en une localisation donnée est définie comme la période de retour de cet événement lorsqu'on considère des cumuls centrés en cette localisation pour le continuum d'échelles spatio-temporelles. Un nouveau cadre de modélisation de la sévérité liée aux événements extrêmes pluviométriques est proposé. Il étend le modèle de la seconde partie à un cadre bayésien permettant, notamment, le calcul des incertitudes liées à l'estimation de la sévérité. Ce cadre est appliqué en deux pixels situés à quelques kilomètres de distance, le premier sur la crête le second sur le plateau, pour les gammes d'échelle allant de 1 km^2 à 2025 km^2 et de 3 h à 48 h. La sévérité des événements les plus rares, apparus pendant notre période d'observation, est étudiée en ces deux pixels. L'aspect bayésien de ce cadre

permet de mettre en évidence l'apport de la prise en compte des incertitudes pour éviter une sous-estimation de la sévérité de ces événements. Enfin, la forte variabilité de la sévérité à la fois à courtes distances et pour le continuum d'échelles spatio-temporelles, en un lieu donné, est soulignée.

Table des matières

Chapitre I

Introduction

1. La région des Cévennes : une région au risque hydro-météorologique élevé.

La région d'étude (Fig. I.1) est la région située au sud de la France comprenant principalement les départements de l'Hérault, du Gard, de la Lozère, de l'Ardèche et de la Haute Loire. Le Massif Central, à l'ouest, dont les principaux sommets (à environ 1500 mètres d'altitudes) sont le Mont Aigoual, le Mont Lozère, le Serre de la Croix de Bauzon et le Mont Mézenc, est le principale massif de cette région. Il est caractérisé par sa crête - appelée crête des Cévennes - sur laquelle les vents en provenance de la Méditerranée, au sud, se heurtent. A l'est, le relief des pré-Alpes constitue le second massif de notre région d'étude. Cependant dans la fenêtre de notre région, l'altitude de ce massif ne dépasse pas les 500 mètres et, du fait de son orientation nord-sud, ne subit pas autant les vents méditerranéens que la crête des Cévennes. Trois éléments géographiques sont disposés en forme d'entonnoir : l'embouchure formée par la Méditerranée au sud, la crête des Cévennes et les pré-alpes cloisonnant la région en un bec autour de la ville de Valence. Ce cloisonnement favorise la stabilisation de flux d'air humide et chaud en provenance de la Méditerranée qui sont typique de situations météorologiques appelées systèmes convectifs de méso-échelle (SCM). Les situations engendrant des événements extrêmes pluviométriques résultent de l'interaction entre ces SCM et la topographie.

Plus précisément, deux grandes situations propices au déclenchement de systèmes précipitants peuvent être décrites. La première concerne principalement le piémont, en amont de la crête des Cévennes. Le massif des Cévennes permet la stabilisation et la convergence des flux d'air chaud, donc très instables, en provenance de la Méditerranée. Cette situation est illustrée sur le panneau de gauche de la Fig. I.2 avec la déviation des flux méditerranéens convergeant vers de nouveaux

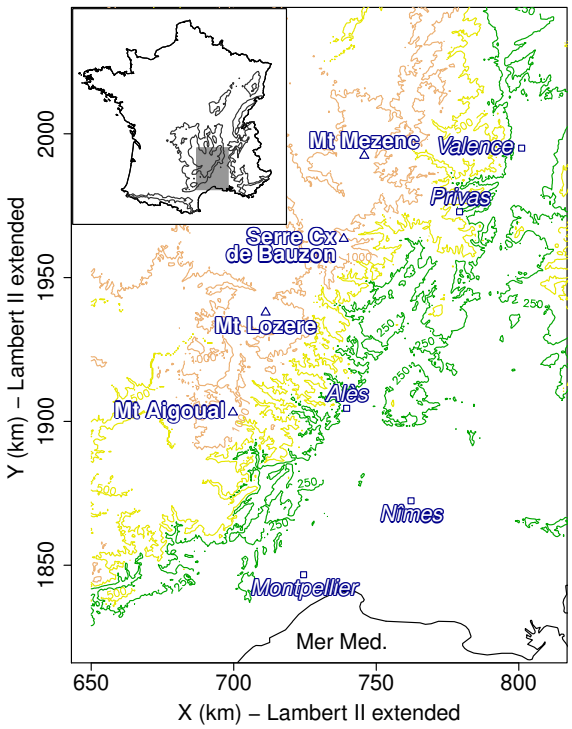

FIGURE I.1 – Carte de la région d'étude avec ses principaux sommets (triangles) et ses principales villes (triangle). Le relief est représenté avec les courbes de niveau 250 (vert), 500 (jaune) et 1000 (marron) mètres au dessus du niveau de la mer.

flux en des points où l'atmosphère devient très instable. Ce mécanisme favorise le déclenchement de systèmes de convection profonde qui sont caractérisés par des précipitations très intenses, pouvant durer quelques heures. Le panneau de gauche de la Fig. I.3 illustre un tel système en montrant le cumul de précipitation le 7 septembre 2010, entre 13h et 14h. On remarque que les plus fortes précipitations de ce système ($>$ 30 millimètres) ont une forme caractéristique en V, orientée sud-ouest nord-est. Cette organisation en V est caractéristique d'un système convectif dont les cellules se régénèrent : les cellules orageuses naissent à la pointe de V, se développent en se propageant vers le haut du V puis meurent alors que d'autres se recréent à la pointe du V. Des études météorologiques, montrant la diversité des causes menant à la formation de systèmes précipitants dans le piémont Cévennol, ont été conduites dans Gaume et al. (2004); Delrieu et al. (2005); Nuissier et al. (2008); Ducrocq et al. (2008); Bousquet et al. (2013).

La seconde situation concerne principalement la crête des Cévennes. L'interaction entre des détails de la topographie de cette crête et les flux en provenance de la Méditerranée, engendre la formation de systèmes précipitants organisés en bandes orientées nord-sud. Le panneau de droite de la Fig. I.2 illustre ce point avec un flux en provenance du sud rencontrant un obstable (cet obstable peut être par exemple le Mont Aigoual qui est un sommet assez isolé). Une première partie du flux est bloquée par l'obstacle, l'obligeant à prendre de l'altitude et engendrant un premier soulèvement d'air appelé orographique. Une seconde partie du flux contourne l'obstacle rencontrant la première partie derrière l'obstacle engendrant un soulèvement par convergence. Ce mécanisme permet la formation de systèmes précipitants organisés en bandes. Ces systèmes sont caractérisés par une convection moins profonde que les systèmes du piémont, et une stationnarité temporelle de l'ordre de plusieurs jours.

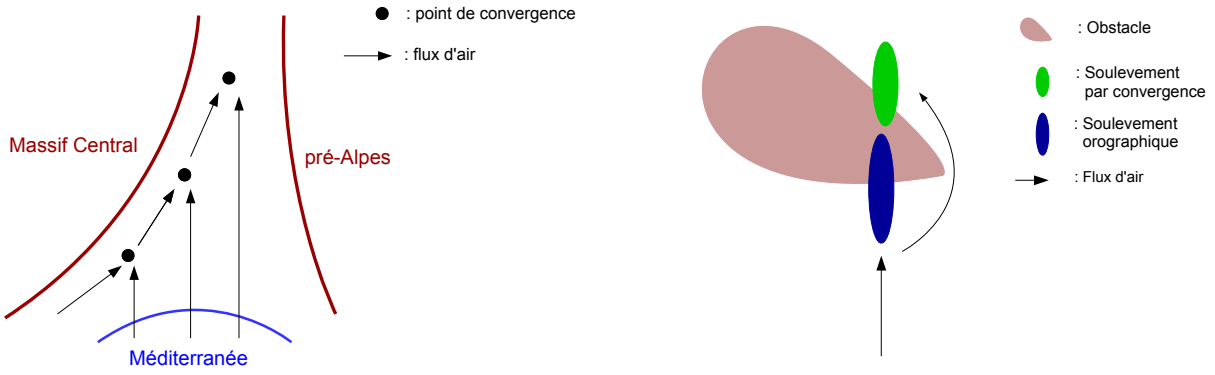

FIGURE I.2 – Schémas illustrant la formation des systèmes pluvieux sur le piémont (gauche) et sur le relief (droite).

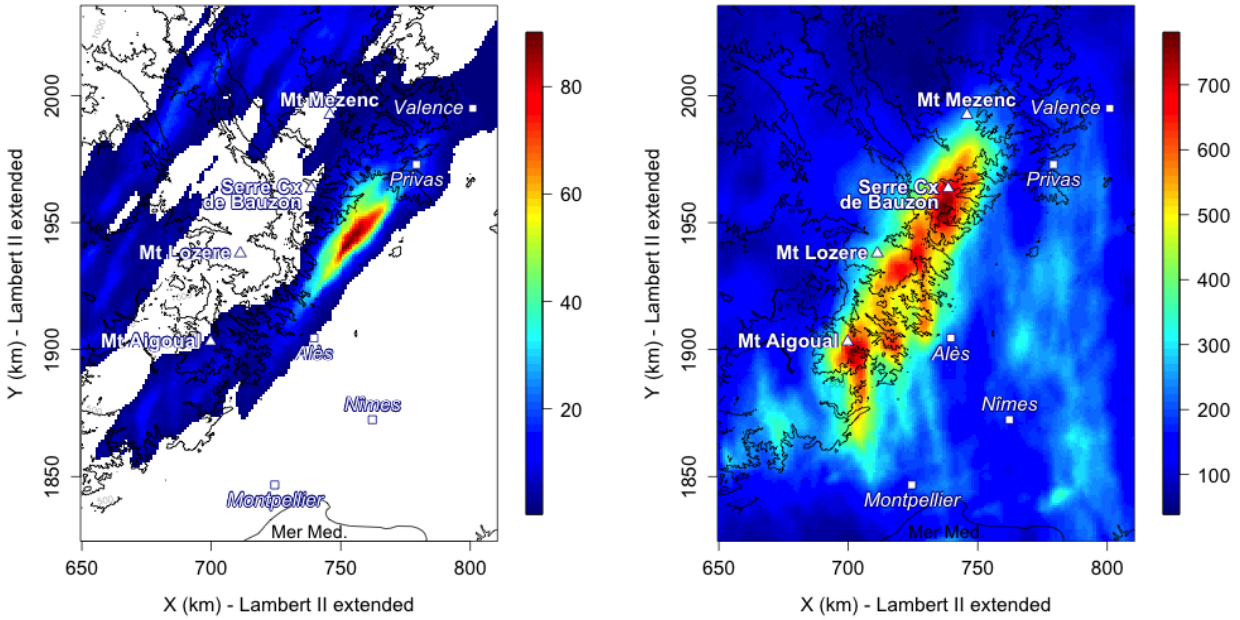

FIGURE I.3 – Gauche : cumul de précipitation (mm) entre 13h et 14h le 7 septembre 2010. Droite : cumul de précipitation (mm) du 1er novembre 2011 à 6h au 6 novembre à minuit. La topographie est représentée avec les courbes de niveau 500 et 1000 mètres au dessus du niveau de la mer.

Ils engendrent ainsi des précipitations moins intenses mais plus longues que celles sur le piémont, pouvant durer plusieurs jours. Le panneau de droite de la Fig. I.3 illustre ce type de systèmes en montrant les précipitations cumulées du 1er novembre au 6 novembre 2011. Les bandes pluvieuses apparaissent clairement autour du Serre de la Croix de Bauzon, à l'est du Mont Lozère et autour du Mont Aigoual. Les ingrédients menant à la formation de ces bandes pluvieuses sont étudiés dans Miniscloux et al. (2001); Anquetin et al. (2003); Godart et al. (2009).

Le cumul de précipitation montré sur le panneau de droite de la Fig. I.3 est l'un des plus fort enregistré durant ces 15 dernières années sur la crête des Cévennes. Cet événement pluviométrique sera étudié dans le Chapitre IV. Il sert également d'exemple dans la section 2, où il sera cité comme "événement de novembre 2011".

En résumé, la topographie et la position géographique de notre région d'étude forment des ingrédients propices au déclenchement d'événements pluviométriques intenses connus sous le nom d'événements cévennols. Il en résulte un risque hydrologique aux impacts socio-économiques élevés caractérisé par des montées rapides des niveaux des cours d'eau appelées crues éclair. Un événement des plus marquants ayant frappé la région s'est déroulé aux alentours de Nîmes, le 3 octobre 1988, où un système en V s'est stabilisé pendant une dizaine d'heures. Les cadereaux aux alentours se sont transformés en torrent provoquant le décès de 9 personnes et de nombreux dégâts (45000 maisons endommagées et 1100 véhicules détruits Duclos et al., 1991). Ce risque hydrologique élevé a engendré la naissance de la campagne HyMeX (Ducrocq et al., 2013; Drobinski et al., 2014) qui propose un éventail d'études des phénomènes hydrométéorologiques extrêmes sur le bassin méditerranéen.

La notion de risque hydrologique comprend deux grandes composantes. La première est l'exposition caractérisée par l'impact de ces crues éclair sur la société. La seconde est l'aléa caractérisé par leurs intensités et leurs fréquences d'occurrence. Dans ces travaux on se concentre sur la quantification de l'aléa qui sert notamment au dimensionnement des structures protégeant les populations des crues comme des barrages ou des digues. L'aléa hydrologique est multifactoriel. L'occurrence d'une crue dépend, par exemple, de la pluviométrie, de la saturation des sols, de l'écoulement souterrain, de la fonte éventuelle du manteau neigeux, de l'hydrogéomorphologie des cours d'eau. Dans ce document, on se concentre sur l'aléa lié aux précipitations, i.e. l'aléa pluviométrique, qui guide de manière prépondérante les débits aux fréquences rares (Guillot, 1993). Les événements pluviométriques extrêmes dans notre région d'étude apparaissant principalement en automne, ce document s'intéresse à la modélisation de l'aléa pluviométrique automnale. Enfin cette étude est menée sous l'hypothèse d'un aléa pluviométrique stationnaire ces 50 dernières années. Le chapitre V donne des pistes de réflexion à l'étude des éventuels changements passés de l'aléa pluviométrique.

2. Sur l'étude de l'aléa pluviométrique

La pluie est un phénomène qui s'accumule non uniformément dans le temps et dans l'espace. Ainsi pour un événement pluviométrique donné, la position géographique des maxima ainsi que leurs intensités dépendent de l'échelle spatio-temporelle considérée. La Fig. I.4 illustre ce point en montrant les maxima de l'événement de novembre 2011 pour différentes échelles spatio-temporelles. Les échelles (3 h, 81 km^2) et (24 h, 1089 km^2) sont pertinentes d'un point de vue hydrologique (Marchi et al.,

$D = 3$ h, $A = 81$ km^2 $D = 24$ h, $A = 1089$ km^2

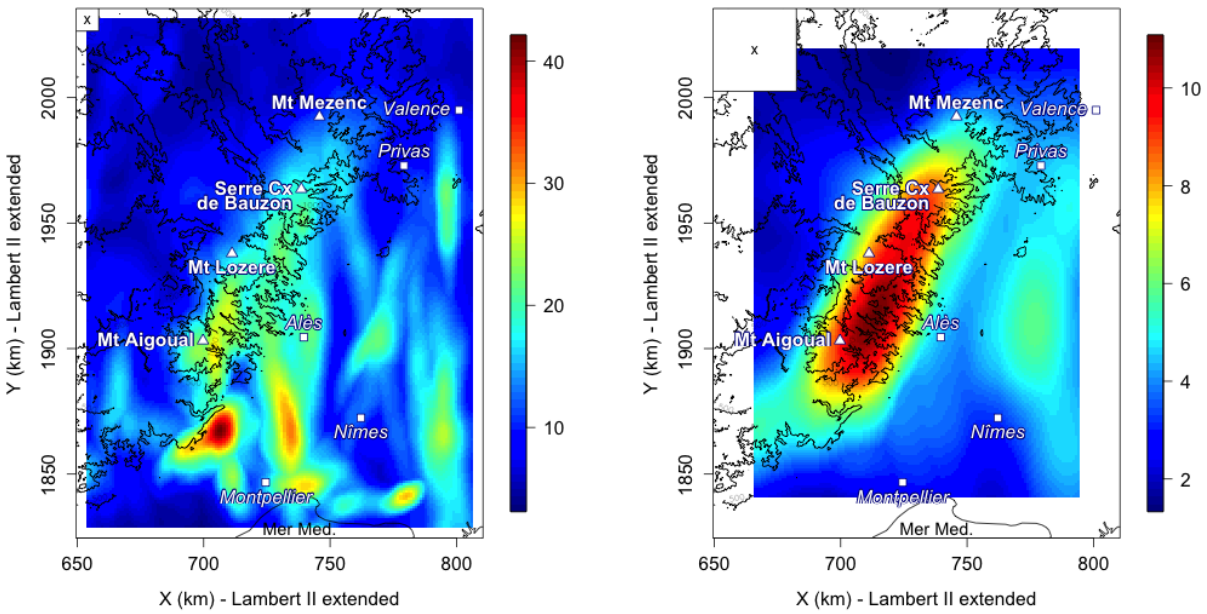

FIGURE I.4 – Intensité maximale (mm/h/km^2) de l'événement de novembre 2011 pour différentes échelles spatio-temporelles. Le carré en haut à gauche représente la surface sur laquelle la pluie est agrégée.

2010). La position spatiale des maxima à l'échelle (3 h, 81 km^2) permet d'identifier des systèmes pluviométriques courts et localisés, susceptibles de déclencher des réactions rapides de petits bassins. A l'échelle (24 h, 1089 km^2), des systèmes plus longs et plus étendus, susceptibles de déclencher des réactions lentes de grands bassins versants, sont identifiés.

Deux remarques préambulaires sur ces cartes. Contrairement aux cartes de la Fig. I.3, l'unité de la pluie est une intensité. L'intensité pluviométrique est la quantité de pluie (mm) normalisée par la durée d'agrégation D (heures - h) et la surface d'agrégation A (kilomètres carrés km^2) et est donc exprimé en mm/h/km^2. La pluie est agrégée sur des surfaces carrées dont la couleur du point au centre représente l'intensité pluviométrique en mm/h/km^2.

La carte du panneau de gauche de la Fig. I.4 montre les intensités maximales pour l'échelle (3 h, 81 km^2). Les intensités maximales les plus fortes sont situées au nord-ouest de Montpellier avec une valeur supérieure à 40 mm/h/km^2. Lorsque la durée D et la surface A augmentent à 24 h et 1089 km^2 (panneau de droite de la Fig. I.4), les intensités maximales les plus fortes sont situées entre le Mont Aigoual et le Mont Lozère avec une valeur supérieure à 10 mm/h/km^2. Ainsi, la position et l'intensité des maxima engendrés par l'événement de novembre 2011 diffèrent grandement entre ces deux échelles. L'étude de l'aléa pluviométrique doit donc se faire sur le continuum d'échelles spatio-temporelles.

Une mesure statistique de l'aléa associé à une certaine intensité maximale est la fréquence d'occurrence de cette intensité maximale, ou de manière équivalente la période de retour. Par exemple, une période de retour de 10 ans correspond à une fréquence d'occurrence moyenne d'une fois tous les 10 ans. Dans ce document, on étudie la période de retour liée aux fortes intensités automnales. La Section 3 présente

une classe de modèles permettant la modélisation de la période de retour en fonction de la durée D, de la surface A et de l'intensité maximale.

La quantification de la période de retour permet ainsi de quantifier l'aléa pluviométrique et par suite de contribuer à la quantification de l'aléa hydrologique. Ce dernier permet le dimensionnement des structures adéquates à la protection des villes et des populations des inondations. Cependant, les périodes de retour pertinentes pour le dimensionnement des ouvrages sont souvent bien supérieures à la période d'observation qui dépasse rarement les quelques dizaines d'années. Les modèles statistiques permettent alors d'extrapoler la période de retour au delà de la longueur de ces séries. Ces modèles n'étant pas parfaits, les incertitudes liées à leur estimation doivent être quantifiées pour éviter une sous-estimation de l'aléa pluviométrique et ainsi une sous-estimation de l'aléa hydrologique qui conduirait à un dimensionnement non adéquat des structures protectrices.

3. Relation Intensité-Durée-Aire-Fréquence sous hypothèse d'invariance par changement d'échelle

Mandelbrot (1984) introduit le concept d'invariance par changement d'échelle par la question de la mesure de la côte de la Bretagne. Imaginons que la côte de la Bretagne soit mesurée avec un mètre puis avec un compas d'écart 1 millimètre. Le mètre va lisser certaines formes alors que le compas va en donner une mesure précise. Ainsi la longueur mesurée au mètre sera plus petite que la longueur mesurée au compas. La Fig. I.5 illustre ce point. Elle a été trouvée dans les papiers de Lewis Fry Richardson après son décès en 1953. Il y trace la longueur de certaines frontières en fonction du pas de mesure en échelle logarithmique. On voit que, pour une frontière donnée, le logarithme de sa longueur est une fonction linéaire du logarithme du pas de mesure et décroit avec l'augmentation de ce pas. Ceci illustre les relations invariantes par changement d'échelle : soit C une frontière, (l_1, l_2) deux pas de mesures et (C_{l_1}, C_{l_2}) les longueurs de C associées. On a

$$\log C_{l_1} = -a \log l_1 + b \text{ et } \log C_{l_2} = -a \log l_2 + b,$$

où a et b sont deux réels et $a > 0$ dans le cas de la Fig. I.5. Par suite :

$$C_{l_1} = \left(\frac{l_1}{l_2}\right)^{-a} C_{l_2}.$$

C_{l_1} et C_{l_2} sont ainsi égaux à un facteur d'échelle près.

Lovejoy and Mandelbrot (1984) et Schertzer and Lovejoy (1987) exhibent le caractère d'invariance par changement d'échelle de la pluie à l'aide de réflectivité obtenue par radar. Puis Gupta and Waymire (1990) formalisent un cadre stochastique de l'invariance par changement d'échelle. Ils y développent notamment une notion de "changement d'échelle simple" (*simple scaling* en anglais). Soit X une variable aléatoire et Ω l'espace de ses réalisations. Pour $\omega \in \Omega$, on dit que $X(\omega)$ est régi par un changement d'échelle simple si et seulement si son rééchelonnement par un réel positif λ s'effectue par la multiplication d'un facteur λ^H, où H est un réel positif. En terme probabiliste cela

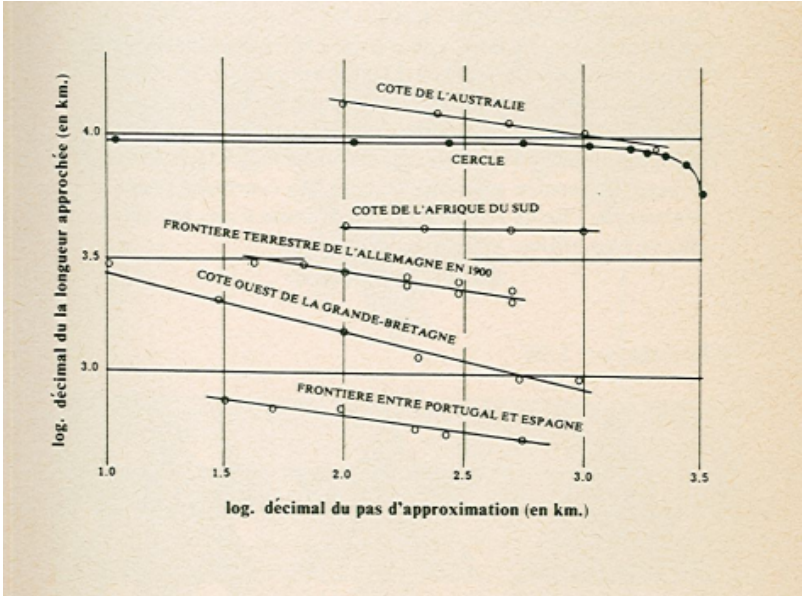

FIGURE I.5 – Longueur de frontières (km) contre pas de mesure de ces frontières (km) ; extraite de Mandelbrot (1984).

s'écrit :

$$\mathrm{pr}\left\{X(\omega) < x\right\} = \mathrm{pr}\left\{X(\lambda\omega) < \lambda^H x\right\}. \tag{I.1}$$

Gupta and Waymire (1990) définissent également une notion plus générale appelée "changement d'échelle multiple" (*multi scaling* en anglais). L'Eq. I.1 implique que pour $\omega \in \Omega$ et pour tout réel q :

$$\mathbb{E}\left[X^q(\omega)\right] = \lambda^{-Hq}\mathbb{E}\left[X^q(\lambda\omega)\right]. \tag{I.2}$$

On appelle K une fonction à valeur dans $\mathbb{R}$. On remplace l'exposant $-Hq$ du terme de droite de l'Eq. I.2 par cette fonction K. On obtient alors, pour $\omega \in \Omega$ et pour tout réel q :

$$\mathbb{E}\left[X^q(\omega)\right] = \lambda^{K(q)}\mathbb{E}\left[X^q(\lambda\omega)\right]. \tag{I.3}$$

On dit alors que $X(\omega)$ est régi par un changement d'échelle multiple si et seulement si K est une fonction non linéaire (voir Veneziano and Langousis, 2005; Veneziano et al., 2006; Langousis et al., 2009, 2013, pour des exemples d'utilisation du changement d'échelle multiple). Cependant l'hypothèse de changement d'échelle simple présente moins de complexité que l'hypothèse de changement d'échelle multiple et est vérifiée sur nos données (voir la Section 4 du chapitre II).

Burlando and Rosso (1996) sont les premiers à utiliser le changement d'échelle simple dans un cadre d'extrêmes pluviométriques ponctuels (en un point donné). Ils supposent alors que la variable aléatoire, M_D, des maxima annuels pluviométriques pour une durée D est en relation de changement d'échelle simple avec la variable aléatoire, $M_{D'}$, des maxima annuels pour une durée D'. Traduit en terme probabiliste cela s'écrit $M_D \overset{d}{=} \left(\frac{D}{D'}\right)^{-H} M_{D'}$, c'est à dire :

$$\mathrm{pr}\left\{M_D < x\right\} = \mathrm{pr}\left\{M_{D'} < x\left(\frac{D}{D'}\right)^H\right\}, \tag{I.4}$$

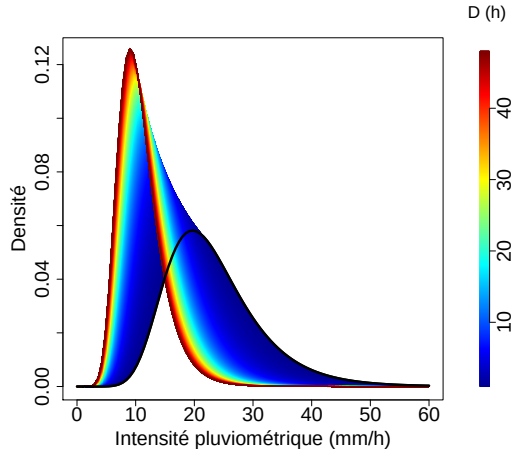

FIGURE I.6 – Illustration du modèle définit Eq. (I.4) avec $H = 0.6$. La densité des maxima pluviométriques ponctuels pour la durée $D = 1$ h est tracée en noire. Les densités des maxima résultantes sont tracées pour le continuum d'échelle temporelle.

où H est un scalaire positif appelé coefficient d'abattement temporel (*scaling coefficient* en anglais). Eq. (I.4) stipule que la distribution des maxima pluviométriques pour une durée D en x est égale à la distribution des maxima pluviométriques pour une durée D' en $x\left(\frac{D}{D'}\right)^H$. Autrement dit, le modèle défini Eq. (I.4) permet de lier les distributions des maxima pluviométriques ponctuels entre elles, sur le continuum d'échelle temporelle. Ceci est illustré Fig. I.6 où est tracé, à titre d'exemple, la densité de $M_{D=1h}$ en noir et les densités résultantes pour le continuum d'échelle temporelle jusqu'à $D = 48$ h. A noter les conséquences d'un tel cadre en terme de biais-variance : l'estimation d'un modèle valable pour toutes les durées au détriment de l'estimation d'une distribution pour chaque durée est susceptible d'augmenter le biais des estimations mais en réduisant drastiquement la variance de ces dernières. Ainsi, dans notre étude nous devrons vérifier la validité de l'Eq. I.4 sur nos données pour que le biais ne prenne pas le pas sur la variance. La Section 4 du chapitre II propose une méthode empirique de vérification de la validité de ce modèle.

Revenons sur le paramètre H de l'Eq. (I.4). Il caractérise la variabilité des maxima pluviométriques ponctuels sur le continuum d'échelle temporelle. La Fig. I.7 illustre ce point avec des intensités maximales tracées en fonction de durées d'agrégations D. Lorsque $H = 0$, les intensités maximales ont tendances à ne pas varier avec la durée d'agrégation D. Lorsque $H = 1$, elles ont tendance à décroitre rapidement lorsque D augmente. Deux cartes de valeurs de H sur notre région d'étude sont proposées dans cette thèse. La première, Fig. II.7 du Chapitre II, à partir de pluviomètres. La seconde, Fig. III.5 du Chapitre III, à partir de réanalyses (les données utilisées sont présentées Section 5).

Nous ajoutons maintenant l'échelle surfacique. Venugopal et al. (1999) exhibe des relations dites de "changement d'échelle dynamique" (*dynamic scaling* en anglais) dans des champs de pluie spatio-temporelle. Ces relations stipulent qu'il existe une relation de puissance entre l'échelle temporelle et l'échelle surfacique. De Michele et al. (2001) propose un cadre stochastique pour l'étude des intensités maximales pluviométriques en combinant l'hypothèse de changement d'échelle dynamique et l'hypothèse de changement d'échelle simple. La formulation probabiliste de son modèle est la

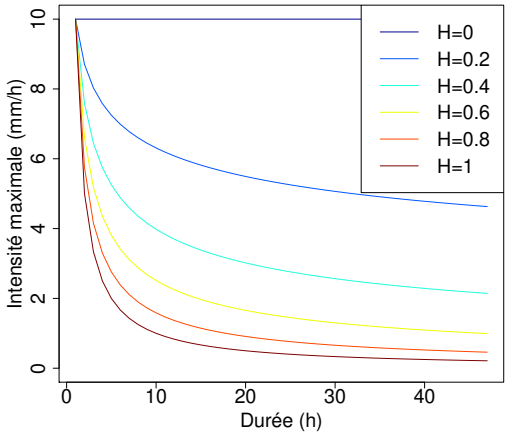

FIGURE I.7 – Illustration de l'influence du paramètre H avec des intensités maximales tracées en fonction de durées d'agrégations D.

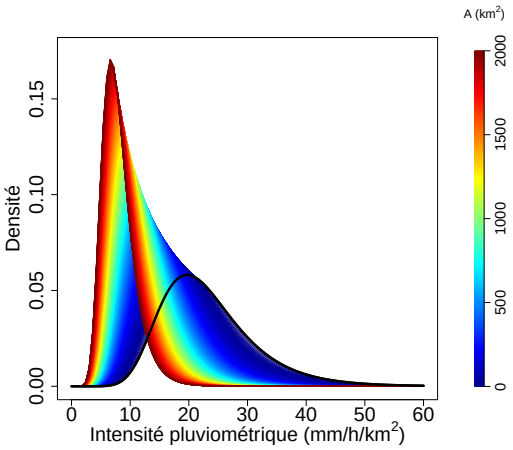

FIGURE I.8 – Illustration de l'Eq. (I.5) pour une durée D fixée et $D = D'$. En noire, la densité des maxima pluviométrique ponctuels. Du bleu au rouge, les densités des maxima surfaciques résultantes.

suivante :

$$\mathrm{pr}\left\{M_{D,A} < x\right\} = \mathrm{pr}\left\{M_{D',A=0} < x\left(\frac{D}{D'}\right)^{H}\mathrm{ARF}(D,A)^{-1}\right\}, \tag{I.5}$$

où $M_{D,A}$ est la variable aléatoire des maxima pluviométriques pour une durée D et une aire A et, $M_{D',A=0}$, est la variable aléatoire des maxima pluviométriques ponctuels pour une durée D. H est le coefficient d'abattement temporel et $\mathrm{ARF}(D,A)$, appelé coefficient d'abattement spatial (*Areal Reduction Factor* en anglais,) est donné par :

$$\mathrm{ARF}(D,A) = \left\{1 + \omega D^{-\beta} A^{\alpha}\right\}^{\gamma}. \tag{I.6}$$

Pour une durée D fixée, $\mathrm{ARF}(D,A)$ permet ainsi de passer de la distribution des maxima pluviométriques ponctuels, i.e. $\mathrm{pr}\left\{M_{D,A=0} < x\right\}$, à la distribution des maxima pluviométriques surfaciques, i.e. $\mathrm{pr}\left\{M_{D,A} < x\right\}$. La Fig. I.8 illustre ce passage avec la densité des maxima pluviométriques ponctuels ($A = 0$ km^2) tracée en noire et les densités des maxima pluviométriques surfaciques résultantes tracées pour le continuum d'échelle spatiale jusqu'à $A = 2000$ km^2.

A noter le compromis biais-variance inhérent à l'utilisation d'un tel cadre (déjà mentionné pour le modèle défini Eq. I.4). Pour que le biais ne prenne pas le pas sur la variance, il est nécessaire de vérifier la validité du modèle défini Eq. I.5 sur nos données. La section III.16 du chapitre III propose une stratégie de vérification d'un tel modèle combiné à une distribution de Gumbel qui sera developpée à la section suivante.

En conclusion de cette Section, le modèle défini à l'Eq. (I.4) permet de lier l'intensité maxima pluviométrique, la durée d'agrégation et la fréquence d'occurrence. Cette classe de modèles appartient aux modèles Intensité-Durée-Fréquence (IDF). Le modèle défini à l'Eq. (I.5) ajoute la dimension surfacique. Il permet de lier l'intensité maximale pluviométrique, la durée, la surface et la fréquence d'occurrence. Cette classe de modèle est donc une extension des modèles IDF, appelée Intensité-Durée-Aire-Fréquence (IDAF).

4. Modélisation statistique des extrêmes pluviométriques

L'objet de cette étude concerne les intensités maximales pluviométriques automnales. Plus précisément, pour chaque automne observé on extrait la valeurs maximales de l'intensité en chaque point d'observation (plus de précision sur les données utilisées en Section 5. Les procédures d'extraction des maxima sont décrites dans chaque chapitre). Le théorème fondateur de la théorie des valeurs extrêmes (voir Coles et al., 2001, pour un développement de la théorie des valeurs extrêmes généralisées) stipulent que si des données indépendantes et identiquement distribuées sont reparties en bloc d'assez grande taille alors la distribution des maxima de chaque bloc est approximativement la distribution des valeurs extrêmes généralisées (GEV pour *Generalized Extreme Value* en anglais). Si une variable aléatoire M suit une telle distribution alors sa fonction de répartition est donnée par l'équation suivante :

$$\mathrm{pr}\left(M < x\right) = \exp\left[-\left(1+\xi\frac{x-\mu}{\sigma}\right)^{-\frac{1}{\xi}}\right], \tag{I.7}$$

avec $1+\xi\frac{x-\mu}{\sigma} > 0$, où μ, $\sigma > 0$ et ξ sont des scalaires, respectivement appelés, paramètre de lieu, d'échelle et de forme.

La Fig. I.9 illustre l'influence des trois paramètres μ, σ et ξ sur la distribution GEV lorsqu'on fait varier un paramètre en fixant les deux autres. Ainsi, par exemple, le panneau de gauche montre les densités d'une GEV lorsque μ varie avec σ et ξ fixés. Lorsque μ augmente la densité est translatée vers la droite et donc la valeur la plus probable (i.e. le mode de la densité) des maxima augmente. Lorsque σ augmente la densité s'aplatit et donc la variabilité des maxima augmente. Des cartes des valeurs des paramètres μ et σ sont proposées Fig. III.5 du Chapitre III pour notre région d'étude. Enfin, lorsque $\xi > 0$ et augmente, la queue droite de la densité s'alourdit donc les maxima les plus exceptionnels ont une fréquence d'occurrence plus élevée. A l'inverse lorsque $\xi < 0$ la densité est bornée à droite se traduisant par des valeurs similaires des maxima de chaque bloc. Une carte de valeurs de ξ, pour notre région d'étude, est proposée dans Blanchet et al. (2016a).

Revenons aux modèles IDF et IDAF présentés en Section 3. L'Eq. (I.4) précise que modéliser, pour D_0 fixé, la distribution de M_{D_0} est suffisant pour modéliser les distributions des variables aléatoires

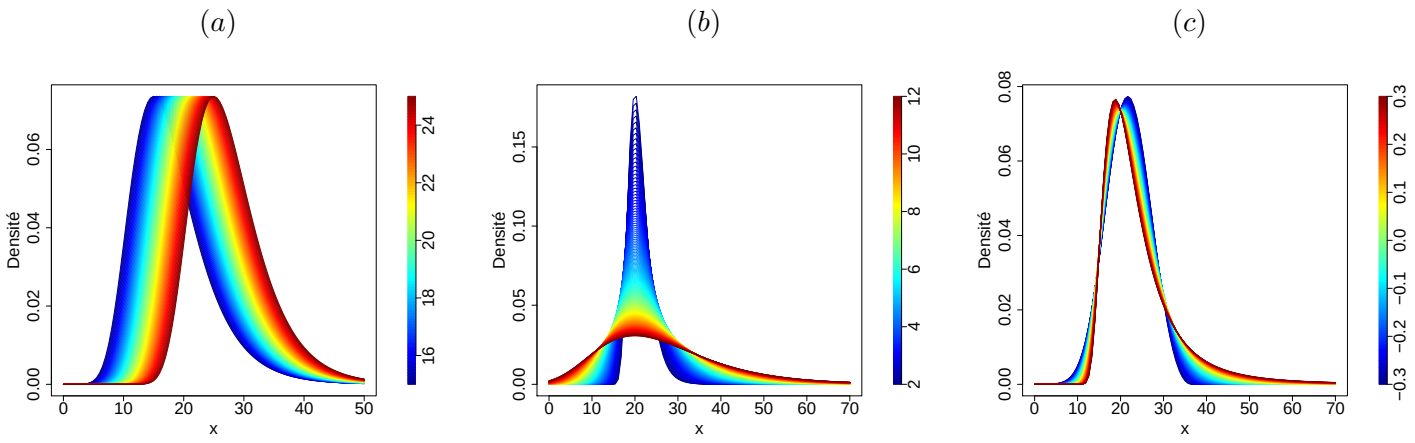

FIGURE I.9 – Illustration de l'influence des paramètres μ, σ, ξ sur la densité GEV. (a) : μ varie, $\sigma = 5$ et $\xi = 0.01$. (b) : σ varie, $\mu = 20$ et $\xi = 0.01$. (c) : ξ varie, $\mu = 20$ et $\sigma = 5$.

des maxima pluviométriques pour n'importe quelle D. Nguyen et al. (1998) montre que si M_{D_0} suit une GEV(μ_0, σ_0, ξ) alors pour tout D, M_D suit une GEV(μ_D, σ_D, ξ) avec $\mu_D = \left(\frac{D}{D_0}\right)^{-H} \mu_0$ et $\sigma_D = \left(\frac{D}{D_0}\right)^{-H} \sigma_0$. La combinaison entre un modèle IDF sous hypothèse de changement d'échelle simple (Eq. I.4) et d'une distribution GEV est l'objet du Chapitre II

De manière équivalente, l'Eq. (I.5) précise que modéliser, pour D_0 fixé, la distribution de $M_{D_0,A=0}$ est suffisant pour modéliser les distributions des variables aléatoires des maxima pluviométriques pour n'importe quelle (D, A). Panthou et al. (2014) montre que si $M_{D_0,A=0}$ suit une GEV(μ_0, σ_0, ξ) alors pour tout (D, A), $M_{D,A}$ suit une GEV$(\mu_{D,A}, \sigma_{D,A}, \xi)$ avec $\mu_{D,A} = \left(\frac{D}{D_0}\right)^{-H} \text{ARF}(D, A)\mu_0$ et $\sigma_{D,A} = \left(\frac{D}{D_0}\right)^{-H} \text{ARF}(D, A)\sigma_0$. Le niveau retour $m_{D,A,T}$ associé à la période de retour T, pour une durée D et une aire A s'exprime alors par

$$m_{D,A,T} = \left(\frac{D}{D_0}\right)^{-H} \text{ARF}(D, A) \left\{ \mu_{D_0,A_0} - \frac{\sigma_{D_0,A_0}}{\xi} \left(1 - \left[-\log\left(1 - \frac{1}{T}\right)^{-\xi} \right] \right) \right\}. \quad \text{(I.8)}$$

A noter que l'hypothèse sous-jacente à l'utilisation d'un modèle IDAF combinant le changement d'échelle dynamique et une distribution GEV est que ξ est constant sur toute la gamme d'échelles spatio-temporelles.

La combinaison entre un modèle IDAF sous hypothèse de changement d'échelle dynamique et simple (Eq. I.5) et d'une distribution de Gumbel (i.e. un cas particulier de la distribution GEV lorsque $\xi = 0$) est l'objet des Chapitres III et IV.

Une remarque importante est que, outre le fait de modéliser l'aléa pluviométrique pour le continuum d'échelles spatio-temporelles, et donc en particulier d'avoir une quantification de l'aléa à des échelles non échantillonnées, les modèles IDF et IDAF permettent de renforcer la robustesse de l'estimation de l'aléa en combinant les intensités maximales pour différentes échelles spatio-temporelles entre elles.

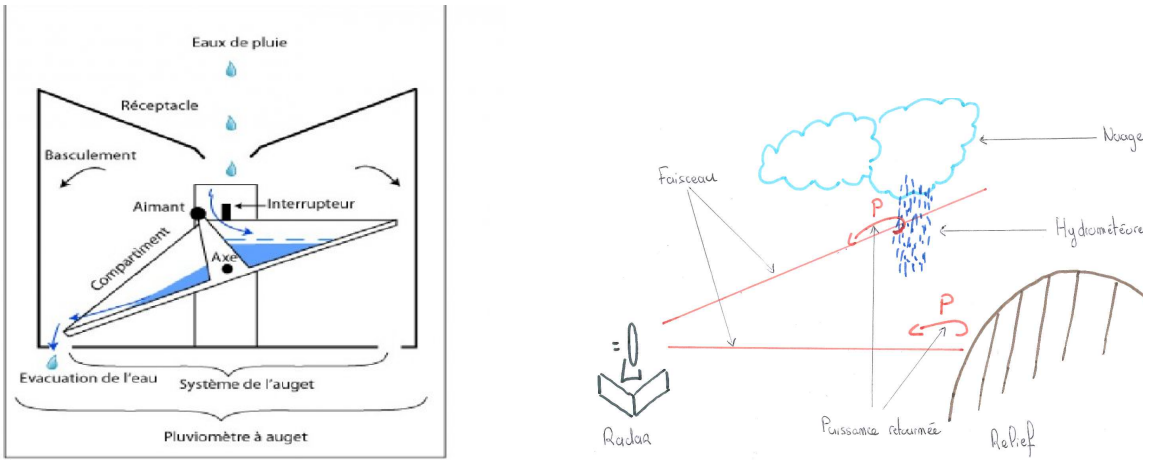

FIGURE I.10 – Schémas de fonctionnement d'un pluviomètre (gauche, issu de http ://www.clg-montand.ac-aix-marseille.fr) et d'un radar (droite).

5. Données pluviométriques utilisées dans cette étude

On dispose de deux bases de données pluviométriques. La première est issue de pluviomètres à augets basculeurs, où les précipitations sont enregistrées toutes les heures, la seconde de réanalyse horaires combinant l'information de pluviomètres horaires et de réflectivité radar.

Le panneau de gauche de la Fig. I.10 décrit le fonctionnement d'un pluviomètre de notre région d'étude. La pluie coule le long du réceptacle (de surface environ égale à 1000 cm^2), remplissant l'auget qui bascule tous les 1 millimètre. Ce basculement déclenche un interrupteur permettant l'enregistrement du millimètre de pluie. La quantité mesurée est donc une quantité d'eau cumulée sur des fenêtres temporelles fixes (par exemple : horaire, journalière). On dispose de 563 pluviomètres horaires (appartenant à Météo France ou Electricité de France) sur une région plus large que celle présentée à la Fig. I.1 s'étendant à l'ouest jusqu'au début des Pyrénées et à l'est jusqu'à Nice (voir la Fig. II.1, Chapitre II, pour une carte de cette région). Cette base de données pluviométrique est utilisée dans le Chapitre II. La procédure de sélection des pluviomètres et d'extraction des intensités maximales pour différentes durées D est décrite dans la Section 3 du Chapitre II.

Le panneau de droite de la Fig. I.10 décrit le fonctionnement d'un radar de notre région d'étude. Le radar émet un faisceau dont une certaine partie est renvoyée lorsqu'il rencontre des hydrométéores. Le radar mesure la puissance de ce faisceau renvoyé, appelée réflectivité et usuellement notée Z. Cette réflectivité mesurée est convertie en lame d'eau R, en supposant que Z et R sont liés par des relations puissances du type $Z = aR^b$. Les coefficients a et b dépendent du type de précipitations (par exemple : taille des gouttes, vitesse de chute), de la climatologie, et des échelles spatio-temporelles considérées.

Une source principale d'incertitude liée à l'estimation de la quantité de pluie par radar est la propagation du faisceau. Le faisceau peut être dévié par un changement brutal de température dans l'atmosphère (phénomène analogue au bâton qui semble cassé une fois mis dans l'eau), ou bloqué par un élément topographique (schématisé par la puissance retournée par le relief sur la Fig. I.10) résultant en une confusion entre les hydrométéores et la topographie. Berne and Krajewski (2013) proposent une

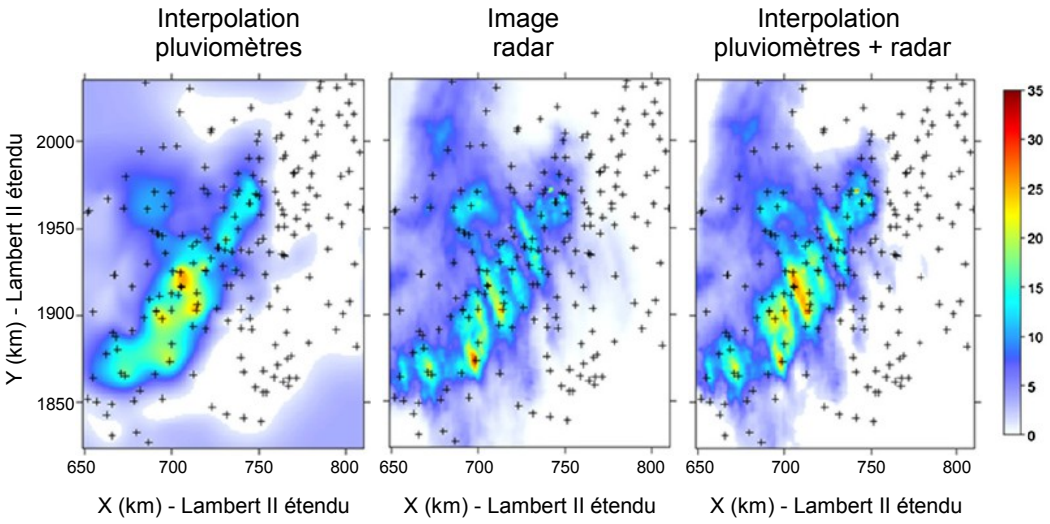

FIGURE I.11 – Illustration des différentes estimations des quantités de pluies le 3 novembre 2011 entre 14h et 15h (modifié à partir de Boudevillain et al. (2016)). Gauche : estimation par interpolation de pluviomètres. Centre : estimation par radar. Droite : estimation par la méthode d'interpolation de Boudevillain et al. (2016).

revue détaillée des différents types de radar mesurant les précipitations et des incertitudes associées à ces mesures.

Pour parer à ces incertitudes, il est commun de combiner l'information obtenue par pluviomètre et celle obtenue par radar. La combinaison de ces deux sources d'informations est complémentaire : le pluviomètre performe dans la quantification locale d'une quantité de pluie alors que le radar, de par sa haute résolution surfacique, permet de capturer la structure spatiale des systèmes précipitants. Les réanalyses utilisées dans le Chaptitre III et IV sont issues d'une telle combinaison développée dans Boudevillain et al. (2016). Elle est basée sur l'estimation d'un processus spatial dont la moyenne est une fonction linéaire de l'estimation du champ des précipitations obtenu par transformation Z-R du champ de réflectivité radar (Delrieu et al., 2014). Cette méthode est communément appelée krigeage avec dérive externe.

La haute résolution spatiale de ces réanalyses permet de mettre en avant certaines caractéristiques à fine échelle des extrêmes pluviométrique qui échappait jusqu'alors avec la seule utilisation de réseau de pluviomètres. Ce point est illustré Fig. I.11 où la quantification des précipitations accumulées entre 14h et 15h le 3 novembre 2011 est considérée. Le panneau de gauche montre l'estimation de cette quantité de pluie obtenue par interpolation de pluviomètres horaires (krigeage ordinaire), dont la position est représentée par des croix noires. Le panneau du centre montre cette estimation obtenue par image radar. On voit les bandes pluvieuses décrites en Section 1 apparaitre. Enfin, le panneau de droite montre cette estimation obtenue par la méthode d'interpolation de Boudevillain et al. (2016) : les bandes pluvieuses, capturées par l'estimation radar, sont présentes et les quantités ponctuelles ont été corrigées par les estimations issues de pluviomètres.

6. Cadres de développement des modèles

Les modèles probabilistes présentés dans cette thèse sont développés dans deux cadres différents : le cadre fréquentiste dans lequel les paramètres du modèle probabiliste sont des scalaires et le cadre bayésien dans lequel les paramètres sont des variables aléatoires. Ainsi d'un cadre à l'autre, la formulation des modèles probabilistes est différente ainsi que leurs inférences. Excepté dans le Chapitre 2 où le cadre de développement est le cadre fréquentiste, dans ce document les variables aléatoires seront écrites en gras afin de les distinguer des scalaires.

On précise maintenant l'estimation d'un modèle dans le cadre fréquentiste et dans le cadre bayésien. Soit $\boldsymbol{X}$ une variable aléatoire de densité f dont n réalisations indépendantes sont représentées par le vecteur x avec $x = (x_1, ..., x_n)$. On appelle θ le vecteur à p composantes représentant l'ensemble des paramètres dans le cadre fréquentiste et $\boldsymbol{\theta}$ celui représentant l'ensemble des paramètres dans le cadre bayésien.

L'estimation de θ dans le cadre fréquentiste repose sur la maximisation de la fonction de vraisemblance $L(\theta) = f(x; \theta)$. Par indépendance des données on a :

$$L(\theta) = \prod_{i=1}^{n} f_i(x_i; \theta). \tag{I.9}$$

On appelle $\tilde{\theta}$ la valeur de θ qui maximise L. $\tilde{\theta}$ est donc une fonction des données x. La variable aléatoire associée, nommée estimateur par maximum de vraisemblance, $\boldsymbol{\theta}_{ML}$, est ainsi une fonction de la variable aléatoire $\boldsymbol{X}$. Le théorème de normalité asymptotique propose une approximation de la distribution de $\boldsymbol{\theta}_{ML}$ quand le nombre de données est grand. Cette approximation est une loi normale multivariée dont une estimation de la moyenne est $\tilde{\theta}$ et dont une estimation de la matrice de variance-covariance est $\Sigma(\tilde{\theta}) = I(\tilde{\theta})^{-1}$ où $I(\tilde{\theta})$ est la matrice $p \times p$ définie par

$$I(\theta) = -\sum_{i=1}^{n} \frac{\partial^2 l_i(\theta)}{\partial\theta\partial\theta^T},$$

évaluée en $\tilde{\theta}$ où $l_i = \log\{f_i(x_i; \theta)\}$ est la log-vraisemblance associées à la données x_i. A noter que $\partial^2 L_i/\partial\theta\partial\theta^T$ représente la matrice $p \times p$ dont l'élément (r, s) est $\partial^2 L_i/\partial\theta_r\partial\theta_s$. Une estimation de l'intervalle de confiance à $(1 - \alpha)$ de la j-ième composante de θ, θ_j, est alors donnée par :

$$[\tilde{\theta_j} - z_{\alpha/2}\sqrt{\Sigma_{jj}}; \tilde{\theta_j} + z_{\alpha/2}\sqrt{\Sigma_{jj}}],$$

où Σ_{jj} et le j-ième élément diagonal de Σ et $z_{\alpha/2}$ est le $(1 - \alpha/2)$ quantile de la distribution normale centrée réduite.

Passons maintenant à l'estimation de $\boldsymbol{\theta}$ dans le cadre bayésien. Cette estimation repose sur le calcul de la densité des paramètres sachant les données, $g(\theta|\boldsymbol{X} = x)$, appelée la densité *a posteriori*. La densité *a posteriori* est donnée par la formule de Bayes :

$$g(\theta|m) = \frac{g(m|\theta)g(\theta)}{\int_\theta g(m|\theta)g(\theta)d\theta}, \tag{I.10}$$

où $g(m|\theta)$ est la fonction de vraisemblance données par l'Eq. (I.9), et, $g(\theta)$ est la densité *a priori*. Cette dernière représente la distribution de $\boldsymbol{\theta}$ avant l'observation des données. Deux grandes classes de densité *a priori* peuvent être distinguées : les densités informatives et les densités non-informative. Les premières sont utilisées pour apporter des connaissances pré analyse, les secondes lorsque ces connaissances ne sont pas disponibles. A partir de la densité *a posteriori*, $g(\theta|\boldsymbol{X} = x)$, un intervalle de crédibilité à $(1 - \alpha)$ est donnée par

$$[u_{\alpha/2}; u_{1-\alpha/2}],$$

où $u_{\alpha/2}$ et $u_{1-\alpha/2}$ sont, respectivement, les quantiles d'ordre $\alpha/2$ et $1 - \alpha/2$ de la densité *a posteriori*.

La plupart du temps, la densité *a posteriori*, $g(\theta|m)$, n'admet pas de forme analytique. Des algorithmes utilisant des chaînes de Markov et des simulations de Monte Carlo (*Markov Chain Monte Carlo algorithms* en anglais) sont alors utilisés pour échantillonner la densité *a posteriori*. Le chapitre 11 de Gelman et al. (2014) détaille ces algorithmes ainsi que leur utilisation.

Le plus connu de ces algorithmes est celui de Metropolis-Hastings dont les étapes sont les suivantes :

i. Tirer un point de départ $\theta^{(0)}$ pour lequel $g(\theta^{(0)}|m)$ est défini et strictement supérieur à 0.

ii. A chaque étape t,
   - Tirer un candidat θ^* à partir d'une distribution $J_t(\theta^*|\theta^{(t-1)})$ (appelée *jumping distribution* en anglais).
   - Calculer la ratio d'acceptation a :

$$a = \min\left\{1, \frac{g(\theta^*|m)/J_t(\theta^*|\theta^{(t-1)})}{g(\theta^{(t-1)}|m)/J_t(\theta^{(t-1)}|\theta^*)}\right\}, \tag{I.11}$$

   - Accepter ou rejeter le candidat θ^*, c'est à dire poser

$$\theta^{(t)} = \begin{cases} \theta^* \text{ avec la probabilité } a, \\ \theta^{(t-1)} \text{ autrement.} \end{cases} \tag{I.12}$$

Un cas particulier de l'algorithme de Metropolis-Hasting est l'algorithme de Metropolis pour lequel la distribution J_t est symétrique, c'est à dire $J_t(\theta_a|\theta_b) \equiv J_t(\theta_b|\theta_a)$. Un exemple de distribution symétrique est la distribution gaussienne. Dans ce cas le quotient $J_t(\theta^*|\theta^{(t-1)})/J_t(\theta^{(t-1)}|\theta^*)$ de l'Eq. I.11 est égale à 1. L'algorithme de Metropolis est utilisé au chapitre II.

La simulation à partir d'algorithme itératif comme celui de Metropolis-Hasting soulève deux problèmes. Le premier concerne la convergence de la chaîne vers la distribution cible ; dans notre cas la distribution *a posteriori*. Autrement dit, comment vérifier que les échantillons tirés représentent bien la distribution cible. Le second concerne la corrélation entre les échantillons simulés. En effet l'inférence à partir d'échantillons corrélés est plus biaisée que l'inférence à partir d'échantillons indépendants.

Le problème de convergence est géré en deux temps. Premièrement on laisse une période "d'échauffement" à l'algorithme. Autrement dit on utilise seulement la seconde moitié des échantillons simulés. Ensuite nous utilisons le critère $\hat{R}$ développé dans le paragraphe 11.4 de Gelman et al. (2014) qui nous permet de vérifier la convergence vers la distribution cible de cette seconde moitié. $\hat{R}$ est un facteur qui quantifie de combien la dispersion de la distribution cible pourrait être réduite si la simulation

des échantillons continuait. Ainsi plus $\hat{R}$ est proche de 1 plus la convergence est assurée. Le problème de corrélation est, quant à lui, géré en gardant seulement 1 échantillon sur 10 de la seconde moitié des échantillons simulés (ou 1 échantillon sur 100 dans le chapitre IV).

Une dernière remarque est que la convergence peut prendre du temps à être atteinte et poser des problèmes de temps de calcul. C'est pourquoi dans le chapitre IV, nous utilisons une version plus efficiente de l'algorithme de Metropolis-Hasting.

La Section 2 du chapitre II propose le développement d'un modèle IDF combiné à une distribution GEV à la fois dans le cadre fréquentiste et dans le cadre bayésien donnant un exemple pratique d'estimation dans ces deux cadres.

Le chapitre IV propose un algorithme MCMC dans lequel une correction est utilisée pour prendre en compte la dépendance entre les données x_i.

7. Vue d'ensemble

Cette thèse fait suite aux travaux, sur la même région, de Ceresetti (2011), dans lesquels il propose un premier cadre théorique pour l'estimation de la période de retour sur le continuum d'échelles spatio-temporelles, combinant les propriétés physiques d'invariance d'échelle (présentées en Section 3) et les propriétés statistiques des valeurs extrêmes (présentées Section 4). Néanmoins, en analysant plusieurs évènements pluvieux sur le piémont et le relief cévenol, Molinié (2013) montre les limites de cette méthodologie. La première est liée à la considération de deux régions homogènes, le relief et la plaine, en termes de précipitations extrêmes. Cette hypothèse n'a pu être vérifiée par manque de données pluviométriques surfaciques à petite échelle à l'époque de ces travaux et conduit à des lois de changement d'échelle spatiale mal spécifiées. La seconde est le manque de robustesse et le possible biais dans l'estimation des périodes et niveaux de retour. Ces écueils proviennent notamment du fait que la procédure d'estimation est décomposée en plusieurs étapes, les erreurs d'estimations s'ajoutant à chacune d'entre elles. La troisième est la non quantification des incertitudes liées à l'estimation de la période de retour qui peut mener à une sous estimation de l'aléa pluviométrique. Les travaux présentés visent à lever ces trois points de blocages. Nous proposons un cadre d'estimation intégré du risque pluviométrique permettant une estimation des périodes et niveaux de retour ainsi qu'une quantification des incertitudes associées. Ce cadre est basé sur les propriétés d'invariance par changement d'échelle de la pluie et est valide pour le continuum d'échelle spatio-temporelles du kilomètres carré à quelques milliers de kilomètres carrés pour l'échelle surfacique et de l'horaire au multi-journalier pour l'échelle temporelle. L'estimation de ce cadre sera faite à partir des réanalyses radar haute résolution, présentées en Section 5, permettant ainsi, en comparaison à Ceresetti (2011), d'améliorer la justesse des lois de changement d'échelle spatiale dans notre région d'étude.

Le Chapitre II vise à comprendre quel cadre d'inférence - fréquentiste ou bayésien - est le plus adapté à l'estimation de l'aléa pluviométrique et des incertitudes associées, pour le continuum d'échelles temporelles. Le Chapitre III propose un modèle permettant d'exprimer l'aléa pluviométrique sur le continuum d'échelles spatio-temporelles. Enfin, le Chapitre IV propose un cadre d'analyse multi-

échelle (en temps et en espace) de l'aléa pluviométrique lié à un événement pluviométrique extrême et notamment la quantification des incertitudes associées.

Chapitre II

Uncertainty estimation of Intensity-Duration-Frequency relationships : a regional analysis

---

Uncertainty estimation of Intensity-Duration-Frequency relationships : a regional analysis

Victor Mélèse[1], Juliette Blanchet[1], Gilles Molinié[1]

[1] *UGA - IGE CS 40700 38 058 Grenoble Cedex 9, France*

Article publié dans *Journal of Hydrology*, doi:10.1016/j.jhydrol.2017.07.054.

Abstract

We propose in this article a regional study of uncertainties in IDF curves derived from point-rainfall maxima. We develop two generalized extreme value models based on the simple scaling assumption, first in the frequentist framework and second in the Bayesian framework. Within the frequentist framework, uncertainties are obtained i) from the Gaussian density stemming from the asymptotic normality theorem of the maximum likelihood and ii) with a bootstrap procedure. Within the Bayesian framework, uncertainties are obtained from the posterior densities. We confront these two frameworks on the same database covering a large region of $100,000$ km^2 in southern France with contrasted rainfall regime, in order to be able to draw conclusion that are not specific to the data. The two frameworks are applied to 405 hourly stations with data back to the 1980's, accumulated in the range 3h-120h. We show that i) the Bayesian framework is more robust than the frequentist one to the starting point of the estimation procedure, ii) the posterior and the bootstrap densities are able to better adjust uncertainty estimation to the data than the Gaussian density, and iii) the bootstrap density give unreasonable confidence intervals, in particular for return levels associated to large return period. Therefore our recommendation goes towards the use of the Bayesian framework to compute uncertainty.

1. Introduction

Determining how often a storm of a given intensity is expected to occur requires an evaluation of its probability of occurrence, i.e. its return period. However extremeness of a rainfall event depends at which duration rainfall is considered. For this reason, Intensity-Duration-Frequency (IDF) curves are extensively used in water resources engineering for planning and design (Rantz, 1971; Cheng and AghaKouchak, 2014; Sarhadi and Soulis, 2017; Te Chow, 1988, chapter 14). They provide estimates of return levels for the continuum of durations and return periods. However a difficulty in producing IDF curves is that return periods of interest for risk mitigation amount usually to several hundreds of years, whereas series at disposal are most of the time much shorter. Estimating the 100-year return level, for example, relies then on extrapolating using some statistical model. Uncertainty is inherent to this estimation because no model is perfect. This is particularly true for extreme value estimation –such as the 100-year return level– because it is based on few data, so a subsequent variability is induced by sampling. Risk evaluation should account for this uncertainty to avoid over-optimistic results (Coles and Pericchi, 2003). Since current infrastructure dealing with flooding and precipitation (e.g. dams or dikes) are based on IDF curves, ignoring uncertainty may result in sharp underestimation of flood risk and failure risk of critical infrastructures.

Few studies have explicitly examined uncertainty in IDF curves. They rely on two distinct theoretical frameworks making different modeling assumptions. The first one is a frequentist framework in which the IDF model parameters are treated as unknown real values. Estimation is usually made by moment- or likelihood-based methods and uncertainty is mainly obtained by a bootstrap resampling scheme to account for the influence of sampling on IDF estimation (Overeem et al., 2008; Hailegeorgis et al., 2013; Tung and Wong, 2014). The second one is a Bayesian framework. It differs from the frequentist framework in that the IDF model parameters are treated as random variables. Its estimation allows by nature uncertainty quantification by providing the most likely distribution for the parameters based on the data (Huard et al., 2010; Cheng and AghaKouchak, 2014; Chandra et al., 2015; Van de Vyver, 2015). The influence of the chosen framework on IDF uncertainty estimation has, to the best of our knowledge, never been addressed in the literature.

In this paper, we propose to confront the frequentist and Bayesian frameworks on the same database covering a large region with contrasted rainfall regimes, in order to be able to draw conclusion that are not specific to the data. The studied region covers $100,000$ km^2 of the southern part of France that is under mediterranean climatic influence and is notably well-instrumented with 563 hourly raingages since the mid-80s, from which we select the 405 stations featuring at least 10 years of observations. The IDF relationships used in this works rely on the simple scaling assumption (Gupta and Waymire, 1990), associated with a Generalized Extreme Value (GEV) distribution representing the frequency of annual maximum rainfall intensity.

This model has been validated in the frequentist case in Blanchet et al. (2016a) for the same region. Here we mainly extend this work by assessing uncertainty in IDF relationships, which was missing in Blanchet et al. (2016a). We develop in Section 2 the Bayesian and frequentist frameworks of GEV-simple scaling IDF relationships. We present the data in Section 3 and give evidence of simple scaling in the range 3h-120h in the region in Section 4. We describe the workflow of analysis in Section

5. Finally, we confront the results of the two frameworks, with a particular focus on uncertainty estimation in Section 6.

2. Two frameworks of IDF relationships

2.1. Introduction

Return levels computation requires estimating the occurrence probability of annual maximum rainfall intensity, i.e. their probability density function (PDF). The founding theorem of extreme value theory (see Coles et al., 2001, for a full review) states that if independent and identically distributed data are blocked into sequences of observations and if each block is long enough, then the PDF of block maxima is approximately the Generalized Extreme Value (GEV) distribution. The combination of strict sense simple scaling and GEV theory for annual maximum rainfall intensity leads to the family of GEV-simple scaling models (Blanchet et al., 2016a). In the next sections, we develop two GEV-simple scaling models, respectively in the frequentist and the Bayesian frameworks. The main difference between the two is that model parameters are scalars under the frequentist framework and random variables under the Bayesian framework. In the following, we write random variables with bold symbols to distinguish them from scalars.

2.2. Frequentist framework

2.2.1. Model

The frequentist framework is the one considered in Blanchet et al. (2016a) in the same region and used in Borga et al. (2005) and Bougadis and Adamowski (2006). It relies on two assumptions. First, on the strict sense simple scaling assumption of Gupta and Waymire (1990) setting that

$$\mathrm{pr}(\boldsymbol{M}_D < x) = \mathrm{pr}\left\{\left(\frac{D}{D_{ref}}\right)^{-H} \boldsymbol{M}_{D_{ref}} < x\right\}, \tag{II.1}$$

where $\boldsymbol{M}_D$ is the random variable of annual maximum rainfall intensity for a duration D, $\boldsymbol{M}_{D_{ref}}$ is the random variable of annual maximum rainfall intensity for a duration of reference D_{ref} ($D_{ref} = 3$h in the application of Section 6), and H is a non-negative scalar called the scaling exponent. In terms of moments, Eq. II.1 leads to the wide sense simple scaling assumption of Gupta and Waymire (1990)

$$\forall q \in \mathbb{R},\ \mathbb{E}(\boldsymbol{M}_D^q) = \left(\frac{D}{D_{ref}}\right)^{-Hq} \mathbb{E}(\boldsymbol{M}_{D_{ref}}^q), \tag{II.2}$$

which shows the advantage over (II.1) of being easily checked empirically on data, at least for moderate q, by computing the empirical moments and regressing them against the duration in log-log scale (see Section 4 for more details in our application).

The second assumption of our model is founded by extreme value theory and asserts that annual maximum rainfall intensity at reference duration, $\boldsymbol{M}_{D_{ref}}$, follows a Generalized Extreme Value

(GEV), i.e. that

$$\mathrm{pr}(\boldsymbol{M}_{D_{ref}} < x) = \exp\left[-\left(1+\xi\frac{x-\mu_{D_{ref}}}{\sigma_{D_{ref}}}\right)^{-\frac{1}{\xi}}\right], \tag{II.3}$$

provided $1+\xi\frac{x-\mu_{D_{ref}}}{\sigma_{D_{ref}}} > 0$, where $\mu_{D_{ref}}$, $\sigma_{D_{ref}} > 0$, ξ are scalars, called respectively the location, scale and shape parameters. Case $\xi = 0$ corresponds to the Gumbel distribution

$$\mathrm{pr}(\boldsymbol{M}_{D_{ref}} < x) = \exp\left[-\exp\left(-\frac{x-\mu_{D_{ref}}}{\sigma_{D_{ref}}}\right)\right]. \tag{II.4}$$

(II.3) associated with (II.1) implies that annual maximum rainfall intensity $\boldsymbol{M}_D$ of any duration D follows a GEV distribution (Blanchet et al., 2016a) and that the GEV parameters at duration D and D_{ref} are linked through $\mu_D = \left(\frac{D}{D_{ref}}\right)^{-H}\mu_{D_{ref}}$, $\sigma_D = \left(\frac{D}{D_{ref}}\right)^{-H}\sigma_{D_{ref}}$, while the shape parameter ξ does not depend on the time scale. As a consequence, the IDF relationships relating the duration D, the return period T_R and the return level (i.e. the quantile of order $1-1/T_R$ of the corresponding GEV distribution) is given by

$$m_{D,T_R} = \left(\frac{D}{D_{ref}}\right)^{-H}\left\{\mu_{D_{ref}} - \frac{\sigma_{D_{ref}}}{\xi}\left(1-\left[-\log(1-\frac{1}{T_R})\right]^{-\xi}\right)\right\}. \tag{II.5}$$

2.2.2. Inference

The set of unknown parameters to be estimated is $\theta = (\mu_{D_{ref}}, \sigma_{D_{ref}}, \xi, H)$. As in Blanchet et al. (2016a), θ is estimated by maximizing the likelihood under the assumptions that i) annual maxima are independent from one year to another, and ii) annual maxima of a given year at different durations are independent. This later assumption is likely to be miss-specified. For instance a 4h annual maximum is likely to be correlated with a 3h annual maximum. However incorporating dependence among many durations complicates the modeling and its estimation (Davison et al., 2012; Cooley et al., 2012; Ribatet and Sedki, 2012; Davison and Huser, 2015), with little gain, if not loss, when only the marginal distributions are of interest (Sebille et al., 2017). We are in this case since IDF relationships relate to quantiles of marginal distributions. Under the assumption of independence, the model log-likelihood is given by

$$\begin{aligned} l(\theta) = &\sum_{D\in\mathcal{D}} n(D)\log\left(\frac{D}{D_{ref}}\right)^{H} - \log(\sigma_{D_{ref}})\sum_{D\in\mathcal{D}} n(D) - \\ &\frac{\xi+1}{\xi}\sum_{D\in\mathcal{D}}\sum_{i=1}^{n}\log\left(1+\xi\frac{\left(\frac{D}{D_{ref}}\right)^{H} m_{D,i} - \mu_{D_{ref}}}{\sigma_{D_{ref}}}\right) - \\ &\sum_{D\in\mathcal{D}}\sum_{i=1}^{n}\left[1+\xi\frac{\left(\frac{D}{D_{ref}}\right)^{H} m_{D,i} - \mu_{D_{ref}}}{\sigma_{D_{ref}}}\right]^{-\frac{1}{\xi}}, \end{aligned} \tag{II.6}$$

where $n(D)$ is the number of observed years at duration D, $m_{D,i}$ is the annual maximum rainfall intensity at the duration D for year number i and $\mathcal{D}$ is the set of considered durations. There is

no analytical form for the maximum of l but maximization can be obtained numerically (e.g. quasi Newton method).

2.2.3. Uncertainty computation

We propose two ways of computing uncertainty in the frequentist framework. The first one relies on the asymptotic normality of the maximum likelihood estimator, but using the correction described in Davison (2008) and used in Van de Vyver (2012) to account for the fact that the likelihood (II.6) ignores dependence among maxima of the same year. Let $\tilde{\theta}$ denote the value maximizing the log likelihood function (II.6). It is function of the data m_D. Writing this in terms of random variables means that the maximum likelihood estimator $\hat{\boldsymbol{\theta}}_{ML}$ is function of the random variable of annual maximum rainfall intensity $\boldsymbol{M}_D$. $\hat{\boldsymbol{\theta}}_{ML}$ is a random variable because it depends on the $\boldsymbol{M}_D$'s which are random, while $\tilde{\theta}$ is a scalar ; it is a realization of $\hat{\boldsymbol{\theta}}_{ML}$. Being random, $\hat{\boldsymbol{\theta}}_{ML}$ has a distribution. The theorem of asymptotic normality of the maximum likelihood estimator provides an approximation for this distribution when the number of data is large. Under the correction of likelihood misspecification for dependence, it states that $\hat{\boldsymbol{\theta}}_{ML}$ can be considered as multivariate normal distributed, with mean approximated by $\tilde{\theta}$ and covariance matrix approximated by $\Sigma(\tilde{\theta}) = I(\tilde{\theta})^{-1}V(\tilde{\theta})I(\tilde{\theta})^{-1}$ where $I(\tilde{\theta})$ and $V(\tilde{\theta})$ are the 4×4 matrices

$$I(\theta) = -\sum_{i=1}^{n} \frac{\partial^2 l_i(\theta)}{\partial\theta\partial\theta^T}, \quad V(\theta) = \sum_{i=1}^{n} \frac{\partial l_i(\theta)}{\partial\theta}\frac{\partial l_i(\theta)}{\partial\theta^T},$$

evaluated in $\tilde{\theta}$. An approximate $(1-\alpha)$ confidence interval for θ_j, any of the four model parameters, is then given by

$$\tilde{\theta}_j \pm z_{\alpha/2}\sqrt{\Sigma_{jj}},$$

where $z_{\alpha/2}$ is the $(1-\alpha/2)$ quantile of the standard normal distribution and Σ_{jj} is the jth diagonal element of Σ.

Applying the delta method (Coles et al., 2001), the maximum likelihood estimator of the T_R-year return level at duration D can be considered as normal distributed with mean approximated by $g(\tilde{\theta})$ and variance approximated by $\tau^2(\tilde{\theta})$, where

$$\tau^2(\theta) = \frac{\partial g(\theta)}{\partial\theta^T}\Sigma(\tilde{\theta})\frac{\partial g(\theta)}{\partial\theta},$$

and g is the right-hand side function in (II.5). In particular, its $(1-\alpha)$ confidence interval is approximately

$$g(\tilde{\theta}) \pm z_{\alpha/2}\,\tau(\tilde{\theta}).$$

The second method to obtain uncertainties is based on bootstrap resampling. It allows to account for the influence of sampling on IDF estimation. It consists of resampling the data with replacement to obtain new samples. Let's assume that the annual maxima are stored in a matrix with one row per year and one column per duration. A bootstrap sample is constructed by drawing with replacement the lines of the matrix. The log likelihood function is maximized for each bootstrap sample, given a new estimate $\tilde{\theta}$, which is considered as a possible realization of the true estimator $\hat{\boldsymbol{\theta}}$. If R bootstrap samples are used, R realizations $\tilde{\theta}_1, \ldots, \tilde{\theta}_R$ are obtained. When R is large (e.g. $R = 1000$ in Section 6),

usual density estimates (e.g. Kernel density) can be applied to $\tilde{\theta}_1, \ldots, \tilde{\theta}_R$ to obtained an approximate density for $\hat{\boldsymbol{\theta}}$. An approximate density for the T_R-year return level is obtained likewise by estimating the density of the $g(\tilde{\theta}_1), \ldots, g(\tilde{\theta}_R)$, where g is the right-hand side function in (II.5). Approximate $(1-\alpha)$ confidence intervals are obtained empirically as the interval bounded by the empirical quantiles of order $\alpha/2$ and $(1-\alpha/2)$.

2.3. Bayesian framework

2.3.1. Model and priors

As in the frequentist framework, the Bayesian framework relies on the strict sense simple scaling hypothesis combined with the GEV distribution. However in this case, the model parameters $\boldsymbol{\theta} = (\boldsymbol{\mu}_{D_{ref}}, \boldsymbol{\sigma}_{D_{ref}}, \boldsymbol{\xi}, \boldsymbol{H})$ are random variables. Thus the two above hypothesis, as all the equations derived in Section 2.2.1, still apply but conditionally on $\boldsymbol{\theta}$ equals to some $\theta = (\mu_{D_{ref}}, \sigma_{D_{ref}}, \xi, H)$. In particular, the strict sense simple scaling assumption of Gupta and Waymire (1990) turns into

$$\mathrm{pr}(\boldsymbol{M}_D < x | \boldsymbol{H} = H) = \mathrm{pr}\left\{ \left(\frac{D}{D_{ref}} \right)^{-H} \boldsymbol{M}_{D_{ref}} < x \right\}, \tag{II.7}$$

which leads, in terms of moments, to

$$\forall q \in \mathbb{R},\ \mathbb{E}(\boldsymbol{M}_D^q | \boldsymbol{H} = H) = \left(\frac{D}{D_{ref}} \right)^{-Hq} \mathbb{E}(\boldsymbol{M}_{D_{ref}}^q). \tag{II.8}$$

Likewise, conditional on $\boldsymbol{\theta} = \theta$, the annual maximum rainfall intensity $\boldsymbol{M}_D$ of any duration D, follows a GEV distribution, i.e.

$$\mathrm{pr}(\boldsymbol{M}_D < x | \boldsymbol{\theta} = \theta) = \exp\left[-\left(1 + \xi \frac{x - \mu_D}{\sigma_D} \right)^{-\frac{1}{\xi}} \right], \tag{II.9}$$

where $\mu_D = \left(\frac{D}{D_{ref}} \right)^{-H} \mu_{D_{ref}}$ and $\sigma_D = \left(\frac{D}{D_{ref}} \right)^{-H} \sigma_{D_{ref}}$.

Finally, the random variable of the T_R-year return level for duration D is given by

$$\boldsymbol{M}_{D,T_R} \overset{a.s.}{=} \left(\frac{D}{D_{ref}} \right)^{-\boldsymbol{H}} \left[\boldsymbol{\mu}_{D_{ref}} - \frac{\boldsymbol{\sigma}_{D_{ref}}}{\boldsymbol{\xi}} \left(1 - \left[-\log(1 - \frac{1}{T_R}) \right]^{-\boldsymbol{\xi}} \right) \right], \tag{II.10}$$

where $\overset{a.s.}{=}$ means equality almost surely.

Since (II.9) is conditional on $\boldsymbol{\theta}$, full modeling of $\boldsymbol{M}_D$ requires defining the density of $\boldsymbol{\theta}$, i.e. the prior density. Here we assume independence of the model parameters, i.e.

$$f(\theta) = f(\mu_{D_{ref}}) f(\sigma_{D_{ref}}) f(\xi) f(H). \tag{II.11}$$

We make this choice for the sake of simplicity but a separate analysis applied to the data of Section 3 revealed that actually choosing dependent or independent priors does does not affect the results.

In (II.11) univariate prior densities for $\mu_{D_{ref}}$, $\sigma_{D_{ref}}$, ξ and H have to be chosen. Choice of the prior density is crucial in Bayesian analysis and a whole field of research is devoted to this issue. Prior densities can be separated into two major classes, namely subjective (or informative) and objective (or uninformative) priors (Gelman et al., 2014; Beirlant et al., 2005, chapter 11). Subjective priors allow to bring prior knowledge to the analysis, based on expert information of different degrees. Objective priors (Berger, 2006; Kass and Wasserman, 1996) should be used when subjective analysis is not possible. Most common objective priors include the uniform density, Maximum Data Information prior (Zellner, 1998) and Jeffreys prior (Kass and Wasserman, 1996; Jeffreys, 1998). For what matters extreme rainfall and GEV distributions, there is no consensus on the choice of the priors. Coles and Tawn (1996) use expert information on extreme quantiles. Huard et al. (2010) and Chandra et al. (2015) use objective priors for the location (uniform) and scale (Jeffreys) but a weakly subjective prior for the shape (Beta). Coles and Pericchi (2003) uses objective priors for the three GEV parameters (Gaussian for the location and shape, log-Gaussian for the scale). For IDF relationships, Van de Vyver (2015) uses objective priors for the location, scale and scaling exponent (respectively Gaussian, log-Gaussian and uniform) and weakly subjective prior for the shape (Beta). Muller et al. (2008) also uses objective priors for the location, scale and scaling exponent (Gaussian for the first and log-Gaussian for the two latter) and weakly subjective prior for the shape (uniform).

In this work, we aim to use a model as general as possible in order to make a fair comparison of uncertainty with the frequentist framework, which does not include expert knowledge, so the four chosen priors are very weakly informative. For the location parameter at reference duration (3h), we choose an objective uniform density as in Huard et al. (2010) and Chandra et al. (2015). The bounds are chosen to span the worldwide values of $\boldsymbol{\mu}_{D_{ref}}$, from very arid to very humid regions, in order to use priors as little informative as possible for our data. In a study of more than 15,000 worldwide records, Papalexiou and Koutsoyiannis (2013) finds that the location parameter for annual maxima of daily rainfall ranges between 6 and 700mm/day. Since rainfall accumulation cannot be greater in 3h than in 24h, we can anticipate that the location parameter for annual maxima of 3h rainfall is worldwide no lower than 6mm/3h and no bigger that 700mm/3h, i.e. between 2 and 233mm/h at 3h duration. In order to be even less conservative, we set the lower and upper bounds of the uniform prior for $\boldsymbol{\mu}_{D_{ref}}$ to 0 and 250mm/h at 3h duration, respectively. Likewise, we use for the scale parameter at reference duration $\boldsymbol{\sigma}_{D_{ref}}$ a uniform prior with bounds 0.1 and 150mm/h at 3h duration, which extends over the range of values found in Papalexiou and Koutsoyiannis (2013) (2-400mm/day). For the shape parameter, we use the normal density, which tends to be less informative than the Beta prior used in Huard et al. (2010), Chandra et al. (2015) and Van de Vyver (2015), which has bounded tails. Papalexiou and Koutsoyiannis (2013) shows that the distribution of the shape parameter is approximately Gaussian with mean 0.1 and standard deviation 0.045. Here we consider a much less informative density by using a Gaussian prior with mean 0.1 but standard deviation 0.5. Finally, owing to the fact that the scaling parameter is non-negative and lower than 1, we choose for $\boldsymbol{H}$ a uniform density between 0 and 1, as in Van de Vyver (2015).

2.3.2. Inference

For shortness we denote $\boldsymbol{M}$ the set of annual maximum rainfall intensities, i.e. the set of $\boldsymbol{M}_{D,i}$, $D \in \mathcal{D}$, $i = 1, \ldots, n$. In the Bayesian framework, interest is in estimating the density of the parameters

knowing the data, i.e. $f(\theta|\boldsymbol{M} = m)$, called the posterior density. The well known Bayes formula states that

$$f(\theta|m) = \frac{f(m|\theta)f(\theta)}{\int_\theta f(m|\theta)f(\theta)d\theta}, \tag{II.12}$$

where the prior density $f(\theta)$ is given by (II.11) with the aforementioned priors and $f(m|\theta)$ is the density associated to the data under (II.9), whose log expression is assumed to be given by (II.6). By doing this we assume that the maxima at different durations are independent conditional on the parameters. In a Bayesian framework, Van de Vyver (2015) and Muller et al. (2008) model dependence between two durations (namely 24h and 72h) with a logistic model, while Stephenson et al. (2016) uses max-stable processes to model dependence across several durations. However Sebille et al. (2017) shows by comparing different spatial models, including that of Stephenson et al. (2016), that when interest lies in the estimation of marginal quantities, such as return levels, the independence assumption is one of the most creditable one.

In our case, as often in Bayesian analysis, there is no analytical form for the posterior density (II.12) due to the presence of an integral in the normalizing constant. This problem can be overcome by using simulation based techniques such as Markov chain Monte Carlo (MCMC), which provides a way of simulating from complex distributions, such as $f(\theta|m)$, by simulating from Markov chains which have the target distributions as their stationary distributions. Estimates of the posterior distribution could then be obtained from the simulated sample at convergence of the Markov chains. There are many MCMC techniques, among which the most popular are the Gibbs sampler when it is possible to simulate from the full conditional distribution, or Metropolis-Hastings sampling otherwise. Here simulation from the full conditional distribution is not straightforward so we use Metropolis sampling, i.e. Metropolis-Hastings with symmetric jumping distributions (or proposal distribution). In our case, it proceeds as follows :

i. Draw a starting point $\theta^{(0)}$ for which $f(\theta^{(0)}|m)$ is defined and strictly superior to 0.

ii. At each step t,
   - Draw a candidate θ^* from a symmetric jumping distribution $J_t(\theta^*|\theta^{(t-1)})$.
   - Derive the acceptance probability :

$$a = \min\left\{1, \frac{f(\theta^*|m)}{f(\theta^{(t-1)}|m)}\right\} = \min\left\{1, \frac{f(m|\theta^*)f(\theta^*)}{f(m|\theta^{(t-1)})f(\theta^{(t-1)})}\right\}, \tag{II.13}$$

   - Accept or reject the candidate θ^*, i.e. set

$$\theta^{(t)} = \begin{cases} \theta^* \text{ with probability } a, \\ \theta^{(t-1)} \text{ otherwise.} \end{cases} \tag{II.14}$$

We use a Gaussian distribution for the jumping distribution $J_t(.|\theta^{(t-1)})$, with mean $\theta^{(t-1)}$ and diagonal covariance matrix with standard deviation set at initialization to $(0.3, 0.3, 0.025, 0.025)$, and then tuned during the first half iterations of the MCMC so that the acceptance rate of θ (i.e. the proportion of times θ^* is set to $\theta^{(t)}$) is between 30% and 50%. The resulting chain converges, after an initial burn-in period, to the posterior distribution. At the end of the algorithm, samples of the posterior density are obtained as $\theta^{(t)}$, for t exceeding the burn-in period. We will see in Section 5 how to

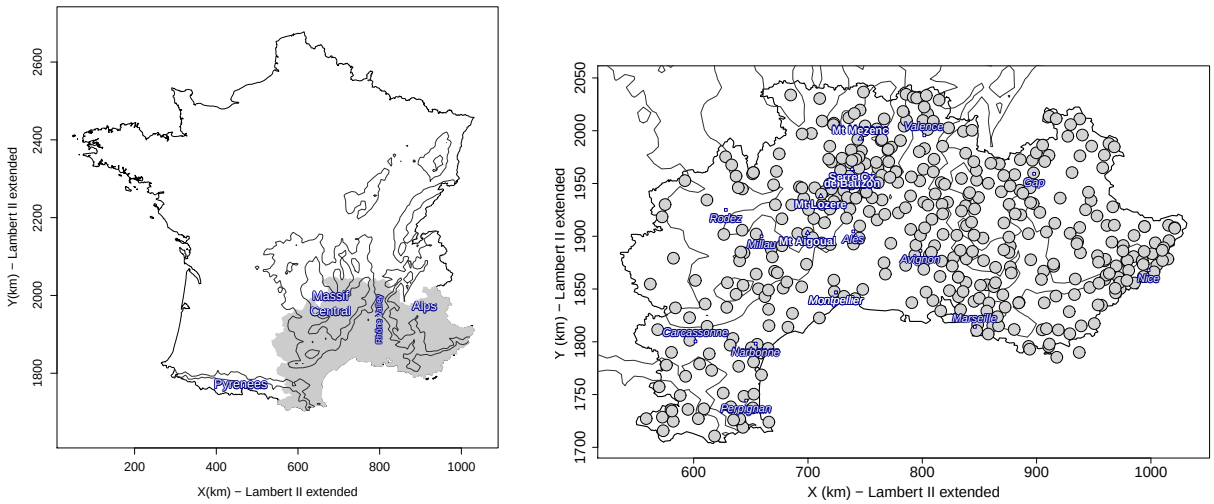

FIGURE II.1 – Map of studied region with main mountains peaks (triangle), main cities (square) and raingage locations (circle).

monitor this convergence. Estimate of the posterior density can be obtained by usual (e.g. Kernel) density estimate based on an independent subsample of these $\theta^{(t)}$.

3. Data

The studied region corresponds to the southern part of France that is under Mediterranean climatic influence (see Fig. II.1). It is limited to the south by the Mediterranean coast from Perpignan to Nice, to the west by the Pyrenees, to the north by the Massif Central and to the east by the southern Alps. Altitude ranges from 0 to more than 3000 m.a.s.l. The highest peaks are located in the the Alps and the Pyrenees while the Massif Central is mostly below 1500m. The mountain massifs design funnel-shaped domains that are known to experience severe storms generating flash-floods from various foothill rivers. Examples are provided by quite recent severe events causing numerous human losses and considerable damages that occurred in 1999 on the Aude River (Gaume et al., 2004), in 2002 on the Gard River (southern edge of the Massif Central - Delrieu et al., 2005), in 1992 on the Ouvèze River (eastern flank of the Alps - Sénési et al., 1996) and in 2010 on the Argens River (southern edge of the Alps - Ruin et al., 2014). Nevertheless a strong heterogeneity exists in terms of occurrence of such events in this area. The south-eastern edge of the Massif Central experiences most of the extreme storms and resulting flash-floods (Fig. 2 of Nuissier et al., 2008). The HyMeX field campaign (Ducrocq et al., 2013; Drobinski et al., 2014) illustrates a variety of meteorological situations blocking heavy rainfall systems over the region. The presence of the surrounding mountain massifs is critical in the positioning and stationarity of these systems (Nuissier et al., 2008).

The instrumented area covers a surface of about $100,000$ km^2, as displayed in Fig. II.1. Hourly rainfall data are acquired by either Météo-France or Electricité de France since the mid 80's for the oldest. 563 hourly raingages with more than 10 years observations are available. We restrict the data to the three months of September-October-November (SON) since flash floods usually occur in Autumn in this region. Starting from hourly data, we create new databases by aggregating hourly rainfalls at 3h, 4h, 8h, 12h, 24h, 48h, 72h, 96h and 120h using 1h-length moving windows. We do

not consider maxima at duration 1h and 2h because these maxima are likely to underestimate the true maxima when a sampling period of 1h is used. This underestimation is likely to decrease with duration. Then, SON maxima are extracted for each of these durations. Following Blanchet et al. (2016a), a given maximum is considered as missing if its rank is smaller than $pmiss \times N$ where $pmiss$ is the proportion of missing values for that season and duration, and N is the number of maxima for the considered duration. This allows us to consider maxima of very incomplete year (large $pmiss$), provided these maxima are large compared to the other maxima (i.e. their ranks are large). Finally a given SON season is considered as completely missing if at least four of the nine durations are missing and the whole station is considered as missing (i.e. excluded from the analysis) if less than 10 SON maxima are observed. Doing so, we end up with a set of 405 stations (see Fig. II.1).

4. Evidence of simple scaling

We first give empirical evidence of simple scaling of rainfall in our region. It is not possible to check the strict sense simple scaling assumptions (II.1) and (II.7) directly on the data because they depend on H which is unknown. However, it is possible to check their counterpart versions (II.2) and (II.8) for the moments, which state in both frameworks that

- wide sense scaling hypothesis : the logarithm of moment of order q of annual maximum rainfall intensity is a linear function of the logarithm of duration,
- wide sense simple scaling hypothesis : the slope of the above linear functions is an affine function of q (i.e. of the form Hq).

We check wide sense scaling hypothesis for $q = 0.25, 0.5, 0.75, 1, 1.25, 1.5, 1.75, 2$ by computing, for each station, the empirical moment of order q of the maxima at each duration, and regressing the logarithm of these values with respect to the log duration. We show in Figure II.2 the boxplots of the correlation coefficients, R^2, of these regressions for the 406 stations. We see that all R^2 are all close to one, as should be under the simple-scaling hypothesis. However, this gives only rough evidence of scaling because R^2 are computed over all durations from 3h to 120h, so it is not possible to assess whether specific durations tend to depart from the regressing lines, which would mean that the simple scaling hypothesis applies only on part of the considered durations. To check this, we consider the case $q = 1$ and compute the slope between averages of successive durations, i.e. between e_d and e_{d+1}, where e_d is the average of maximum rainfall intensity at the dth smallest duration, for a given station. Let call s_d this slope, $d = 1, \ldots, 8$. Any ratio $s_d/s_{d'}$ should be one under the wide sense scaling hypothesis. We show in Fig. II.3 the boxplots of the ratio s_d/s_{d+1}, $d = 1, \ldots, 7$, for the 406 stations. We see that 95% of the ratio lie between 0.6 and 1.4, which can be considered as close to one given that each slope is computed on two points only. More importantly maybe, we do not see any break point in the 95% envelopes as d increases, so the wide sense scaling hypothesis seems to apply equally to all durations between 3h and 120h.

To check the wide sense simple scaling assumption, we consider the slopes of Fig. II.2 for $q = 0.25, 0.5, 0.75, 1,$
$1.25, 1.5, 1.75, 2$, divide them by q, and denote c_k, $k = 1, \ldots, 7$, these values. If the simple scaling holds, each c_k should equal H. Fig. II.4 shows the ratio c_k/c_{k+1}, for $k = 1, \ldots, 7$. We see that 95% of

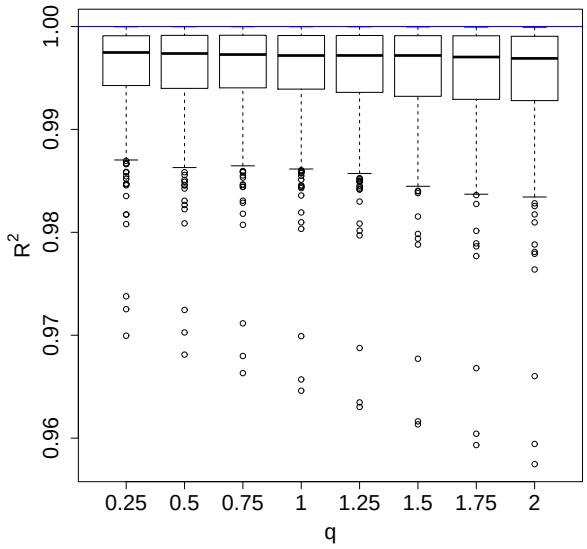

FIGURE II.2 – Boxplots of the correlation coefficients, R^2, of the empirical moments of order $q = 0.25, 0.5, 0.75, 1, 1.25, 1.5, 1.75, 2$ of maximum rainfall intensity versus duration in log-log scale. The blue horizontal line show the theoretical value under the wide sense scaling hypothesis.

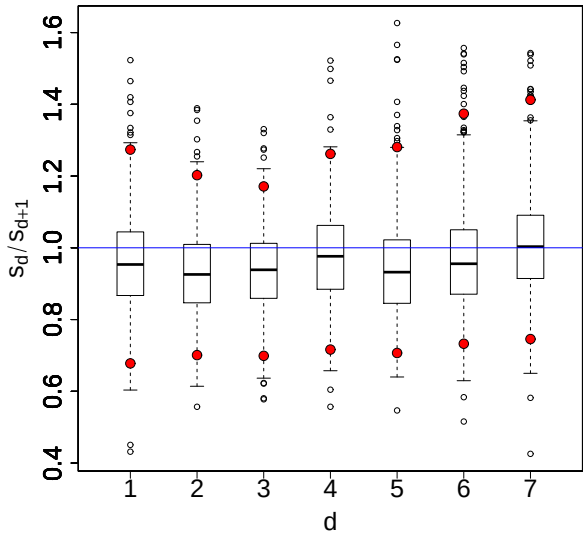

FIGURE II.3 – Boxplots of the ratio of the slopes s_d/s_{d+1}, for $d = 1, \ldots, 7$ and $q = 1$. The upper and lower red points show the quantiles of order 0.975 and 0.025, respectively. The blue horizontal line shows the theoretical value under the wide sense scaling hypothesis.

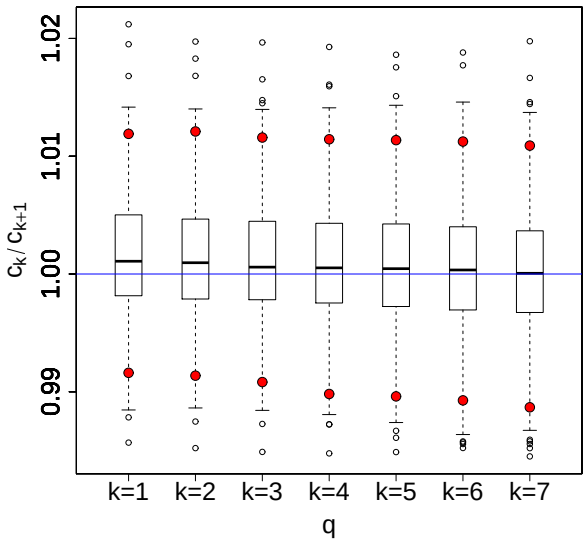

FIGURE II.4 – Boxplots of the ratio of the slopes c_k/c_{k+1}, for $k = 1, \ldots, 7$. The upper and lower red points show the quantiles of order 0.975 and 0.025, respectively. The blue horizontal line shows the theoretical value under the wide sense simple scaling hypothesis.

ratios lie between 1.011 and 0.988, with no value lower than 0.984 and larger than 1.021. This gives good evidence of wide sense simple scaling in the region.

5. Workflow

5.1. Frequentist framework

The GEV simple scaling model in the frequentist framework (Section 2.2.1) is estimated at each station by maximizing the likelihood (II.6). Optimization is based on the gradient projection method of Byrd et al. (1995) allowing box constraints for the variables. Constraints are set on the scale parameter, which is restricted to strictly positive values, the shape parameter, which is restricted in the range $(-0.75, 0.75)$ and the scaling parameter H, which is constrained in the range $(0, 1)$. Optimization is initialized by $\theta_1 = (\mu_{D_{ref,1}}, \sigma_{D_{ref,1}}, \xi_1, H_1)$, which can be considered as a smart initialization in that it is built from that data of each station : ξ_1 is set to 0, corresponding to a Gumbel distribution. $\mu_{D_{ref,1}}$ and $\sigma_{D_{ref,1}}$ are estimated using the method of moments under the Gumbel assumption. Following (II.2) with $q = 1$, H_1 is set to the opposite of the regression slope of the log average maxima on the log duration (i.e. case $q = 1$ in Fig. II.2). Starting from θ_1, the gradient projection algorithm stops in $\tilde{\theta}$, the maximum likelihood estimate, if it is unable to reduce the log likelihood (II.6) by a factor of $10^{-8} \times |l(\tilde{\theta})|$. Density estimates of the associated random variable are obtained i) from the theorem of asymptotic normality of the maximum likelihood estimator, and ii) by bootstrap resampling technique using 1000 bootstrap samples. Return level estimates and associated densities are derived from these estimations as detailed in Section 2.2.3.

5.2. Bayesian framework

The same starting points θ_1 is used to initialize Metropolis-Hastings algorithm in the Bayesian framework (Section 2.3.2). Convergence of the MCMC is monitored using the $\hat{R}$ convergence criteria of Gelman et al. (2014) chapter 6, based on five runs of the Metropolis-Hastings algorithm. Convergence is considered to be reached if $\hat{R} < 1.06$, which is obtained after $20,000$ iterations. The burn-in period is set to the first half iterations and every 10th iteration of the remaining 10,000 iterations is considered for the estimation of the posterior density, in order to reduce dependence within the sample. So, the posterior density estimation is based on 1000 samples. Posterior density estimates of return levels are obtained from (II.10), using these 1000 samples. To summarize any posterior density with one single value and, in particular, compare estimations with the frequentist framework, we decide to consider the posterior mean, i.e. the mean of the posterior density. Another common choice is to consider the mode of the posterior density (maximum a posteriori) but this is slightly less stable than the posterior mean.

6. Results and discussion

6.1. IDF curves

Although this is not the main focus of this study, we present below some results on IDF relationships because they are valuable from a climatological point of view by documenting the main hydrological processes leading to extreme rainfall in the region.

6.1.1. Estimation and goodness-of-fit

Fig. II.5 compares the Bayesian (posterior mean) and frequentist (maximum likelihood) estimates. It shows that the framework has very little impact on these estimation with the chosen initialization. A separate analysis (not shown) revealed that actually the Bayesian framework is very little sensitive to initialization, whereas the frequentist framework requires a quite reasonable initialization. In order to assess goodness-of-fit of the estimated IDF curves, we consider two goodness-of-fit criteria proposed by Blanchet et al. (2016a) : the relative Root Mean Square Error (rRMSE) and the relative bias (rBIAS), respectively given by

$$\mathrm{rRMSE}_i(D) = \left\{ n_i(D) \sum_{T_R} \left[\frac{m_{i,D,T_R} - \widehat{m_{i,D,T_R}}}{\sum_{T'_R} m_{i,D,T'_R}} \right]^2 \right\}^{1/2}, \tag{II.15}$$

and,

$$\mathrm{rBIAS}_i(D) = \sum_{T_R} \left[\frac{m_{i,D,T_R} - \widehat{m_{i,D,T_R}}}{\sum_{T'_R} m_{i,D,T'_R}} \right], \tag{II.16}$$

where m_{i,D,T_R} is the empirical T_R-year return level for duration D and station i and $\widehat{m_{i,D,T_R}}$ is its estimation. The closer rBIAS and rRMSE to zero, the better the fit. We find that, under both frameworks, the absolute value of rBIAS is no bigger than 12% for 95% of the stations and rRMSE is no bigger that 26% for 95% of the data. This is of the same order as the values found in Blanchet

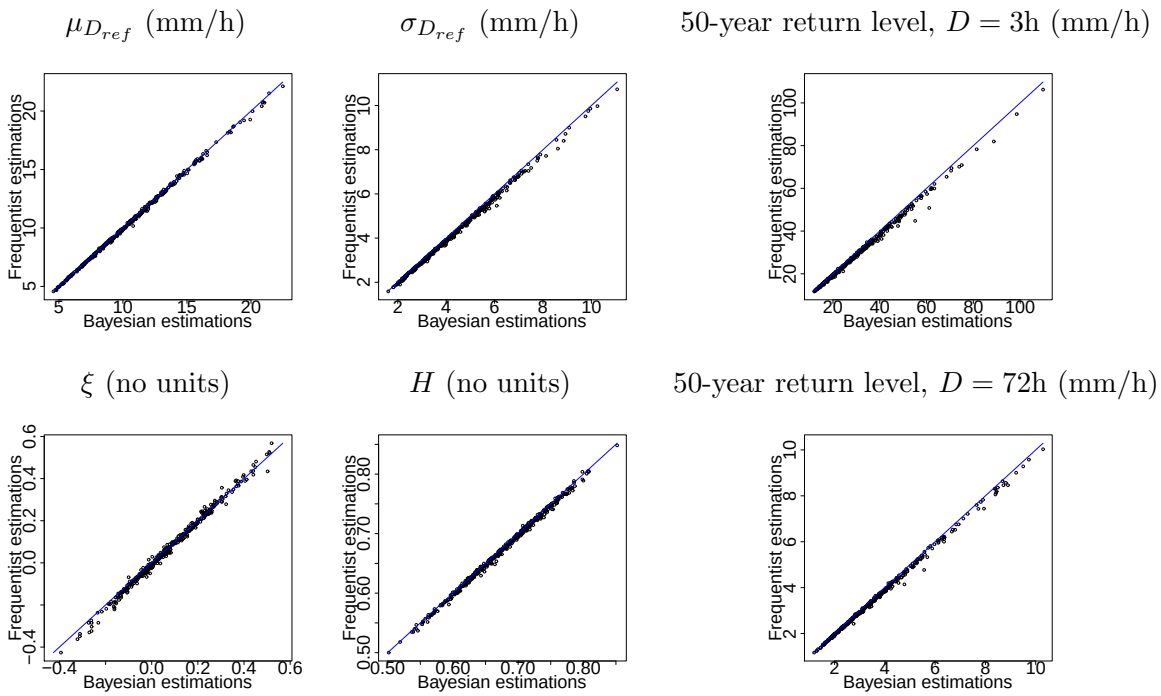

FIGURE II.5 – Scatter plot of the Bayesian (posterior mean) and frequentist (maximum likelihood), for $\mu_{D_{ref}}$, $\sigma_{D_{ref}}$, ξ, H and for the 2- and 50-year return levels at 3h and 72h durations.

et al. (2016a) on part of the region but using daily data on a much longer observation period (about 60 years).

6.1.2. Spatial variability of return level across durations

Fig. II.6 displays the posterior mean estimations of the 2- and 50-year return levels at 3h and 72h durations. Fig. II.6 shows that the 2- and 50-year return levels behave differently as the duration increases from 3h to 72h. Considering the 2-year return level, the largest values at 3h duration are found in the foothill around the town of Alès and along the overhanging Massif Central crest. Increasing the duration to 72h, the largest values are still found along the crest but, comparatively, the 2-year return level fade in the foothill.

Rainfall events featuring a 2-year return period are quite common as by definition they tend to occur regularly in one's life (every two years on average). Molinié et al. (2012) characterize the rainfall regimes in the Massif Central region. They show that the largest rainfalls at hourly duration usually occur both over the foothill and over the Massif Central crest. The rainfall characteristics are those of convective storms in terms of intermittency, diurnal cycle and spatial pattern. Increasing the duration to 72h, one may hypothesize that there is no stationary forcing of rainfall over the foothill, while the mountain crest or slope may continue to trigger rainfall if humidity remains sufficient. Molinié et al. (2012) shows that the spatial pattern of rainfall at daily duration over the mountain is similar to those of cellular storms.

Focussing on the 50-years return level, the largest values at 3h duration are found only in the foothill, while they extend over the mountain range at 72h duration. The persistence of large rainfall over the foothill during several hours requires an exceptional forcing in agreement with the exceptional characteristics of the 50-year return level event, which occur seldom in one's life (in average every 50

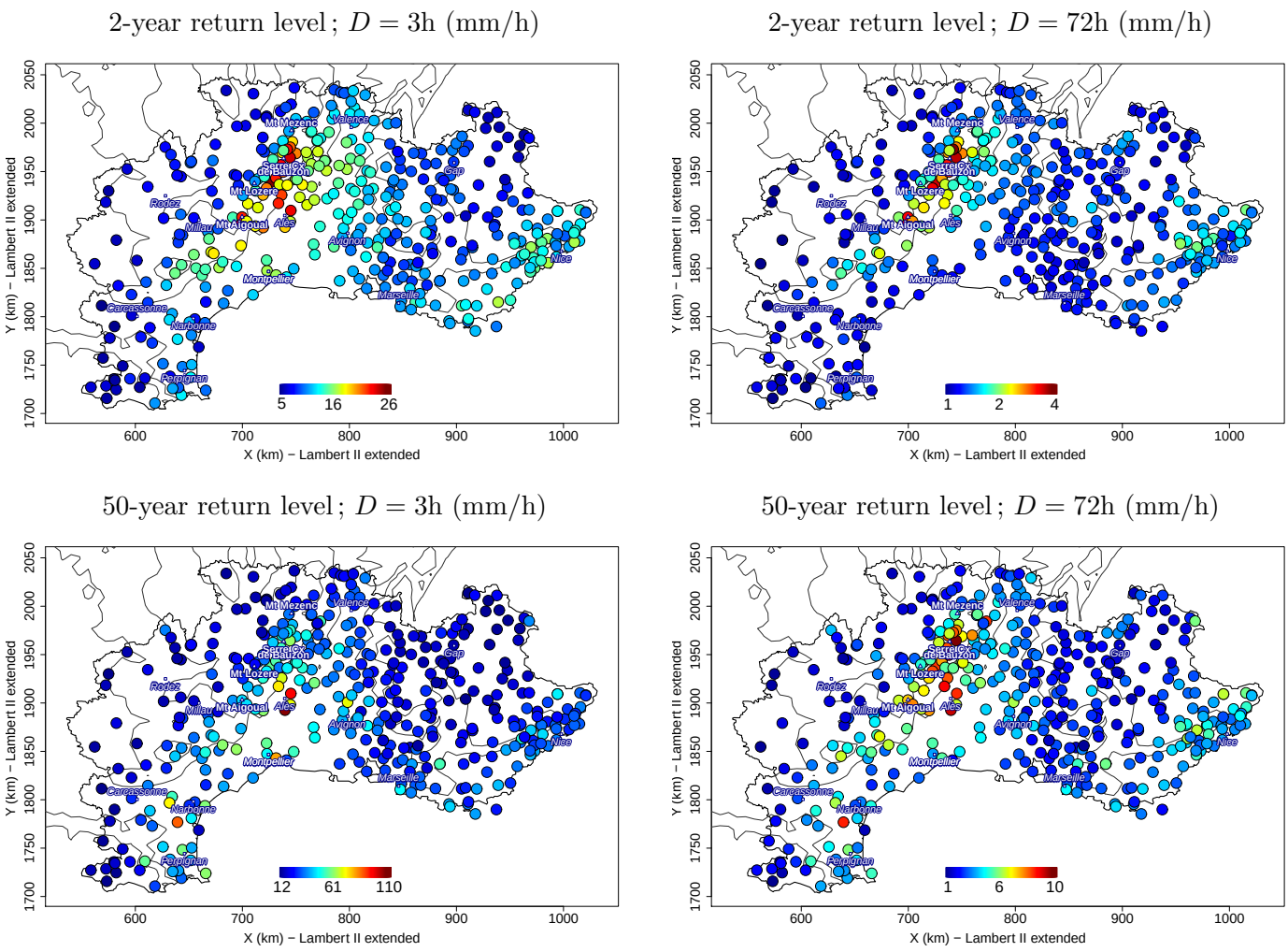

FIGURE II.6 – Posterior mean estimation of the 2- and 50-year return levels (mm/h) at 3h and 72h durations.

years). Example of such forcing is the cold pool thermal forcing described in Ducrocq et al. (2008). Other configurations producing severe and long lasting rainfall events have been observed during the HyMeX field campaign (Ducrocq et al., 2013; Drobinski et al., 2014). For example Bousquet et al. (2013) describes a mesoscale convective system impinging the Massif Central range from the west and producing a bow of heavy rainfall cells over the foothill. A different kind of precipitating system yielding large rainfall during periods of tens of hours over the Massif central crest is stationary shallow convective system (Miniscloux et al., 2001; Anquetin et al., 2003). This shallow convection may be combined with deep convection during several hours. Godart et al. (2011) shows that 40% of the largest daily rainfalls over the Massif central crest are produced by such systems.

6.1.3. Temporal variability of extreme rainfall

Eqs. (II.5) or (II.10) show that the T_R-year return levels at duration D is nothing else than the T_R-year return level at the reference duration D_{ref} multiplied by $(D/D')^{-H}$, for any D, D' and T_R. Note that the multiplying factor is independent on T_R, so it applies equally to any quantile. Case $H = 0$ corresponds to uniform rainfall with equal intensity whatever the duration. Case $H = 1$ corresponds to rainfall tending to concentrate in D_{ref} hours. Cases $0 < H < 1$ correspond to intermediate cases between uniform and concentrated rainfall. The closer H to one, the more rainfall tends to concentrate

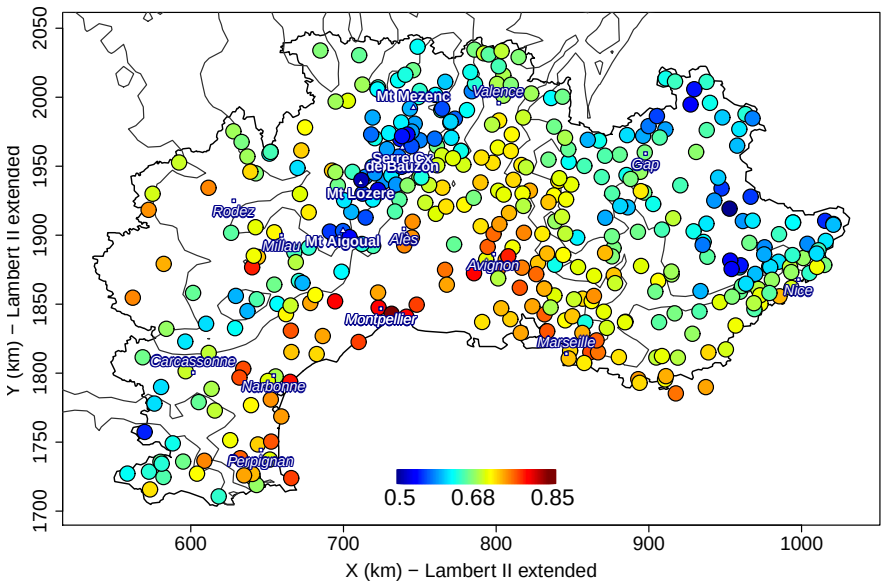

FIGURE II.7 – Posterior mean estimation of the scaling parameter H (no units).

in few hours. So H informs on the temporal variability of extreme rainfall. Fig. II.7 displays the posterior mean estimations of H in the region. The largest H are found along the Mediterranean coast between Perpignan and Marseille and along the Rhône valley ($0.7 - 0.85$). The lowest values are found along the Massif Central crest and in the south eastern Alps (H around 0.5). Thus two different extreme rainfall regimes are identified : i) mainly short and intense rainfall events along the Mediterranean shore and in the wide plain of the Rhône valley, which are likely to be controlled by deep convection, and ii) mainly long and regular rainfall events along the Massif Central crest and slope, which force stationary shallow or deep convection.

6.2. IDF uncertainty

6.2.1. The example of Montpellier

Before comparing the density estimates obtained with the different frameworks over the whole region, we start illustrating results on the station of Montpellier. This station is chosen because i) it shows among the largest values of 3h-rainfall intensity (84 mm/h at 3h duration, in autumn 2014), ii) Montpellier is a good illustration of the temporal variability of extreme rainfall : the median value of annual maximum 3h-rainfall intensity (15mm/h at 3h duration) is 50% bigger than the median value over the region (10mm/h at 3h duration), whereas at 72h duration it equals the regional median (1.25 mm/h at 72h duration), and iii) its population is among the biggest in the region (more than $250,000$ inhabitants in 2010), which make it a sensible case of risk analysis. Fig. II.8 compares the density estimates of the parameters and 50-year return levels at 3h and 72h durations. In the frequentist framework, densities are obtained with either the theorem of asymptotic normality -in which case densities are Gaussian-, or the bootstrap resampling method. For the Bayesian framework, the posterior density is depicted. Fig. II.8 illustrates that the posterior and bootstrap densities are able to better adjust to the data by being able to produce asymmetric densities with several modes. The posterior density of H departs particularly from the bell-like shape of a Gaussian with a flattened

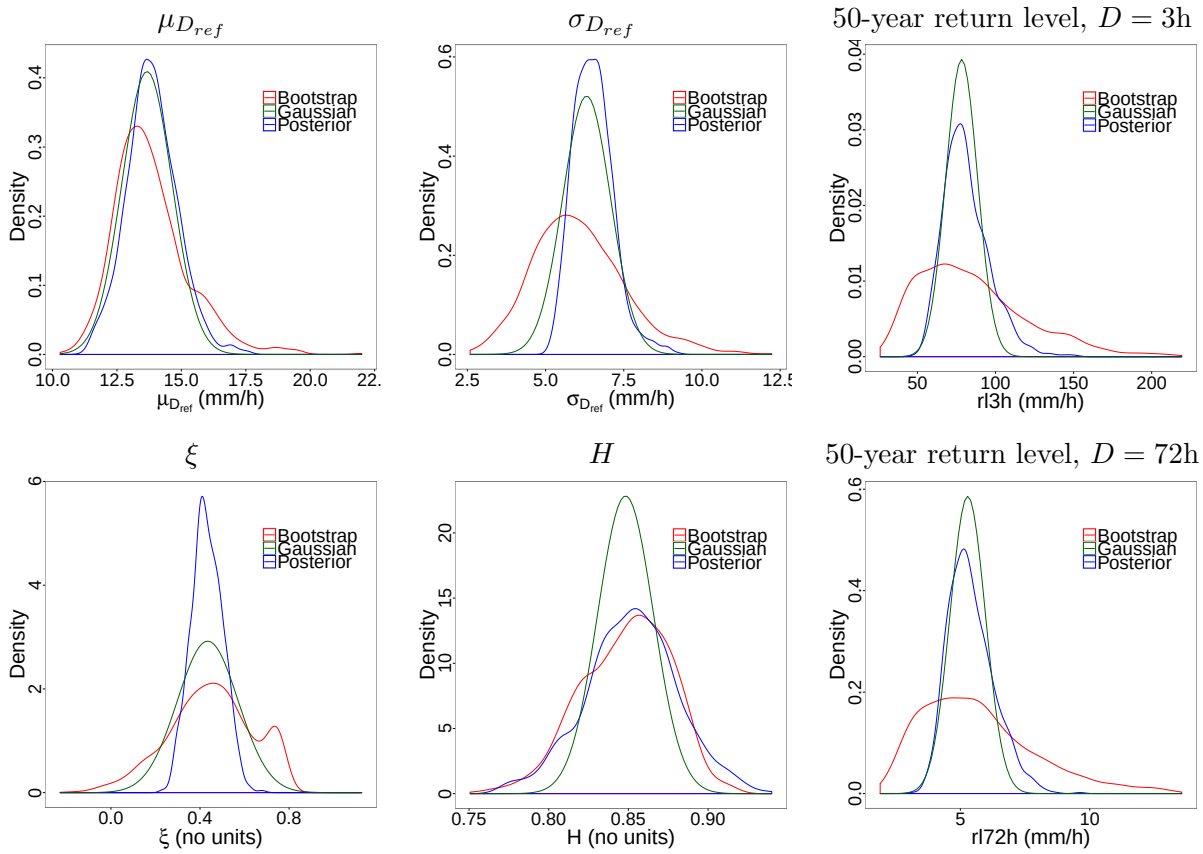

FIGURE II.8 – Density estimates of the model parameters and the 50-year return levels at 3h and 72h durations, for Montpellier station. Frequentist densities are obtained with the theorem of asymptotic normality (green) and the bootstrap resampling method (red). Bayesian densities are the posterior densities (blue).

peak between 0.83 and 0.87, which cannot be seen by application of the asymptotic normality theorem. The bootstrap method, on the opposite, produces similar density of H to the posterior density. Some asymmetry with respect to the mode is also found for ξ in the posterior density and even more in the bootstrap density. This produces asymmetry in return levels with a heavier right tails for the bootstrap and posterior densities than for the Gaussian density, whereas the left tails of the posterior and Gaussian densities are similar. Therefore the bootstrap and Bayesian methods are able to tell there is a greater likelihood for the 50-year return level to be over than under the estimated value, which is not possible when considering symmetric Gaussian densities.

The return level plot of Fig. II.9 illustrates this asymmetry in the uncertainty of return levels for the bootstrap and posterior densities, particularly for large return periods. Whatever the return period, the {lower bound of the posterior and Gaussian confidence intervals are equal, whereas the upper bound differs significantly. We can thus postulate that, by imposing symmetry, the asymptotic normality theorem tends to underestimate the upper bound of the confidence interval. The bootstrap method allows asymmetry, however it gives much wider confidence intervals than the two other methods, even for the lower bound. Comparing the bootstrap and posterior densities in Fig. II.8 shows that difference in the width of the confidence intervals is mainly due to differences in the scale $\sigma_{D_{ref}}$ and shape ξ parameters.

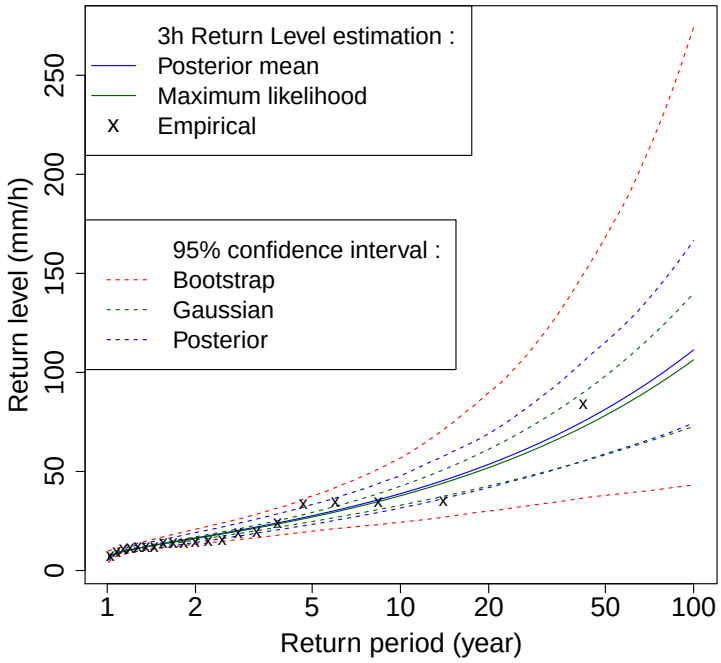

FIGURE II.9 – Return level plot at 3h duration. The crosses show the empirical values and the lines the predicted values in the frequentist (green) and Bayesian (blue) framework. The dotted lines are the 95% confidence intervals associated to the Gaussian (green), bootstrap (red) and posterior (blue) densities.

6.2.2. Regional study

The example of Montpellier showed asymmetry of the bootstrap and posterior densities, which is a good sign that these methods allow to better adjust uncertainty estimation to the data. To document this feature at the region scale, we compute the skewness s of the estimated densities at each station. If $s = 0$, the density is symmetric (as in the Gaussian case). If $s > 0$ the density is asymmetric and the right tail is heavier than the left tail. If $s < 0$, it is the opposite. The further s from zero, the greater the asymmetry. Fig. II.10 shows the skewness of the bootstrap and Bayesian densities. For sake of readability, we represent the Kernel densities of the skewness and restrict the x-axis to comprise 95% of the values. For the GEV parameters, most skewness of the posterior densities are positive, meaning heavier right tails. This also applies for the bootstrap densities but to a lesser extent for ξ. For the scaling parameter, both left and right heavy tails are found with both methods. For the return levels, mainly positive skewness are found, corroborating what was found for the station of Montpellier in Section 6.2.1. For the great majority of the stations, there is a greater likelihood for the 50-year return level to be over than under its estimated value. This piece of information is of great importance for risk management and is missing when considering symmetric Gaussian densities according to the asymptotic normality theorem. Bootstrap skewness of all variables often largely exceed the Bayesian values. We can postulate that the bootstrap method tends to give too heavy right-tailed densities and are not recommended for the computation of uncertainty. The main reason is that the number of observed years per station is too small (20 years on average), while bootstrapping requires long series. To illustrate this, we compare in Fig. II.11 the normalized range of 95% confidence interval of 50-year return level at 3h duration in the Bayesian and bootstrap cases.

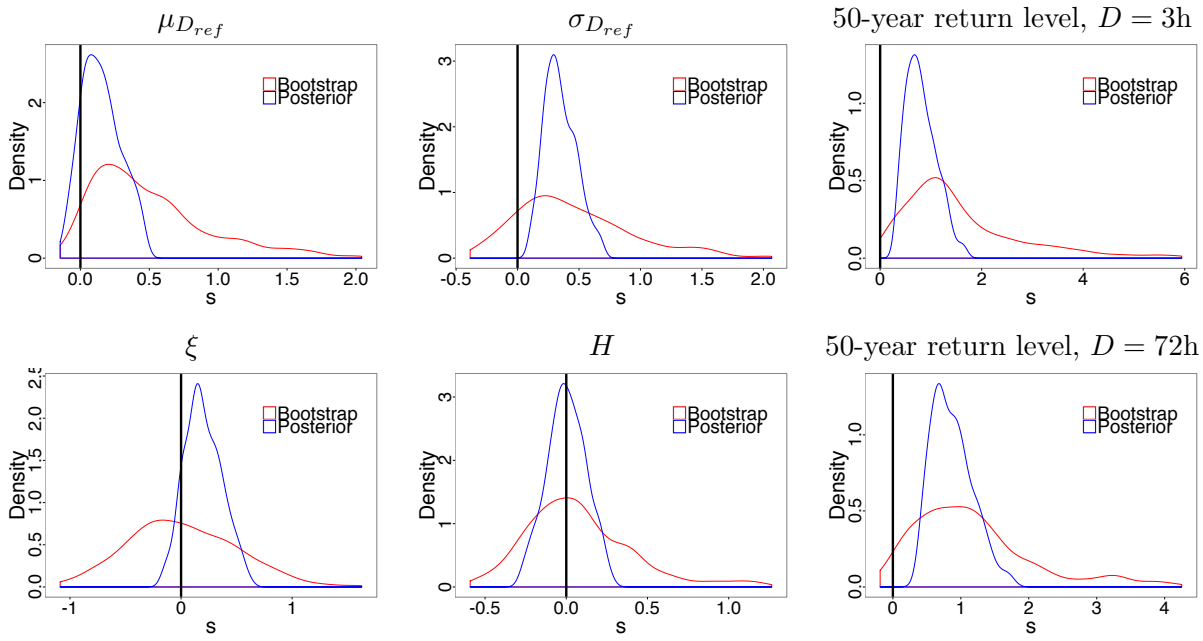

FIGURE II.10 – Skewness of the bootstrap (red) and posterior densities (blue) of the model parameters and the 50-year return levels at 3h and 72h durations. The black vertical line at 0 corresponds to symmetric density, as the Gaussian density.

The normalized range is obtained by dividing the 95% confidence interval by either the maximum likelihood estimate (in the bootstrap case) or the posterior mean (in the Bayesian case). Fig. II.11 illustrates that bootstrap uncertainty estimation is much more sensitive to the number of data than the Bayesian estimation, confirming that bootstrapping requires long series to work well, while the Bayesian estimation is much more robust. On the opposite there is no way of knowing whether the Bayesian confidence bands are too narrow but checking the return level plots of a large number of stations revealed that very few empirical estimates lie outside the 95% Bayesian confidence bands, which seems to confirm that Bayesian uncertainty estimation is reasonable.

We conclude this analysis by comparing uncertainty in 50-year return levels obtained from the Gaussian and posterior densities. We discard the bootstrap densities, which are often not reasonable. Fig. II.12 compares the lower and upper bounds of the 95% confidence interval of the Gaussian and posterior densities at 3h duration. It shows that the lower bounds are usually similar in both cases whereas the upper bounds of the posterior density are always greater. This corroborates the results found for the station of Montpellier in Section 6.2.1 : the Bayesian framework allows to obtain asymmetric confidence bands extending further to large values. We conclude from Fig. II.12 that the Gaussian density tends to underestimate uncertainty across the whole region.

7. Conclusion

We conducted in this paper a regional study on the impact of using either a frequentist or Bayesian framework in the estimation of Intensity-Duration-Frequency relationships and subsequent uncertainty. Our analysis was applied to a large database covering a large Mediterranean region with contrasted rainfall regimes. It was shown that estimation is not very sensitive to the choice of framework if the starting point is chosen with care. Uncertainty estimation, however, depends on

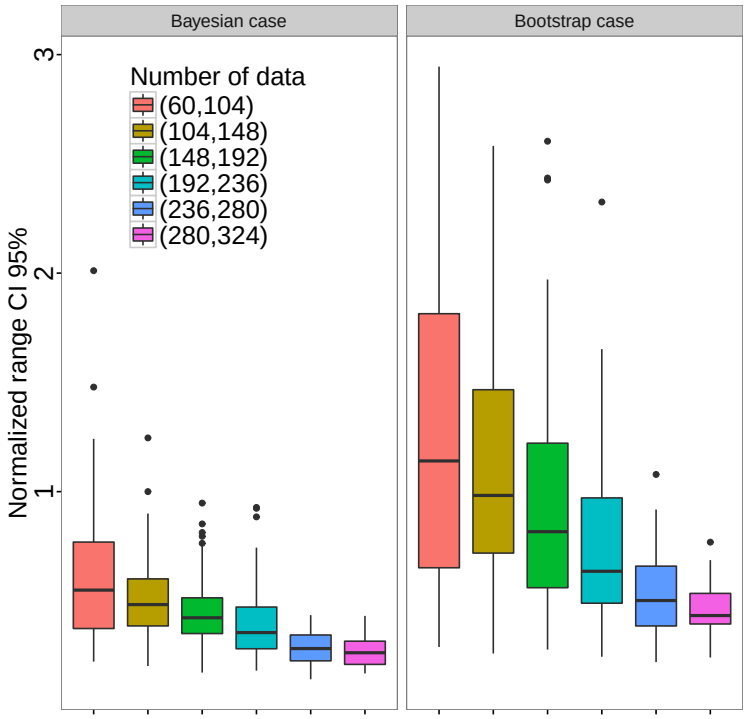

FIGURE II.11 – Boxplot of the normalized range of 95% confidence interval of 50-year return level at 3h duration obtained in the Bayesian case (left) and in the bootstrap case (right). Different boxplots are drawn depending on the number of data per station, summing the observed years of the nine durations.

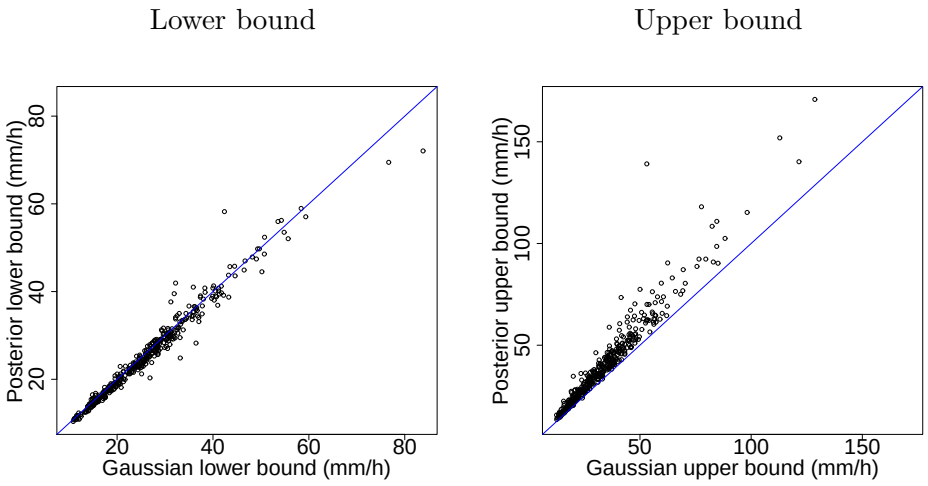

FIGURE II.12 – Bounds of 95% confidence interval of Gaussian density versus bounds of 95% confidence interval of posterior density of 50-year return level at 3h duration.

both framework and estimation method. It was shown that the posterior density (in the Bayesian framework) and the bootstrap density (in the frequentist framework) are able to better adjust uncertainty estimation to the data than the Gaussian density stemming for the asymptotic normality theorem (in the frequentist framework). They are in particular able to produce multi-modal asymmetric densities. However the bootstrap density tends to give unreasonable confidence intervals, in particular for return levels associated to large return period. The main reason is that the number of observed years per station is too small (20 years on average), while bootstrapping requires long series to work well. On the opposite there is no way of knowing whether the Bayesian confidence bands are too narrow but checking the return level plots of a large number of stations revealed that very few empirical estimates lie outside the 95% Bayesian confidence bands, which seems to confirm that Bayesian uncertainty estimation is pretty reasonable. By imposing symmetric confidence intervals, the Gaussian density tends to underestimate to upper bounds of the confidence intervals, which is an issue for risk management. The lack of objectivity of the Bayesian framework is the principal argument of those who rejects this framework (Efron, 2005), but this criticism does not apply to this work, which was conducted using very weakly subjective priors. Therefore our recommendation goes towards the use of the Bayesian framework to compute uncertainty because i) it better adjusts uncertainty computation to the data, and ii) it gives reasonable estimates of uncertainty. Our analysis further highlighted that uncertainty estimation is particularly important in IDF estimation in order to avoid over-optimistic results. For instance, in our case study, there is on average 95% chance for the 50-year return level to be between -20% and +30% of its estimation. Since current infrastructure dealing with flooding and precipitation (e.g. dams or dikes) are based on IDF curves, ignoring this uncertainty would result in large underestimation of flood risk and failure risk of critical infrastructures.

Although the Bayesian framework revealed to give reasonable estimates of IDF relationships and related uncertainties, estimation could be improved in two ways. First, relaxing the hypothesis of independence between durations assumed in this study. Although this hypothesis does not impact the estimation of IDF curves, it may have some impact on their uncertainty. However taking into account dependence between durations is not straightforward. Extreme value theory insures that dependence modelling between the continuum of durations should rely on max-stable processes, which are difficult to estimate in the frequentist framework (Davison et al., 2012), and even more in a Bayesian framework (Ribatet et al., 2012). To the best of our knowledge, max-stable processes have never been used in IDF estimation. This may be the subject of future work. Second improvement regards the consideration of nonstationarity of IDF curves in a context of global warming, for example by considering time-varying IDF relationships as in Cheng and AghaKouchak (2014) or Sarhadi and Soulis (2017), or, even better maybe, by considering covariations in temperature or other climate-related variable. A stationary assumption in a framework of nonstationarities may lead to underestimation of extreme precipitation, and therefore underestimation of flood risk or failure risk in infrastructure systems (Cheng and AghaKouchak, 2014; Sarhadi and Soulis, 2017). However nonstationarity in extreme precipitation seems not to be obvious for the studied region at daily time step (Blanchet et al., 2016b). Furthermore accounting for nonstationarity at subdaily scales would require much longer time series than those available so far for the region, which are most of the time less than 20-years long.

Chapitre *III*

A regional scale-invariant extreme value model of rainfall Intensity-Duration-Area-Frequency relationships

---

A regional scale-invariant extreme value model of rainfall Intensity-Duration-Area-Frequency relationships

Victor Mélèse[1], Juliette Blanchet[1], Jean-Dominique Creutin [1]

[1] *UGA - IGE CS 40700 38 058 Grenoble Cedex 9, France*

Article soumis dans *Water Resources Research*.

Abstract

We propose in this article a regional study of Intensity-Duration-Area-Frequency (IDAF) relationships of annual rainfall maxima in southern France. For this we develop a regional extreme value IDAF model based on space-time scale invariance hypotheses. The model allows us to link the statistical distributions of rainfall maxima over any duration and area. It provides in particular an analytical expression of the Areal Reduction Factor (ARF), which expresses how the statistical distribution of rainfall maxima changes as the area increases, for any fixed duration. It also provides an analytical expression of areal return level for the continuum of area and duration. The model is applied to radar reanalysis data covering a 13,000 km^2 region of southern France featuring contrasted rainfall regimes (2008-2015). We estimate the IDAF relationships centered on any radar pixel of the region in the range 3-48 h and 1-2025 km^2. We obtain in particular a spatial distribution of the ARF, which allows us to distinguish different rainfall regimes in the region. The overall IDAF model provides also a regional quantification of areal rainfall risk by allowing the computation of rainfall return level maps for any area and duration in the applicable range. Despite inevitable sampling issues due to the shortness of the data sample, we highlight important differences in the spatial distribution of areal rainfall risk depending on the area and duration, illustrating that a comprehensive storm risk evaluation should consider the continuum of area and duration rather than arbitrarily predefined ones.

1. Introduction

Protecting people and infrastructures against potential damages caused by storm floods has long been a sensitive sociotechnical issue. A statistical measure of storm risk is the frequency of occurrence - or equivalently the return period - of a given rainfall amount at a given location. Since rainfall accumulates over river basins in space and time, a meaningful risk evaluation involves the computation of return levels as a function of area and duration. Relationships between duration, area and return level are called the Intensity-Duration-Area-Frequency (IDAF) curves, a mere extension of Intensity-Duration-Frequency (IDF) curves when considering areal rainfall. A particular ingredient of IDAF curves is the Areal Reduction Factor (ARF), which is defined as the multiplicative factor allowing the transformation of point rainfall return levels to areal rainfall return levels, for a given return period , duration and location.

Different methods have been proposed in the literature to compute ARFs (see Svensson and Jones, 2010, for a comprehensive review). They can be classified into three main categories. First, empirical methods derive the ARFs as the ratio of the empirical return levels of areal and point rainfall (Omolayo, 1993; Durrans et al., 2002; Allen and Degaetano, 2005; Lombardo et al., 2006; Eggert et al., 2015). Second, analytical expression of ARFs are derived based on the spatial correlation structure of point rainfall (Iturbe and Mejìa, 1974; Lebel and Laborde, 1988; Sivapalan and Blöschl, 1998). The major advantage of this approach is that it does not necessitate areal rainfall data since the spatial correlation structure of rainfall can be estimated from gauge data. However a non-negligible drawback is that the estimated ARFs strongly depend on the choice of the spatial correlogram function, as noted in Pavlovic et al. (2016). Third, several studies have developed purely data-driven models, proposing analytical expressions of ARFs as parametric functions of area and duration. A variety of expressions have been proposed depending on the case study (Yoo et al., 2007; Olivera et al., 2008; Mineo et al., 2018), making the generality of the proposed formulations in other parts of the world debatable.

The studies modeling IDAF relationships combine ARF computations and quantile models through statistical distributions. They can be classified into two main categories. First, purely data-driven IDAF models estimate the link between the statistical distributions of space-time rainfall extremes using area and duration as covariates in the statistical distributions (such as in Overeem et al., 2010). Second, more physically-based IDAF models use the structural properties of rainfields in both space and time (De Michele et al., 2001; Veneziano and Langousis, 2005; Nhat et al., 2007). In particular De Michele et al. (2001) build an IDAF model based on dynamic scaling hypothesis of space-time rainfields, as evidenced in Venugopal et al. (1999), combined with simple scaling hypothesis of point rainfall. This model is applied in southern France by Ceresetti et al. (2012) and in western Africa by Panthou et al. (2014). The model of De Michele et al. (2001) shows the advantage over Overeem et al. (2010) of relying on theoretical arguments related to physics (space-time scaling properties), whereas the model of Overeem et al. (2010) is purely data-driven with no physical assumptions (in the scaling sense). However scaling assumptions may sometimes be too strong. In particular, De Michele et al. (2002) and De Michele et al. (2011) relax the simple scaling hypothesis under lognormal distributions.

The great majority of IDAF studies considers spatial homogeneity of rainfall distribution over the region, meaning that a single IDAF model is estimated for the whole region. Although this is

reasonable for small regions (De Michele et al., 2001, 2002) or flat regions with little rainfall variability (Overeem et al., 2010; Panthou et al., 2014), this is more debatable in hilly terrains where orography may induce anisotropy and may increase the temporal persistence of rainfields. This leads Ceresetti et al. (2012) to split a region of southern France into two domains - a flat subregion and a rugged subregion - that are both assumed to be homogeneous in terms of extreme rainfall regime. However this division into subregions based on geographical considerations was not really tested.

This article extends the work of Ceresetti et al. (2012) by studying IDAF relationships of annual rainfall maxima over the same region but without assuming spatial homogeneity of rainfall distribution. IDAF relationships estimated at every grid point of the region allow us to document more precisely than in Ceresetti et al. (2012) the rainfall regimes in the region. Allowing for non homogeneity of rainfall and increased flexibility, our IDAF model combines a modified dynamic scaling hypothesis of rainfields with a simple scaling hypothesis of point rainfall. The model of De Michele et al. (2001) becomes a special case of our formulation.

The data are presented in Section 2. Two IDAF relationships are derived in Section 3, following respectively the space-time scaling assumptions of De Michele et al. (2001) and relaxing the dynamic scaling hypothesis for more flexibility. These distribution-free models are then combined with extreme value theory to provide two versions of Gumbel-IDAF relationships. Section 4 discusses results of these two models for the region of study. It illustrates in particular the usefulness of relaxing the dynamic scaling hypothesis of De Michele et al. (2001) for part of the region. Using this more flexible model, we highlight and discuss different rainfall regimes in the region, as well as different storm risk, keeping however in mind the limits of the study in terms of sampling fluctuations, particularly in the foothills.

2. Data

The region of study covers 13,000 km^2 of southern France that are under Mediterranean climatic influence (see Fig. III.1). It is limited to the south by the Mediterranean coast, to the north west by the Massif Central and to the east by the RhÃt'ne Valley. Altitude ranges from 0 to more than 1500 m.a.s.l. The mountain massifs design funnel-shaped domains that are known to experience severe storms generating flash-floods from various foothill rivers. Hydrometeorological situations leading to extreme events in the region are described in Gaume et al. (2004); Delrieu et al. (2005); Ducrocq et al. (2013); Drobinski et al. (2014).

We use high-resolution rainfall reanalysis data based on radar-raingauge merging, as described in Boudevillain et al. (2016). These reanalyses are available at 1 km^2 spatial resolution and at 1 h temporal resolution for 138 significant rain events during the 2008-2015 period. Definition of these events is described in Boudevillain et al. (2016). Briefly speaking, daily raingauges recording precipitation accumulation from 0600 to 0600 UTC are used to define rain events. Rain days are defined as the days from 0600 to 0600 with regional rainfall accumulation (summing the station values) exceeding 30 mm/day. Consecutive rain days form a rain event. For computational reasons, in this article the rainfall reanalysis database is restricted to the months of September, October and November. This restriction barely or does not affect the annual maximum values as the most extreme rainfall events occur almost always in autumn in the region. This gives 50 events whose

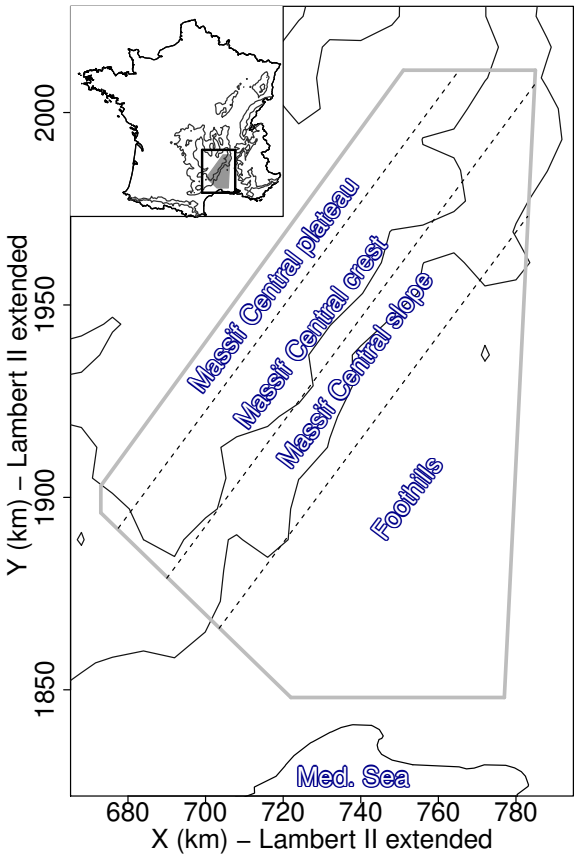

FIGURE III.1 – Maps of studied region. The top-left insert shows the location of the region in France. The black square shows the domain of Boudevillain et al. (2016) where the reanalysis data are available. The gray domain shows the location of the pixels at which the IDAF models are estimated. The black dashed lines in the main map roughly delineate the main parts of the studied region (note that the Massif Central plateau extends much beyond the indicated band). The topography is represented by the the 400 and 800 m.a.s.l isocontours.

duration varies between a few hours to more than 8 successive days. In order to focus on the area featuring the strongest rainfall variability (see Fig. 10 of Blanchet et al., 2016a), we restrict the region of Boudevillain et al. (2016) to the Massif Central plateau, the Massif Central crest, the slope and the foothills (right panel of Fig. III.1). The study region contains 12763 pixels of 1 km^2 surface. Note that the pixels lying outside the study region will still be used for aggregating rainfall over surfaces going beyond the region, as will be explained below.

Two drawbacks of the considered database can be pointed out. First, the selection of "significant" rain events ignores rainfall data for the hours in-between the events. Given the way the events are built (Boudevillain et al., 2016), these hours of rainfall are expected to be small. However they may contribute to the temporal aggregation of rainfall and thus impact annual maximum values. A separate analysis comparing annual maximum series of 148 hourly raingauges of the region obtained when considering either the continuous or the discontinuous (i.e. event-based) times series leads us to conclude that the impact of temporal discontinuity is reasonably small for the years 2008-2015 at durations 3 to 48 h (note that we do not consider rainfall maxima at 1 and 2 h durations because they likely underestimate the true maxima given the sampling period of 1 h). Second, by studying extremes based on only eight years of data, sampling is likely to be an issue. We are aware that interpretation of the results should be interpreted with caution, however the contribution of this article may be primarily viewed as theoretical. Our new IDAF model is illustrated using the best high resolution spatio-temporal data available in our region. More reliable results would obviously greatly benefit from longer time series.

Going back to the reanalysis data, the database of areal annual maxima is computed as follows. We consider the durations 3, 4, 6, 8, 12, 16, 24, 36 and 48 h and areas 1, 9, 25, 81, 169, 361, 625, 1089, 1521 and 2025 km^2. For computational reason, we restrict the number of grid point by selecting one pixel out of 2 km in longitude and one pixel out of 3 km in latitude, ending up with 2149 pixels covering the study region. We compute the time series of areal rainfall centered on each pixel, for each pair of duration and area, considering squared surfaces centered on the focus pixel. Note that the pixels lying outside the study region are used for aggregating rainfall over surfaces going beyond the region (e.g. for the focus pixels located on the edges of the region or for the largest areas), so that all spatio-temporal scales can be computed for any pixel of the study region. Finally, we extract the annual maxima for each pair of duration and area, considering zero rain for the time steps outside the rain events. For the 8-year period period 2008-2015, we end up with $9 \times 10 \times 8 = 720$ annual maxima for each of the 2149 pixels (i.e. 8 maxima for each pair of duration and area).

Note that the choice of squared areas for rainfall integration has an impact on the annual maximum volumes and thus on the estimated model. Considering round surfaces could be another possibility but it would actually barely affect the results since circle and square have 90% overlap. Moreover Blanchet and Creutin (2017) show a strong anisotropy in rainfall extremes in the region. Thus another choice could be to consider elliptical shapes as in Kim et al. (2019) but choosing the optimal ellipses (i.e. their orientation and dilatation) would be computationally intensive given the number of durations, areas, pixels and time steps to consider. Since this article focuses more on the theory than on its operational use, squared surfaces are considered here for simplicity. However interpretation of the results should obviously keep in mind that they apply for squared surfaces.

Note also that unlike in e.g. Ceresetti et al. (2012) and Kim et al. (2019), extremes are computed at each pixel rather than at regional scale. An advantage of considering pixel maxima is that it allows us to highlight the regional variability in IDAF relationships. However a drawback of considering annual maxima rather than event maxima as in e.g. Kim et al. (2019) is that annual maximum series can theoretically correspond to different rain events, making the physical interpretation of the IDAF relationships difficult. However in our case on average 80% of the annual maxima a given year at a given location are induced by the same rain event. This means that annual maxima can mainly be interpreted as event maxima and therefore IDAF relationships can be interpreted in terms of storm features.

3. A flexible Gumbel-IDAF model

3.1. Generic IDAF relationships

The framework of the IDAF relationship considered in this article relies on two assumptions. This first one is a version of space-time dynamic scaling setting that :

$$\text{pr}\left\{\lambda^{-H} M(D,A) < x\right\} = \text{pr}\left\{M(\lambda D, \lambda^b A) < x\right\}, \tag{III.1}$$

where $M(D,A)$ is the random variable representing the annual maximum rainfall intensity for the duration D and the area A, H and b are non-negative real numbers called the scaling exponents and λ is a non-negative real number. The second assumption relies on the definition of a duration of reference D_0, taken in this article equal to the finest temporal resolution of the data, $D_0 = 3$ h. It assumes spatial scaling of rainfall for the duration of reference D_0 : for any areas A and $A_\star$,

$$\text{pr}\left\{M(D_0,A) < x\right\} = \text{pr}\left\{K_{D_0}(A,A_\star) M(D_0,A_\star) < x\right\}, \tag{III.2}$$

where K_{D_0} is a non-negative deterministic function verifying $K_{D_0}(A,A) = 1$ for any A. The subscript "D_0" intends to remind that spatial scaling is assumed for the duration D_0. We use the subscript "$\star$" to distinguish D_0 –which is fixed– from $A_\star$ –which can by any. Eq. (III.2) is used in Nhat et al. (2007) with $K_{D_0}(A,A_\star) = \left(\frac{A}{A_\star}\right)^\gamma$. The model of De Michele et al. (2001) is equivalent to consider $K_{D_0}(A,A_\star) = \left(\frac{1+\eta A^\alpha}{1+\eta A_\star^\alpha}\right)^\gamma$. In this article, we consider a more flexible version :

$$K_{D_0}(A,A_\star) = \left(\frac{1+\sum_{i=1}^R \eta_i A^{\alpha_i}}{1+\sum_{i=1}^R \eta_i A_\star^{\alpha_i}}\right)^\gamma \tag{III.3}$$

where η_i, α_i are scalars, γ is a non-negative scalar and R is a strictly positive integer. The choice of R is discussed in Section 4.1 for an illustrative example.

Combining Eqs. (III.1) and (III.2) leads to the following IDAF relationships deriving the statistical distribution of annual maximum rainfall intensity for any pair of duration and area, (D,A), from the statistical distribution of annual maximum for the duration of reference and any other area, $(D_0,A_\star)$

(see Appendix 6.1) :

$$\text{pr}\left\{M(D,A) < x\right\} = \text{pr}\left\{r_{D_0}(D,A,A_\star)M\left(D_0,A_\star\right) < x\right\}, \tag{III.4}$$

where

$$r_{D_0}(D,A,A_\star) = \left(\frac{D}{D_0}\right)^{-H}\left(\frac{1+\sum_{i=1}^{R}\omega_i(D^{-b}A)^{\alpha_i}}{1+\sum_{i=1}^{R}\omega_i(D_0^{-b}A_\star)^{\alpha_i}}\right)^{\gamma}, \tag{III.5}$$

ω_i and α_i are scalars, and b, γ are nonnegative scalars. Note that Eq. (III.4) applies for any $D, A, A_\star$, given the duration of reference D_0. We name $\Pi_{1,R}$ the model defined by Eqs. (III.4) and (III.5). The model developed in De Michele et al. (2001) corresponds to $\Pi_{1,1}$, where it is written for $A_\star = 0$. $\Pi_{1,R}$ involves more parameters for more flexibility but it satisfies the same scaling hypotheses as in De Michele et al. (2001). In particular, it defines IDF simple-scaling relationships between $M(D_0,A)$ and $M(D,A)$ when $A \approx 0$.

Combining $\Pi_{1,R}$ for $(D_0,A_\star)$, (D_0,A) and (D,A) gives (see Appendix 6.2) :

$$\text{pr}\left\{M(D,A) < x\right\} = \text{pr}\left\{ARF_{D_0}(D,A,A_\star)M\left(D,A_\star\right) < x\right\}, \tag{III.6}$$

where

$$ARF_{D_0}(D,A,A_\star) = \left(\frac{1+\sum_{i=1}^{R}\omega_i(D^{-b}A)^{\alpha_i}}{1+\sum_{i=1}^{R}\omega_i(D^{-b}A_\star)^{\alpha_i}}\right)^{\gamma}. \tag{III.7}$$

Eq. (III.6) allows us to pass from the statistical distribution of annual maximum for $(D,A_\star)$ to that for (D,A), for any $D, A, A_\star$, through the multiplicative factor $ARF_{D_0}(D,A,A_\star)$. For this reason the latter is termed the Areal Reduction Factor (ARF). Note that the ARF can be either lower than 1 -in which case ARF_{D_0} is a reduction factor-, or larger than 1 -in which case it is actually an amplification factor.

As will be illustrated in Section 4.1, the model $\Pi_{1,R}$ is able to model decreasing or increasing ARF curves but it is unable to model ARFs with changing slopes in sign with the accumulation. For this reason, for more flexibility, a second model is considered by relaxing the dynamic scaling assumptions, still considering that Eq. (III.4) holds but replacing Eq. (III.5) by

$$r_{D_0}(D,A,A_\star) = \left(\frac{D}{D_0}\right)^{-H}\left(\frac{1+\sum_{i=1}^{R}\omega_i D^{-\beta_i}A^{\alpha_i}}{1+\sum_{i=1}^{R}\omega_i D_0^{-\beta_i}A_\star^{\alpha_i}}\right)^{\gamma}. \tag{III.8}$$

where β_i is a scalar. We name $\Pi_{2,R}$ the model defined by Eq. (III.8). Case when β_i, $i = 1,\ldots,R$, are all equal corresponds to Eq. (III.5). In particular, when $R = 1$ as in De Michele et al. (2001), $\Pi_{1,1}$ and $\Pi_{2,1}$ are equivalent.

It will be shown in Section 4.1 on an illustrative example that the model $\Pi_{2,2}$ is able to satisfyingly cope with the different forms of ARFs in our region, unlike $\Pi_{1,1}$ and $\Pi_{1,2}$. However it is actually overparametrized for our data since the more parcimonious model $\Pi_{2,2}^{+}$ obtained by setting $\gamma = 1$ and $\alpha_1 = \alpha_2$ fits as well. In order to restrict the number of parameters and to consider the same family of model for the whole region, in the rest of this article, the model $\Pi_{2,2}^{+}$ is used for every pixel.

It considers that Eq. (III.4) holds with

$$r_{D_0}(D, A, A_\star) = \left(\frac{D}{D_0}\right)^{-H} \left(\frac{1 + \sum_{i=1}^{2} \omega_i D^{-\beta_i} A^{\alpha}}{1 + \sum_{i=1}^{2} \omega_i D_0^{-\beta_i} A_\star^{\alpha}}\right), \tag{III.9}$$

giving in particular

$$ARF_{D_0}(D, A, A_\star) = \frac{1 + \sum_{i=1}^{2} \omega_i D^{-\beta_i} A^{\alpha}}{1 + \sum_{i=1}^{2} \omega_i D^{-\beta_i} A_\star^{\alpha}}. \tag{III.10}$$

Note that the model $\Pi_{2,2}^{+}$ still verifies the spatial scaling assumption of Eq. (III.2) and the IDF simple-scaling relationships when $A \approx 0$. However, it does not satisfy the space-time dynamic scaling of Eq. (III.1) due to β_i. Nevertheless, it can still be referred to as a scaling model in the wider sense that according to Eq. (III.4), defining the cumulative distribution function (CDF) of annual maximum intensity for some area A_0 and the reference duration D_0 is sufficient to fully model the CDF for any other duration and area - this is the "fractal" property in the statistical sense.

3.2. Gumbel-IDAF relationships

Without loss of generality, we take the reference duration to be $A_0 = 1$ km^2, which is the finest spatial resolution of the data. As previously mentioned, according to Eq. (III.4), it is sufficient to model the CDF of (D_0,A_0) to fully model the CDF of any (D, A). The founding theorem of extreme value theory (see Coles et al., 2001) states that if independent and identically distributed data are blocked into sequences of observations and if the CDF of block maxima converges to a non degenerate distribution function as the length block increases to infinity, then the limit distribution is the Generalized Extreme Value (GEV) distribution. Applied in the finite case, this means that if each block is long enough, then the CDF of block maxima can be approximated by the GEV distribution (if convergence holds). Therefore, assuming that the autumn season is long enough, it can be considered that annual maximum rainfall intensity at the reference duration and area, $M(D_0, A_0)$, follows a GEV distribution, i.e. that :

$$\mathrm{pr}\left\{M(D_0, A_0) < x\right\} = \exp\left\{-\left(1 + \xi\frac{x - \mu_0}{\sigma_0}\right)^{-1/\xi_0}\right\}, \tag{III.11}$$

where μ_0, $\sigma_0 > 0$ and ξ_0 are scalars, called respectively the location, scale and shape parameters. A particular case of the GEV distribution is the Gumbel distribution , corresponding to (III.11) with $\xi_0 \to 0$, giving :

$$\mathrm{pr}\left\{M(D_0, A_0) < x\right\} = \exp\left[-\exp\left(-\frac{x - \mu_0}{\sigma_0}\right)\right]. \tag{III.12}$$

The Gumbel distribution is less general than the GEV and therefore it is less flexible. Papalexiou et al. (2013) show in a worldwide study that heavier-tailed distributions -such as the GEV- are in better agreement with the observed daily rainfall extremes than lighter tailed distributions -such as the Gumbel distribution. The same conclusions are reached at hourly scale for the United States in Papalexiou et al. (2018). See also Koutsoyiannis (2004a,b) for a comprehensive review. However, as will be seen in Section 4.2, the Gumbel distribution is preferable for our data owing to the difficulty in estimating the shape parameter ξ of the GEV distribution based on short records (here 8 years).

For the sake of conciseness, we assume in the rest of the article that $M(D_0, A_0)$ follows a Gumbel distribution. Equations in the GEV case can be straightforwardly derived. Eq. (III.4) associated with Eq. (III.12) implies that the annual maximum rainfall intensity, $M(D, A)$, of any duration D and area A follows a Gumbel distribution with location and scale parameter respectively given by $\mu_{D,A} = r_{D_0}(D, A, A_0)\,\mu_0$ and $\sigma_{D,A} = r_{D_0}(D, A, A_0)\,\sigma_0$ (Salvadori and De Michele, 2001; Panthou et al., 2014), where $r_{D_0}(D, A, A_0)$ is given by Eq. (III.5) for model $\Pi_{1,R}$ and Eq. (III.8) for model $\Pi_{2,R}$.

As a consequence the IDAF relationships relating the T-year return level (i.e. the quantile of order $1 - 1/T$ of the Gumbel distribution) to the duration D and the area A is given by :

$$m_{D,A,T} = r_{D_0}(D, A, A_0)\left\{\mu_0 - \sigma_0 \log\left[-\log\left(1 - \frac{1}{T}\right)\right]\right\}. \tag{III.13}$$

Note that an important difference relies in the IDAF relationships of Eq. (III.13) compared those derived in Overeem et al. (2010). The IDAF relationships derived in the latter are based on generic regression models for the extreme value model parameters, using power functions of D and A as covariates. This can be seen as a "purely" data-driven model, in which the scaling properties of the rainfields are not considered at all. As it is more constrained, our model is obviously less flexible in general. However, if the scaling assumptions it relies on are true, it is expected to be more reliable - this is the well-known biasâĂŞvariance tradeoff. Note also that it could be difficult to select a model at regional scale based on short record if no *a priori* information -such as scaling- is provided. Here we started from the strict scaling assumptions of De Michele et al. (2001) to guide our search for a more flexible model. In this sense, our model can be considered as a compromise between Overeem et al. (2010) and De Michele et al. (2001) models.

3.3. Physical meaning of the different components of the model

The Gumbel parameters μ_0 and $\sigma_0 > 0$ model the statistical distribution of rainfall intensity maxima at the finest spatio-temporal scales. The parameter μ_0 is the mode of the distribution. The larger μ_0, the larger the most likely intensity maxima at $D_0 = 3$ h and $A_0 = 1$ km^2. The parameter σ_0 is the standard deviation multiplied by $\sqrt{6}/\pi$. The larger σ_0, the larger the variability in intensity maxima at $D_0 = 3$ h and $A_0 = 1$ km^2.

When $A = A_\star \approx 0$ km^2, Eqs. (III.5) and (III.8) define IDF simple-scaling relationships between $M(D_0, 0)$ and $M(D, 0)$. Following Mélèse et al. (2018), this means that the parameter H is related to the temporal variability of extreme rainfall at the point scale, i.e. for $A \approx 0$ km^2. The closer H to one, the more extreme rainfall at local scale tends to concentrate in few hours. On the contrary, the smaller H, the more extreme rainfall is homogeneous in time.

The ARF parameters in Eq. (III.10) are difficult to interpret but the ARF relationships do have a physical meaning. Noting that

$$ARF_{D_0}(D, A, A_\star) = ARF_{D_0}(D, A, A_0)/ARF_{D_0}(D, A_\star, A_0),$$

for any $(D, A, A_\star)$, we see that the set of curves $ARF_{D_0}(\cdot, \cdot, A_0)$ fully determine any ARF relationships. For ease of conciseness and without loss of information, below and in Section 4 we restrict interpretation to the curves defined by $ARF_{D_0}(\cdot, \cdot, A_0)$. According to Eq. (III.6), the latter is the multiplicative factor allowing us to pass from the statistical distribution of extremes at the pixel scale to extremes over aggregated pixels. When $A = A_0$, we obviously have $ARF_{D_0}(D, A, A_0) = 1$, for any D. When $ARF_{D_0}(D, A, A_0) < 1$, maximum rainfall intensity at the pixel scale tends to be more intense than maximum areal rainfall around the focus pixel. This is the case when rainfalls at the pixel and in its neighborhood have roughly identical marginal distributions, i.e. in flat regions. This is also the case when the focus pixel is located in a region where rainfall is usually more intense than around, e.g. for a focus pixel located in a mountainous region over which rainfall intensifies due to orography. In this case, spatially aggregated rainfall is less intense than locally aggregated rainfall.

Although much less common in the studies to date (with the exception of Mineo et al., 2018), the case $ARF_{D_0}(D, A, A_0) > 1$ occurs when the rainfall events leading to areal extremes tend to be less intense at the pixel scale than in its neighborhood. This is typically the case for pixels located on the edge of a subregion where rainfall is usually more intense, e.g. for a focus pixel located in the foothills of a mountainous region over which rainfall intensifies due to orography. In this case, spatially aggregated rainfall is more intense than locally aggregated rainfall.

Considered as a function of A, with D hold fixed, $ARF_{D_0}(D, \cdot, A_0)$ usually decreases as A increases when $ARF_{D_0}(D, A, A_0) < 1$, while it usually increases as A increases when $ARF_{D_0}(D, A, A_0) > 1$. The rate of decrease/increase depends on both the convective signature (spatial correlation) and the rainfall drift (spatial variability).

Considered as a function of D, with A hold fixed, whatever $ARF_{D_0}(D, A, A_0)$ being lower or greater than 1, the closer the ARF values as D changes, the more homogeneous in time the storm over A. In particular storms that are stationary in time correspond to $ARF_{D_0}(D, A, A_0)$ being quite constant for all D. Reciprocally, the more short-lasting the storm, the larger the differences between $ARF_{D_0}(D, A, A_0)$ as D varies.

The above interpretations show that the ARF curves are the signature of different families of rainfall regimes, depending on whether the ARFs are lower or greater than 1 but even more depending on whether the ARFs increase or decrease with A, how fast, and how fast they change as D changes. It is however worth noting that, although usual cases show monotonic ARF curves (mainly decreasing), very specific cases in the shape of the ARF curves can also be found - in particular non monotonic curves - due to local effects (see Section 4.1 for an illustrative example).

3.4. Model estimation

Let consider a given pixel. Let $\boldsymbol{\theta}$ be the vector of model parameters at this pixel. $\boldsymbol{\theta}$ comprises the two Gumbel parameters at the duration and area of reference, together with the 6 scaling parameters $(H, \omega_1, \omega_2, \beta_1, \beta_2, \alpha)$ of $\Pi^+_{2,2}$. We estimate $\boldsymbol{\theta}$ by maximizing the model loglikelihood, using for each pixel the concatenated vector of the 720 annual maxima. The considered likelihood assumes that i) annual maxima are independent from one year to an other and ii) annual maxima of a given year at different durations and areas are independent. This second hypothesis is likely to be misspecified.

For instance an annual maximum at 4 h duration and 100 km^2 area is likely to be correlated with an annual maximum at 3 h duration and 50 km^2 area. Nevertheless modeling dependence between durations and areas complicates the model estimation and deserves a study in its own right (see Cooley et al., 2012; Davison et al., 2012; Ribatet and Sedki, 2012, for some examples of such models, but not in a multiscale framework). Furthermore Sebille et al. (2017) show in a simulation study of spatially-dependent data that modeling dependence barely improves the estimation of univariate return levels (i.e. marginal distributions) compared to the misspecified independence assumption, and could even degrade the results due to robustness and optimization issues. Therefore we believe that the hypothesis of space-time independence in the likelihood, although being misspecified, does not bias the IDAF estimation. Under the two aforementioned assumptions, the model loglikelihood writes

$$l(\boldsymbol{\theta}) = \sum_{A\in\mathcal{A}} \sum_{D\in\mathcal{D}} \sum_{y\in\mathcal{Y}} \log f_{D,A}(m_{D,A,y}), \tag{III.14}$$

where $f_{D,A}$ is the Gumbel density associated with (D, A), $m_{D,A,y}$ is the annual maximum rainfall intensity at duration D and area A for the year y and $\mathcal{D}$, $\mathcal{A}$ and $\mathcal{Y}$ are the corresponding sets of values. This gives

$$\begin{aligned} l(\boldsymbol{\theta}) = &- \sum_{A\in\mathcal{A}} \sum_{D\in\mathcal{D}} n(\mathcal{Y}) \log\{r_{D_0}(D,A)\} - \sum_{A\in\mathcal{A}} \sum_{D\in\mathcal{D}} n(\mathcal{Y}) \log(\sigma_0) - \\ &\sum_{A\in\mathcal{A}} \sum_{D\in\mathcal{D}} \sum_{y\in\mathcal{Y}} \left\{ \frac{r_{D_0}(D,A)^{-1} m_{D,A,y} - \mu_0}{\sigma_0} \right\} - \\ &\sum_{A\in\mathcal{A}} \sum_{D\in\mathcal{D}} \sum_{y\in\mathcal{Y}} \exp\left\{ -\left(\frac{r_{D_0}(D,A)^{-1} m_{D,A,y} - \mu_0}{\sigma_0} \right) \right\}, \end{aligned} \tag{III.15}$$

where $n(\mathcal{Y})$ is the number of observed years. Given the observed maxima $m_{D,A,y}$, the most likely parameters are those maximizing $l(\boldsymbol{\theta})$.

4. Results

4.1. Empirical validation of the ARF relationships

The IDAF models proposed in Section 3 are composed of two parts : i) the Gumbel model, ii) the scaling relationships defined by Eq. (III.9). This section aims at illustrating the latter. Since the temporal simple scaling assumption of point rainfall -corresponding to the term $(D/D_0)^H$- has already been validated in several studies in the region (e.g. Mélèse et al., 2018; Blanchet et al., 2016a), we focus here on the validation of the ARF model of Eq. (III.10). Because we are interested here in the ARFs only, and not in the full Gumbel-IDAF model, we temporally estimate the ARF relationships by least squares based on the empirical estimation of the ARFs. The latter are obtained by taking the empirical mean of Eq. (III.6), noting that if $\mathrm{pr}(X < x) = \mathrm{pr}(aY < x)$ for all x, then a is the ratio between the expectations of X and Y. Thus empirical ARFs at a given pixel are obtained as

$$\overline{ARF}(D, A, A_0) = \frac{\sum_y m_{D,A,y}}{\sum_y m_{D,A_0,y}}. \tag{III.16}$$

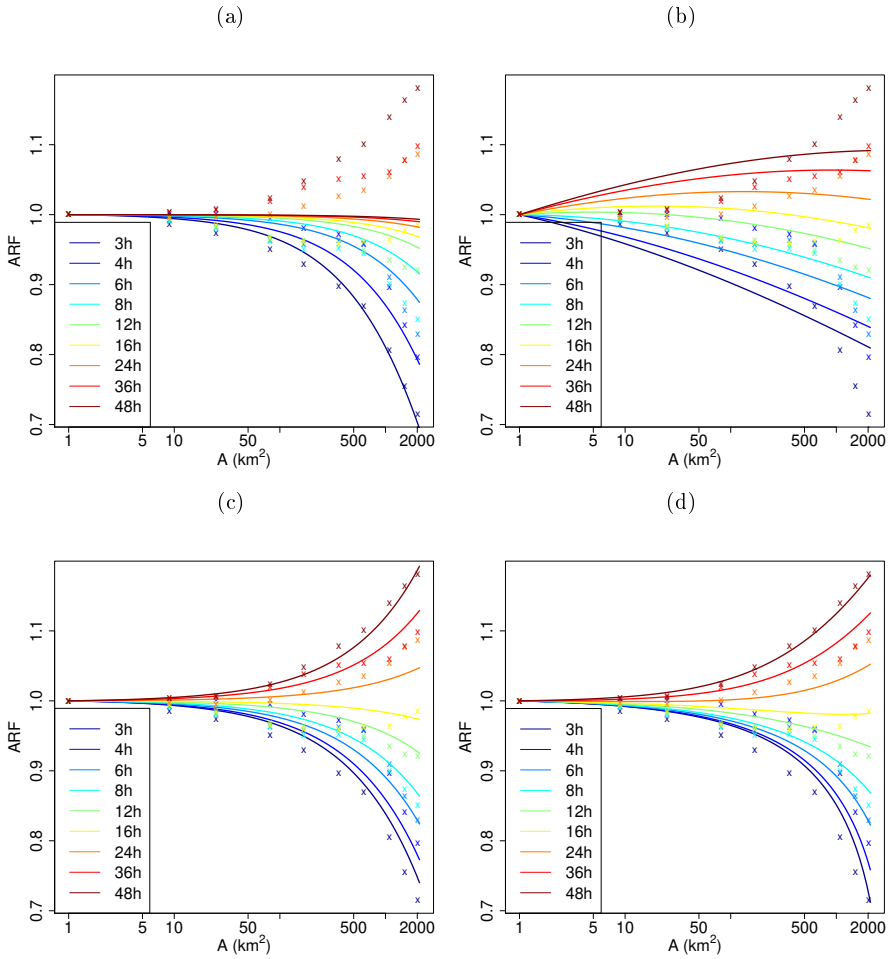

FIGURE III.2 – Empirical ARFs (crosses) and estimated ARFs (solid lines) for (a) : $\Pi_{1,1}$; (b) : $\Pi_{1,2}$; (c) $\Pi^{+}_{2,2}$; (d) $\Pi_{2,2}$

First, we exemplify the estimated ARF curves for the pixel of the city of Alès, which is chosen for illustration purpose because Alès is known to feature a strong spatio-temporal variability of extreme rainfall (Mélèse et al., 2018). For the sake of comparison, Fig. III.2 shows the estimated curves for four competing models developed in Section 3.1 : $\Pi_{1,1}$ (corresponding to the ARF modelling of De Michele et al., 2001), $\Pi_{1,2}$, $\Pi_{2,2}$ and the more parcimonious $\Pi^{+}_{2,2}$. It shows that the empirical ARFs for the pixel of the city of Alès are mostly lower than 1 for durations lower than 16 h and that they decrease as A departs from A_0. On the other hand, the empirical ARFs are mostly greater than 1 for duration greater than 24 h and they increase as A departs from A_0. Indeed, on one hand the region of Alès experiences mostly short and localized storms induced by deep convective systems, giving ARF values lower than 1 for subdaily durations, as described in Section 3.3. On the other hand, daily rainfall tends to become larger over the neighboring Massif Central slope under the orographic accumulation effect (Blanchet et al., 2016a; Mélèse et al., 2018). Since Alès is situated in the foothills of the Massif Central, ARF values are larger than 1 for $D \geq 24$ h

Fig. III.2 also shows that the model proposed by De Michele et al. (2001) ($\Pi_{1,1}$) succeeds to adjust the decreasing empirical ARFs while it fails to fit the increasing ones. Using $\Pi_{1,2}$ allows us to get increasing ARFs but large discrepancies are still found, especially for small areas. Using $\Pi_{2,2}$ or $\Pi^{+}_{2,2}$, the discrepancies wipe off and both the increasing and decreasing empirical ARFs are well adjusted.

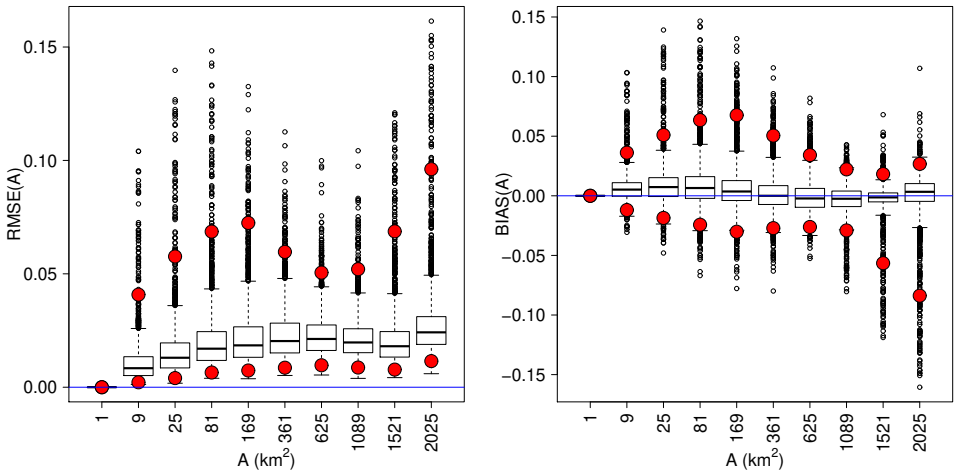

FIGURE III.3 – RMSE and BIAS between the empirical and least square estimates of ARFs. Each boxplot contains one point per pixel and observed area. The upper and lower red points in the boxplots show the quantiles of order 97.5% and 2.5%, respectively. The blue horizontal line shows the value for a perfect fit.

Note that considering $R = 3$ does not lead to better fits, neither for $\Pi_{1,R}$ nor for $\Pi_{2,R}$ (not shown). We conclude that $\Pi_{2,2}$ and $\Pi^+_{2,2}$ seem to provide the best ARF models for the city Alès. As it is more pacimonious (2 less parameters), we select the model $\Pi^+_{2,2}$ for the rest of the study, keeping in mind that it might still be overparameterized for other pixels.

In order to quantitatively validate the ARF model of $\Pi^+_{2,2}$ for all pixels, we compute the Root Mean Square Error (RMSE) and the bias (BIAS) between the empirical and least square estimates. We focus here on the evaluation as the area A varies, considering for pixel i

$$\mathrm{RMSE}_i(A) = \left\{ \frac{1}{n(\mathcal{D})} \sum_{D \in \mathcal{D}} \left(\overline{ARF}_i(D, A, A_0) - \widetilde{ARF}_i(D, A, A_0) \right)^2 \right\}^{1/2} \tag{III.17}$$

and

$$\mathrm{BIAS}_i(A) = \frac{1}{n(\mathcal{D})} \sum_{D \in \mathcal{D}} \left(\overline{ARF}_i(D, A, A_0) - \widetilde{ARF}_i(D, A, A_0) \right) \tag{III.18}$$

where $n(\mathcal{D}) = 9$ is the number of durations and $\widetilde{ARF}_i$ is the least square estimate of the ARF curve for pixel i under $\Pi^+_{2,2}$. Fig. III.3 shows that the RMSE tends to increase as the area increases but the average RMSE is no larger than 0.02, which is little relatively to the variability of the ARF curves. The bias is relatively stable with respect to the area and on average very close to 0. However we note that variability in both scores among pixels is large. The worst fits have a RMSE and an absolute bias of up to 0.15, which is quite significant. A closer look at these pixels shows even more complicated cases than Alès, with several inflection points that cannot be modeled with $R = 2$. Given the chaotic terrain of the region and the strong variability of rainfall, we judge that the RMSE and bias scores of Fig. III.3 are rather convincing, at least for 95% of the pixels. However we keep in mind that the considered model might not be flexible enough for the most complicated cases with several inflection points.

4.2. Goodness-of-fit of the Gumbel-IDAF model

The Gumbel-IDAF model of Section 3.2 (with $\Pi^{+}_{2,2}$) is estimated at each pixel by maximizing the loglikelihood of Eq. (III.15), giving one estimated Gumbel-IDAF model for each pixel. Loglikelihood optimization is based on the simplex method proposed in Nelder and Mead (1965). The Gumbel parameters μ_0 and σ_0 are initialized as the most likely parameters obtained for the reference scales D_0 and A_0. Two initializations of the parameters H, ω_i, β_i and α are considered. First, using the least square estimates of ω_i, β_i and α based on the empirical ARFs, as described in Section 4.1. In that case H is initialized following the wide sense simple scaling assumption of Gupta and Waymire (1990) as the regression slope of the logarithm of the average maxima at D and A_0 versus the logarithm of D (Panthou et al., 2014; Mélèse et al., 2018). Second, using the least square estimates of H, ω_i, β_i and α based on the empirical r factors, which are obtained from Eq. (III.10) as a ratio of averages, as for the ARFs in Eq. (III.16). Among these two possible initializations, the most likely is used, for each pixel and each model. The optimization algorithm stops when it is unable to reduce the loglikelihood of Eq. (III.15) by a factor of $10^{-8}|l(\boldsymbol{\theta})|$, giving the maximum likelihood estimate $\hat{\boldsymbol{\theta}}$.

We assess goodness-of-fit of the Gumbel-IDAF model obtained with $\hat{\boldsymbol{\theta}}$ by computing the rRMSE and the rBIAS for the data. Let $m^{(j)}_{i,D,A}$ be the j-th largest maxima in the maxima series for duration D and area A, for $j = 1, \ldots, 8$. The empirical CDF built on the 8-year maxima series for (D, A) associates the value $m^{(j)}_{i,D,A}$ to a non-exceedance probability p_j. Different definitions are possible for p_j. Here we take the probability returned by the function 'ppoints' of the R language (R Core Team, 2019). The estimated quantile associated to this probability is given by the theoretical T_j-year return level of Eq. (III.13) with $\hat{\boldsymbol{\theta}}$, where $T_j = 1/(1-p_j)$, that we note $\widehat{m_{i,D,A,T_j}}$. The scores of evaluation are based on the comparison of these two quantiles, under the rule that the closer the estimated quantiles to the empirical ones, the better the model. Of course, we face here an issue since empirical quantiles are uncertain, given that we have only 8 years of data. However this is the only reference that we can use. For the sake of concision, we focus here on the model evaluation as the area varies. In order to compare goodness-of-fit for all the pixels, we compute the relative scores obtained by dividing by the average annual maxima for the area A :

$$\mathrm{rRMSE}_i(A) = \left\{ n(\mathcal{Y}) n(\mathcal{D}) \sum_{D \in \mathcal{D}} \sum_{j=1}^{8} \left[\frac{m^{(j)}_{i,D,A} - \widehat{m_{i,D,A,T_j}}}{\sum_{D' \in \mathcal{D}} \sum_{j'=1}^{8} m^{(j')}_{i,D',A}} \right]^2 \right\}^{1/2}, \tag{III.19}$$

and

$$\mathrm{rBIAS}_i(A) = \sum_{D \in \mathcal{D}} \sum_{j=1}^{8} \left[\frac{m^{(j)}_{i,D,A} - \widehat{m_{i,D,A,T}}}{\sum_{D' \in \mathcal{D}} \sum_{j'=1}^{8} m^{(j')}_{i,D',A}} \right]. \tag{III.20}$$

In order to compare the Gumbel- and GEV-IDAF models, we show in Fig. III.4 the boxplots of the rRMSE(A) and the rBIAS(A) as A varies, in both cases. Remind that the GEV has one more parameter, namely the shape parameter ξ in Eq. (III.11). Fig. III.4 clearly shows that better scores are usually obtained with the Gumbel distribution. More precisely, the median scores are largely comparable in the two cases but the 5% worst scores (i.e. beyond the red points in the boxplots) are much worse in the GEV case. This is due to the difficulty in estimating the shape parameter based on short records (Papalexiou and Koutsoyiannis, 2013), which makes the fit fail for some pixels,

particularly for large areas. Note that quantiles are largely overestimated at these pixels (strongly negative rBIAS), with up to 40% overestimation, due to an overestimation of the shape parameter. Going back to the Gumbel case, Fig. III.4 reveals that the rRMSE(A) monotonously decreases as the area increases, particularly for the largest quantiles (e.g. the 97.5% quantile is divided by 2 between 1 and 2025 km^2). The rBIAS(A) is mainly positive for small A, meaning that the empirical return levels tend to be underestimated, whereas they are on average unbiased for the largest A. The fact that larger errors are obtained for small A might be due to the use of a Gumbel distribution, which is light-tailed, rather than a heavier tail, since Mélèse et al. (2018) evidenced heavy-tailed distribution at raingauge scale in the region for durations from 3 to 48 h (see also Papalexiou et al., 2018, for a comprehensive study of hourly rainfall across the US). For larger areas, the Gumbel distribution performs better since aggregating rainfall pixels over large areas induces Gaussian-like distributions (according to the central limit theorem), and therefore Gumbel-like distributed maxima, as assumed in our model. Another explanation might be that averaging over large areas also decreases the sampling uncertainty caused by the precipitation spatial variability (e.g. Peleg et al., 2018), making the model adjustment easier. This could explain why both the rRMSE(A) and the rBIAS(A) reduce as A increases. The question whether heavier-tailed distribution would improve the fits, in particular for small A, remains open but it would definitively require much longer data than we have here (e.g. Papalexiou et al., 2018, considers hourly raingages with at least 3,000 nonzero values, which corresponds in our region to about 28 years of data). All in all, the absolute value of rBIAS is no bigger than 16% for 95% of the pixels and rRMSE is no bigger than 32% for 95% of the pixels. Those values are only slightly larger than those found in Blanchet et al. (2016a) and Mélèse et al. (2018), although we consider here a more complex model accounting for both the temporal and spatial scaling of rainfall.

4.3. Characterization of the extreme rainfall regime of the region

Having one Gumbel-IDAF model per pixel, we now present a regional analysis of the model parameters revealing the rainfall regime of the region. We start in Section 4.3.1 with μ_0, σ_0 and H parameters characterizing the extreme values of local rainfall. We continue in Section 4.3.2 with the ARF curves, and in particular their shape, characterizing the extreme values of areal rainfall.

4.3.1. Extreme local rainfall features

Fig. III.5 displays the map of the maximum likelihood estimates of the Gumbel parameters at pixel size and 3 and 24 h duration, as well as the map of the scaling parameter H. The parameters $\mu_{24} = \mu_{24,A_0}$ and $\sigma_{24} = \sigma_{24,A_0}$ are obtained as combination of the estimated Gumbel-IDAF parameters, as described in Section 3.2. Following Section 3.3, the Gumbel parameter μ_D is related to the average of the average annual maxima at duration D, σ_D on the variability of the annual maxima from year to year at the same duration and H on the temporal variability of extreme rainfall as the duration varies. The closer H to one, the more extreme rainfall tends to concentrate in few hours. On the contrary, the smaller H, the more homogeneous in time extreme rainfall is. These parameters being intertwined, they should be interpreted jointly, each parameter bringing complementary information about the dynamics of extreme rainfall accumulation in time. We comment these maps below bearing in mind various studies conducted over western Mediterranean regions under the umbrella of HyMeX (Ducrocq et al., 2013; Drobinski et al., 2014). Basically, the extreme rainfall regime in the region is

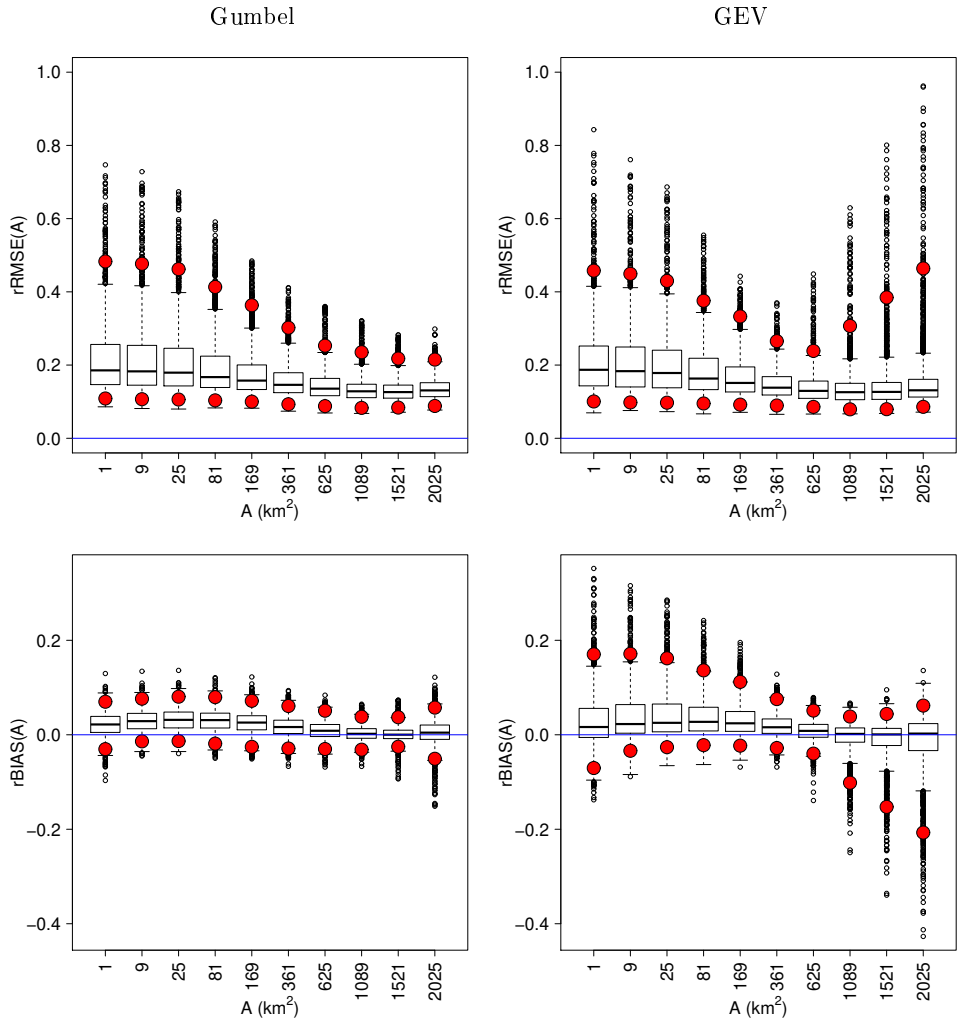

FIGURE III.4 – Boxplot of (top) rRMSE(A) versus A and (bottom) rBIAS(A) versus A, in the (left) Gumbel and (right) GEV case. Each boxplot contains one point per pixel and observed area. The upper and lower red points in the boxplots show the quantiles of order 97.5% and 2.5%, respectively. The blue horizontal line shows the value for a perfect fit.

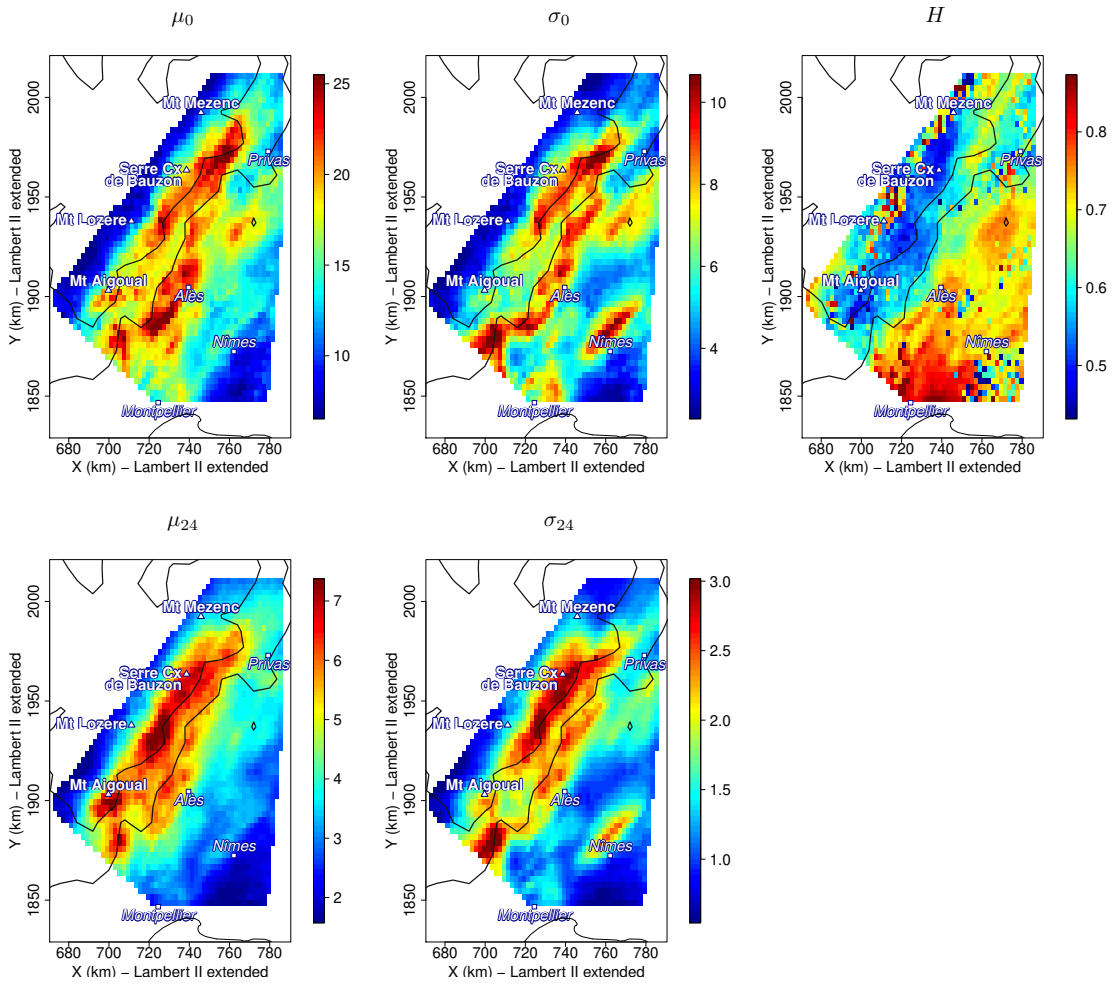

FIGURE III.5 – Top : Maximum likelihood estimates of the Gumbel parameters μ_0, σ_0 of Eq. (III.12), and of the scaling parameter H of Eq. (III.5). Bottom : Maximum likelihood estimates of the Gumbel parameters μ_{24}, σ_{24}. The 1% largest and 1% lowest values of μ, σ and H are censored to make the spatial pattern clearer. The topography is represented by the 400 and 800 m.a.s.l isocontours.

shown to be governed by Mesoscale Convective Systems (MCSs) interacting with the topography at different scales. On the one hand, the Massif Central chain itself modifies the mesoscale circulation, more or less stabilizing the MCS upstream the ridge, over the foothills (Ducrocq et al., 2008). On the other hand, the small details of the topography trigger long lasting shallow convection rainbands when exposed to the moist southern winds typical of these MCSs (Godart et al., 2009).

Focusing first on the mountainous part of the region, the map of μ_0 shows a clear dichotomy between the plateau area to the north of the crest and the rest of the region. Although our perimeter of study drastically cuts the plateau region, the sharp decrease in μ_0 clearly shows the protection by the crest from the south fluxes bringing the rainfall extremes. Moving then to the map of H, despite less organized pattern, we can see that the slope area divides the region into two opposite types of rainfall variability - along the crest and in the foothills, in good agreement with the studies mentioned above. The values of H along the crest are among the lowest of the region (around 0.4-0.5). This result corroborates the H values found in the IDF simple-scaling framework of Blanchet et al. (2016a) and Mélèse et al. (2018), where H is estimated using raingage data, corresponding to A of a few hundreds of cm^2. More importantly, this result is in accordance with the small scale

rainbands mentioned above. The map of H quite clearly delineates north-south oriented bands of rainfall temporal stability shown by low H areas around the Mont Aigoual, East of the Mont Lozère and the Serre de la Croix de Beauzon. These areas feature quite large μ_0 (around 20 mm/h/km^2) meaning that this long lasting orographic convection is able to provide subtantial annual maxima at all time scales, as shown by the map of μ_{24} in Fig. III.5. The medium values of σ at subdaily to daily scale at Mont Aigoual, growing up of about 40% in the north of the crest, deserve some remarks. Whatever the duration, the annual maxima are little variable from year to year in the south of the crest because this mountain constitutes the most southern topographic feature, i.e. the most exposed whenever a flux of humid air comes from a broad southern sector. The larger interannual variability in the north of the crest may result from a less systematic orographic effect due to the screening from topographies located upwind (Anquetin et al., 2003) or from some interference with convection of the foothills that we examine below.

The values of H in the foothills are mostly high (around 0.6-0.7 and up to 0.9), statistically pointing to rainfall accumulations from short-lasting intense storms. This result is in agreement with the occurrence of MCSs upstream the mountain ridge mentioned before. This clear difference in H leads to more contrasted patterns in μ_{24} and σ_{24} between the foothills and the crest than for μ_0 and σ_0. At 3 h duration, if we exclude the small area south-east of Nîmes, the mean rainfall annual maxima and their variance are in a similar range in a wide zone covering the foothills, the slope and the crest. On the contrary, at daily scale, the mean rainfall annual maxima and to a lesser extent their variance are systematically larger in the crest and the slope than in the foothills.

Finally, considering the maps of σ, we can speculate briefly about i) the strange "alley" of significant variance that follows quite accurately the topographical details shown by the 400 m.a.s.l. isoline, at both daily and subdaily scales and ii) the southwest-northeast oriented spots of high variance to the north of Nîmes and the far south of Privas that are much more evident at 3 h than 24 h duration. The main "alley" of high variance, that is associated to quite high means could result from low level winds deflected by the topography. They could induce a low level convergence able to preferentially trigger deep convection along this area of contact between MCSs and the mountain chain. This "alley" seems to be deflected toward west by the relief indentation of the Chaîne du Coiron to the south of Privas (up to 700 m.a.s.l.). This could make quite singular the situation around the Serre Croix de Bauzon at 3 h (large means and variances compared to the rest of the crest) where the two regimes - MCS and orographic bands - would mix. The southwest-northeast oriented spots of the Plateau Saint Nicolas, to the north of Nîmes (around 200 m.a.s.l.), and of the Berg Mountains, to the far south of Privas (up to 500 m.a.s.l.), both correspond to small topographical singularities that could play the same role of deep convection preferential triggering. We touch here the limits of the present study in terms of sampling fluctuations. We believe that the crest regime is correctly depicted with our 8 years of data but we suspect that the details of the foothill regime are much more speculative. A separate sensitivity analysis (not shown) reveals that most foothills patterns are sensitive to single events : namely September 15-21, 2014 and September 6-8, 2010 for the "alley", October 6-15, 2014 for the Plateau Saint Nicolas, and September 11-18, 2015 for the Berg Mountains. Removing one by one these events makes the corresponding pattern partly vanishing. In comparison, the mountainous part shows a remarkable stability of the maps of μ and σ to the most intense events, with the exception of the north-eastern part of the Serre Croix de Bauzon whose pattern is influenced by September

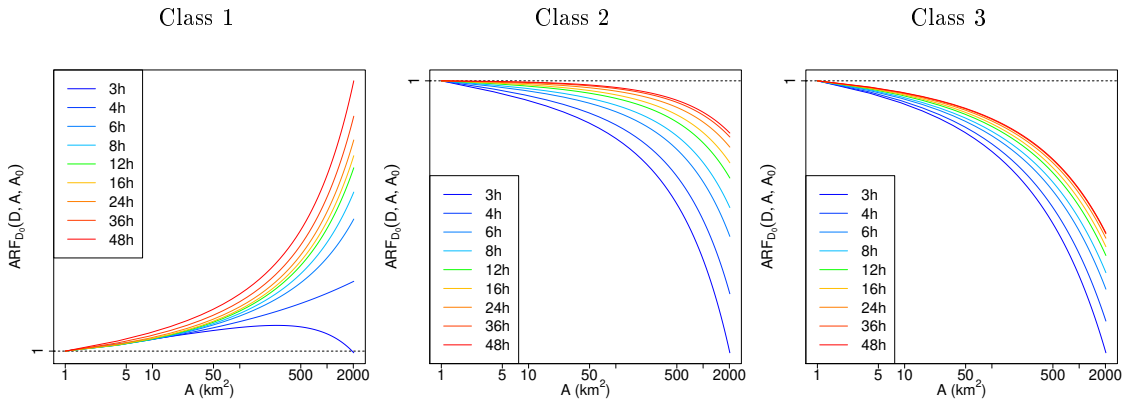

FIGURE III.6 – Shape of the $ARF_{D_0}(D, A, A_0)$ curves of each class center obtained with k-means with 3 classes. There is no value on the y-axis apart from $ARF = 1$ for $A = 1$ km^2, which always holds, because classification is based on the shape of the ARF curves, not on their absolute values.

15-21, 2014 but to a much lesser extent. Worth noticing is also the remarkable stability of the map of H all over the region, apart in the north of Montpellier.

4.3.2. Extreme areal rainfall structure

In order to summarize the spatial structure of extreme rainfall in the region, we group together the pixels having similar ARF shapes. This can be seen as the dual approach to Ceresetti et al. (2012) : whereas Ceresetti et al. (2012) assume *a priori* that the region can be subdivided into two subregions with homogeneous extreme rainfall regimes and estimate the ARFs over these two areas based on this assumption, we estimate the ARFs everywhere across the region and we look for subregions with homogeneous ARFs. Following the interpretation of the ARF of Section 3.3, we group together the pixels featuring ARFs with similar shapes rather than similar absolute values, using the k-means algorithm proposed by Hartigan and Wong (1979). We build an ARF matrix whose rows represent the 2149 selected pixels and whose columns represent the pairs (D, A) with D from 3 to 48 h with a step of 1 h and $A^{1/2}$ from 1 km to 45 km with a step of 1 km. This matrix contains then 2149 rows and 2070 columns, each row representing the values of $ARF_{D_0}(D, A, A_0)$ when A and D vary, for a given pixel. Since we are interested in the shape of the ARF curves, we normalize each row between 0 and 1. We perform a principal component analysis to reduce the matrix to 9 columns, which represents 99.9% of the explained variance. Then we apply the k-means algorithm to this matrix with a number of classes varying from 2 to 5. Below we consider the classification into 3 classes as it allows a more manageable description of the extreme rainfall structure at regional scale.

Fig. III.6 shows the normalized $ARF_{D_0}(D, A, A_0)$ curves for each of the 3 class centers. The map of the pixel classification is shown in Fig. III.7. Below we interpret the rainfall spatial features leading to these classes, focusing on the ARF shapes of the center classes. By doing so, we purposely omit the variability of the ARF curves among the classes -two pixels of the same class being interpreted has having the same ARF curves. Our goal is to interpret the broad rainfall scaling properties in space through "idealized" ARFs curves. At this point, we note that the case with ARF lower or larger than 1 depending on the duration like in Alès (Fig. III.2) is not frequent enough to appear as a class in itself, since there are only 54 such pixels (2.5% of all pixels).

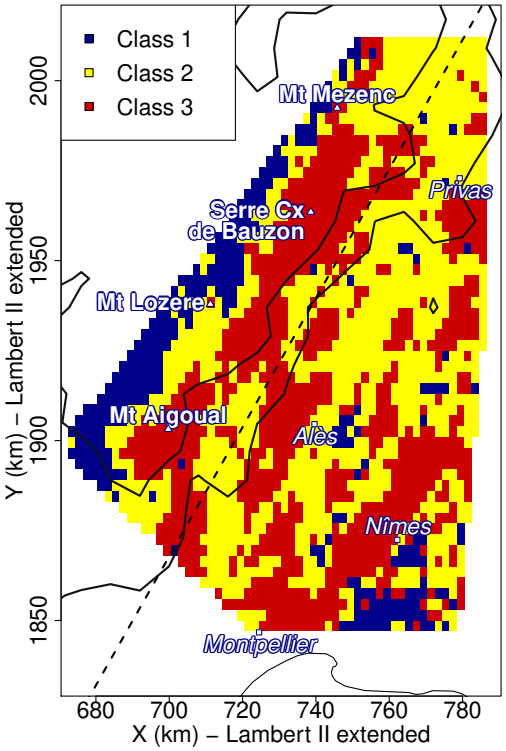

FIGURE III.7 – Pixel classification when running k-means with three classes on the normalized ARFs. Each color represents a class. The topography is represented by the 400 and 800 m.a.s.l isocontours. The dashed line delineates the two subregions of Ceresetti et al. (2012).

The classes of ARF shapes depict three typical cases. Class 1 with mainly positive slope ARFs at all time scales is typical of underexposed areas where the annual maximum values are systematically surrounded by greater neighboring maxima. Classes 2 with negative slopes getting flatter at larger time scales reflect situations where rainfall accumulation tends to smooth out the structure of extreme values in space. This âĂIJsmoothingâĂİ effect may be more or less strong, the limit being almost flat ARF curves corresponding to uniformly distributed rainfall in space. Class 3 with quite similar ARF shape at all time scales reflects situations of stable rainfall generation where the maximum values at all durations tend to display similar structure in space.

The map of ARF classes (Fig. III.7) can be analyzed following the same steps as we did for the maps of μ, σ and H in Fig. III.5. Looking first at the mountainous part of the region, the map of ARF classes confirms the protection of the plateau area by the crest. Most of Class 1 pixels are on the lee side of the crest, pointing places where extremes of spatially aggregated rainfall are more intense than extremes of locally aggregated rainfall at all time scales. A small number of Class 1 pixels to the south of Nîmes, also present on the maps of μ_0 and σ_0 (Fig. III.5), points to another underexposed zone (see for instance Fig. 2 of Blanchet and Creutin, 2017).

Moving then to the crest area, a striking resemblance with the map of H (Fig. III.5) is the north-south oriented bands around the Mont Aigoual, East of the Mont Lozère and the Serre de la Croix de Beauzon. These zones of stable time scaling (low H) appear to be stable in space structure as well (Class 3). This result is consistent with the existence around these topographic singularities of long lasting orographic convection displaying a stable structure in bands and steady rainfall rates in time. The Class 3 spots are surrounded by less stable pixels of Class 2.

Finally, considering the foothills, we are tempted to extend our speculation about âĂIJalleysâĂİ of preferential deep convection triggering made in the previous section. The "alley" with large variance around Alès feature meainly Class 3 pixels showing a significant space stability of rainfall, while the H map of Fig. III.5 indicates a medium time stability. The same is true for the two less organized spots seen before in Nîmes and Berg Mountains.

As an intermediate conclusion, we can say that the map of ARF classes (Fig. III.7), combined with the maps of μ, σ and H (Fig. III.5), reflect two levels of convection organization in space : i) the north-south oriented bands of shallow convection triggered by salient topographic details on a quite stationary mode during the south circulation situation controlling MCSs and ii) the northeast-southwest oriented alley of deep convection that follow the main orientation of the chain of mounts. It is worth remarking that this analysis is not fully consistent with the analysis of the co-occurrence of daily extremes from raingage data in Blanchet and Creutin (2017) that finds a general northeast-southwest structure over the crest like over the foothills. We believe so far that is the merit of using radar data that made possible to see the effect of topographic details. Let us also note that the speed of decrease and variability in the ARF curves are influenced by the shape considered for the spatial aggregation, which is squared in our case. For comparison with Ceresetti et al. (2012), the dashed line in Fig. III.7 shows the subdivision they considered that quite nicely separate the two convection organizations mentioned above. Nevertheless, within these regions the hypothesis of homogeneous ARF shapes they made looks questionable, as far as the local detail of the extreme rainfall risk matters.

4.4. Areal rainfall risk

As a way of illustrating the areal rainfall risk in the region at different scales, we show in Fig. III.8 the maximum likelihood estimate of the 12-year return level. This return period is chosen for illustrating extrapolation -which is the main goal of fitting a model rather than estimating empirical return levels-, but considering short extrapolation rather than, e.g., the 100-year return level that would be very uncertain given that only 8 years of data are available. Return levels are shown at two relevant scales in hydrology : the scale (3 h, 100 km^2) intends to identify localized and short-lasting storms likely to induce a fast response of small catchments, while the scale (24 h, 900 km^2) intends to identify more widespread and long-lasting storms likely to induce a slower response of larger catchments These scales are used for illustration but since the Gumbel IDAF-model is defined for the continuum of durations and areas, any other scales could just as well be considered, using Eq. (III.13).

Fig. III.8 shows a remarkable change in the spatial distribution of the 12-year return as the spatio-temporal scales increase. Focusing on the 3 h and 100 km^2 scale, the pattern is quite similar to that of σ_0 in Fig. III.5. The largest 12-year return levels (> 40 mm/h/km^2) are found in the northern part of the crest around the Serre Croix de Bauzon, but also along the foothills "alley" and over Nîmes and Berg Mountains. However, once again we touch here the limits of the present study. Whereas a separate sensitivity analysis shows a remarkable stability of returns levels in the whole Massif Central part, sampling fluctuations are quite large in the foothills. Return levels vary notably along the crest at very short distances. They are divided by three in 10 km distance between the Serre Croix de

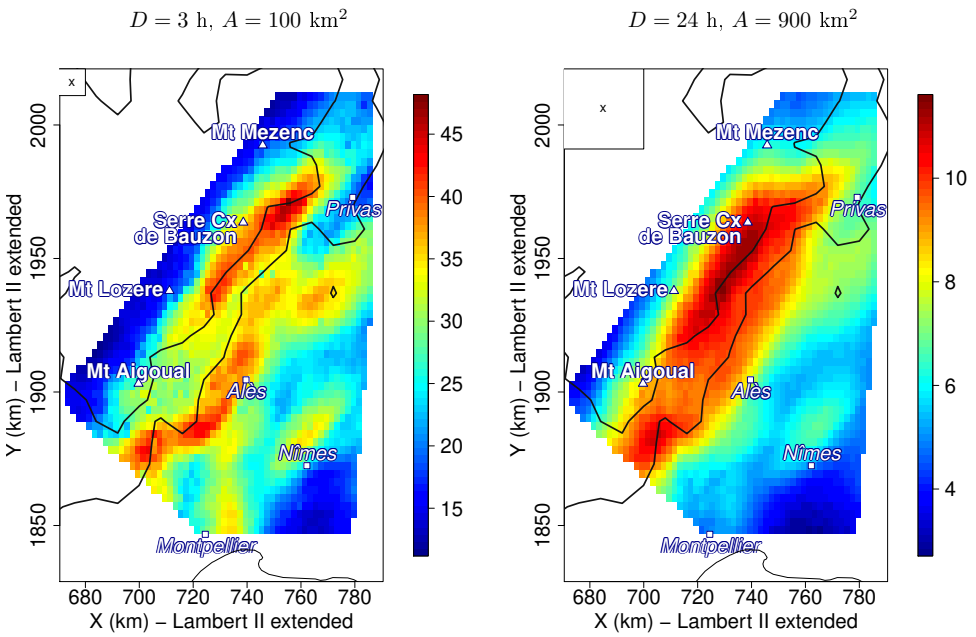

FIGURE III.8 – Maximum likelihood estimates of the 12-year return level (mm/h/km^2) for $D = 3$ h, $A = 100$ km^2 and $D = 24$ h, $A = 900$ km^2. The top-left squares in the maps show the considered spatial scales. The topography is represented by the 400 and 800 m.a.s.l isocontours.

Bauzon and the plateau. Worth noticing also is the fact that return levels in the southern part of the crest are 50% smaller than in the northern part. This largest concentration of rainfall over short duration and small areas in the northern part of the crest might be explained by the deflection of the storm alley that is blocked by the Chaîne du Coiron mentioned before.

At 24 h and 900 km^2 scale, the largest return levels strikingly concentrate over the whole crest and slope, where the two types of convection can contribute to the areal extremes. As said before, both types of organized convection are primary driven by the topography. This is coherent with the results of co-occurrence of extremes at daily scale found in Blanchet and Creutin (2017). Comparison of the two maps of Fig. III.8 nicely shows that storm risk evaluation must be evaluated over the continuum of areas and durations, as provided by the proposed model, since the risk pattern strongly depends on the spatio-temporal scales.

5. Conclusions

In this article, we conducted a regional study of IDAF relationships in a space-time invariant framework. Exploiting the spatio-temporal properties of the rainfall fields, we proposed a new IDAF model that can be seen as a compromise between the physically-based model of De Michele et al. (2001) and a purely empirical data-driven model, such as the framework proposed in Overeem et al. (2010). The generic IDAF model was combined with a Gumbel extreme value distribution, leading to an extreme value IDAF model. This model was applied to annual maxima of areal rainfall in southern France. The extreme value IDAF model was estimated at each 1 km^2 grid point of the region using 8 years of raingage-radar reanalysis data. From an hydrometeorological perspective, the estimated models allowed (i) the analysis of the relationships between space-time statistical properties of annual rainfall extremes and the dynamics of their generating storms, and (ii) the evaluation of the risk of

extreme rainfall accumulations in time and space across the region. In comparison with previous studies conducted using raingage data, the space-time resolution of radar reanalysis data brought a new level of detail in relation with the topography and its signature on extreme rainfall accumulations. We realized that the broad dichotomy identified from a quite dense network of raingages between the low intermittent moderate rainfall of the crests and the high intermittent heavy rainfall of the foothills (see for instance Molinié et al., 2012; Blanchet et al., 2016a; Mélèse et al., 2018), if true and interesting in first approximation, merits further attention given the more detailed organization of extremes in both subregions.

Despite a significant progress brought in the area of IDAF estimation in terms of generality and adaptability, this article relies on a quite strong assumption of statistical scaling of annual maxima, according to which knowing the CDF of annual maxima at a duration and area of reference is enough to know the CDF at any other spatio-temporal scale. Although this assumption has been validated on our data, it would be interesting to assess its impact on IDAF relationships compared to a fully unconstrained model such as that of Overeem et al. (2010). Comparison with common engineering tools involving empirical IDAF relationships would also allow us to quantify the added-value of the model from a practical point of view. From a more mathematical perspective, future work should tackle different issues that have not been addressed in this article. First, this paper provided ARF estimates all across the region without assessing their uncertainty. Uncertainty estimation based on the asymptotic normality of the maximum likelihood estimator or using bootstrap resampling should be easy to implement. Nevertheless our preference would go to the Bayesian framework developed in Mélèse et al. (2018) for IDF modelling. The major issue is however that the ARF model is non-identifiable for $R > 1$, which complicates its estimation in a Bayesian framework. Second, a light-tailed (Gumbel) distribution was used in this paper to model the CDF of annual maxima at different scales. The more general GEV distribution could not be used due to its lack of robustness for short records. However Blanchet et al. (2016a) and Mélèse et al. (2018) show that point rainfall extremes in the region tend to feature bounded distributions over the crest and heavy-tailed distributions in the foothills. Although these results will have to be validated for areal extremes, using the Gumbel distribution is likely to misjudge the risk, by either underestimating (in the foothills) or overestimating (over the crest) the return period of the largest extreme rainfall amounts. A future direction of research will be to make the GEV parameter estimation more robust, by using the annual maxima recorded at the focus pixel and its neighborhood (e.g. at the 8 nearest-pixels) to increase the data sample. This is the "region-of-influence" approach used for point daily rainfall extremes in the region in Carreau et al. (2013) and Evin et al. (2016). The method still has to be developed in the case of space-time extremes. Another possibility will be to take advantage of point data from ground stations, which go back to the 50's in the region, in order to maximize the available historical information. However using station data together with the reanalysis data induces two main issues : i) the use of two databases with probably different measurement bias since raingage data and reanalysis data are different products ; ii) the fact that considering station data beyond the 2008-2015 period of this study may introduce temporal nonstationarity. Blanchet et al. (2016a) and Ribes et al. (2018) have shown that extreme rainfall has increased significantly in most of the region these last decades. Here nonstationarity could be omitted due to the shortness of the period. Finally, a third improvement of this study will be to consider more physically-based surfaces of integration. In this article, squared surfaces have been

chosen for simplicity rather than for physical reasons. Following Blanchet and Creutin (2017), a first improvement will be to consider elliptical surfaces corresponding to maximum volumes, for every pixel, duration, area and time step, as in Kim et al. (2019) in a storm centered approach. Another improvement will be to consider rainfall aggregation over areas matching watersheds instead of using squared areas in order to better address hydrological risk.

6. Appendix

6.1. Details leading to Eq. (III.4)

Eq. (III.1) is valid for all λ. Evaluated at $\lambda = \frac{D_0}{D}$, it leads to :

$$\mathrm{pr}\left\{\left(\frac{D}{D_0}\right)^H M(D,A) < x\right\} = \mathrm{pr}\left\{M(D_0, \left(\frac{D}{D_0}\right)^{-b} A) < x\right\}. \tag{III.21}$$

Developing the right hand side of Eq. (III.21) using (III.2) and writing $k_{D_0}(D,A,A_\star) = K_{D_0}\left(\left(\frac{D}{D_0}\right)^{-b} A, A_\star\right)$ leads to :

$$\mathrm{pr}\left\{\left(\frac{D}{D_0}\right)^H M(D,A) < x\right\} = \mathrm{pr}\left\{k_{D_0}(D,A,A_\star) M\left(D_0,A_\star\right) < x\right\}, \tag{III.22}$$

valid for all D, A, $A_\star$, given D_0. Under Eq. (III.3), we have

$$k_{D_0}(D,A,A_\star) = \left(\frac{1+\sum_{i=1}^R \eta_i \left(\frac{D}{D_0}\right)^{-b\alpha_i} A^{\alpha_i}}{1+\sum_{i=1}^R \eta_i A_\star^{\alpha_i}}\right)^\gamma. \tag{III.23}$$

The change of variable $\eta_i D_0^{b\alpha_i} \mapsto \omega_i$, $i \in \{1,...,R\}$, gives

$$k_{D_0}(D,A,A_\star) = \left(\frac{1+\sum_{i=1}^R \omega_i (D^{-b}A)^{\alpha_i}}{1+\sum_{i=1}^R \omega_i (D_0^{-b}A_\star)^{\alpha_i}}\right)^\gamma. \tag{III.24}$$

Eqs. (III.22) and (III.24) lead to :

$$\mathrm{pr}\left\{\left(\frac{D}{D_0}\right)^H M(D,A) < x\right\} = \mathrm{pr}\left\{\left(\frac{1+\sum_{i=1}^R \omega_i (D^{-b}A)^{\alpha_i}}{1+\sum_{i=1}^R \omega_i (D_0^{-b}A_\star)^{\alpha_i}}\right)^\gamma M\left(D_0,A_\star\right) < x\right\}, \tag{III.25}$$

for any D, A, $A_\star$, given D_0.

6.2. Details leading to Eq. (III.7)

Eq. (III.22) is valid for all areas A. Written for $A = A_\star$, it leads to :

$$\mathrm{pr}\left\{\left(\frac{D}{D_0}\right)^H M(D,A_\star) < x\right\} = \mathrm{pr}\left\{k_{D_0}(D,A_\star,A_\star) M\left(D_0,A_\star\right) < x\right\}. \tag{III.26}$$

Combining Eqs. (III.26) and (III.22) leads to :

$$\mathrm{pr}\left\{M(D,A) < x\right\} = \mathrm{pr}\left\{\frac{k_{D_0}(D,A,A_\star)}{k_{D_0}(D,A_\star,A_\star)} M\left(D,A_\star\right) < x\right\}. \tag{III.27}$$

Thus from Eqs. (III.24) and (III.27)

$$ARF_{D_0}(D,A,A_\star) = \frac{k_{D_0}(D,A,A_\star)}{k_{D_0}(D,A_\star,A_\star)} = \left(\frac{1+\sum_{i=1}^{R}\omega_i(D^{-b}A)^{\alpha_i}}{1+\sum_{i=1}^{R}\omega_i(D^{-b}A_\star)^{\alpha_i}}\right)^{\gamma}, \tag{III.28}$$

for any D, A, $A_\star$, given D_0.

Chapitre *IV*

A Bayesian framework for multi-scale assessment of storm severity and related uncertainties

---

A Bayesian framework for multi-scale assessment of storm severity and related uncertainties

Juliette Blanchet[1], Victor Mélèse[1]

[1]*UGA - IGE CS 40700 38 058 Grenoble Cedex 9, France*

Article soumis dans *Journal of Hydrometeorology*.

Abstract

This article proposes a statistical framework for assessing the multi-scale severity of a given storm at a given location. By severity we refer to the rareness of the storm event, as measured by the return period. Rather than focusing on predetermined spatio-temporal scales, we build a model assessing the return period of a storm event observed across the continuum of durations and areas around a focus location. We develop a Bayesian Intensity-Duration-Area-Frequency model based on extreme value distribution and space-time scale invariance hypotheses. The model allows to derive an analytical expression of the return period for any duration and area, while the Bayesian framework allows by construction to assess the related uncertainties. We apply this framework to high-resolution radar-raingauge reanalysis data covering a mountainous region of southern France during the autumns 2008-2015 and comprising 50 rain events. We estimate the model at two grid points located a few kilometers apart on either side of the mountain crest, considering spatio-temporal scales ranging 3-48 h and 1-2025 km^2. We show that at all scales and for all significant events, the return period uncertainties are skewed to the right, evidencing the need of considering uncertainty to avoid systematic risk underestimation. We also reveal the large variability of the storm severity both at short distance and across scales, due to both the natural variability of rainfall and the mask effect induced by the mountain crest.

1. Introduction

Mediterranean storms triggering floods have long been a source of heavy damage caused to people and infrastructure. What is the frequency of occurrence -or equivalently the return period- of such devastating storms ? Rain falling non uniformly in space and time, the return period of a given storm depends on both the location, the duration and the area over which it is observed. This article deals with these three sources of variability of the return period.

Extremes being rare by definition, the computation of extraordinary return periods -which are of most interest- faces a problem of lack of data. Different statistical methods have been proposed to strengthen the robustness of return period estimates based on short time series. Among them, the Regional Frequency Analysis (RFA) is based on the identification of homogeneous subregions in terms of rainfall distribution, allowing to pool together extreme rainfall data of a given subregion, and thus to base return level estimation on longer series. Norbiato et al. (2007) used RFA to compute the return period of point rainfall during a storm that occurred in August 2003 in the eastern Italian Alps. The authors illustrated in particular that the rareness of point rainfall (i.e. the return period) depends on the considered accumulation duration, due to rainfall temporal intermittency. Liu et al. (2015) also used RFA to study a storm that occurred in February 2007 in Jakarta, Indonesia. They highlighted in particular the strong spatial variability of point rainfall rareness induced by the spatial intermittency.

Another way to strengthen the robustness of return period estimates is to account for the structural properties of rainfields, in order to base estimation on a pool of extreme rainfall depths observed at different scales. Several articles applied this idea for point rainfall considered at different durations.

Temporal scaling properties of rainfall were used to derive analytical expressions of Intensity-Duration-Frequency (IDF) curves representing by mathematical equations the relationships between rainfall intensity, duration and return period of an event in, e.g., Bougadis and Adamowski (2006); Van de Vyver and Demarée (2010) and Mélèse et al. (2018). The studies accounting for both the temporal and spatial scale -i.e. dealing with extreme values of areal rainfall considered over different durations and areas- are much more scarce, partly due to the lack of spatial rainfall measurements. One of these is the study of De Michele et al. (2001), which used the space-time structural properties of the rain fields to build analytical expressions of Intensity-Duration-Area-Frequency (IDAF) relationships in the Reno basin, Italy. Mélèse et al. (2019) proposed for the region studied in this article a new IDAF model that can be seen as a compromise between the structure-based model of De Michele et al. (2001) and a purely empirical data-driven model, such as the framework proposed in Overeem et al. (2010). Additionally to strengthening the return levels estimates, the IDAF relationships allow to compute the return period of an event for any duration and any area in the applicable range of scales. Thus they allow to assess the multi-scale rareness of a given storm at a given location. Following Ramos et al. (2005), we refer to the rareness of a storm observed over a continuum of spatio-temporal scales as the storm "severity" (or multi-scale severity). Ramos et al. (2005) considered the storm severity in a regional way, by focusing on the return level of the maximum rainfall value over a given region. They used the IDAF relationships to study the severity of three storms that occurred in a region of 300 km^2 area, around the city of Marseilles, in southeastern France. They revealed in particular that areal return period estimates can vary from ordinary values (1-2 years) to exceptional values (100 years) depending on the considered durations and areas. Also, for a given duration, both ordinary and exceptional point return period estimates can coexist a few kilometers apart due to spatial intermittency. Ceresetti et al. (2012) extended the work of Ramos et al. (2005) to a $3,000$ km^2 region located in southern France, using the IDAF model developed in De Michele et al. (2001). By considering the storm severity in a regional way, neither Ramos et al. (2005) nor Ceresetti et al. (2012) could assess the spatial variability of the severity across scales.

Another issue when dealing with return period estimation is that uncertainty is unavoidable both because models are imperfect and because data have a limited length. Uncertainty is particularly large for the largest return periods, which in turn are usually of most interest. Evaluating uncertainty is required to avoid a systematic underestimation of the probability of occurrence of disastrous events (Coles and Pericchi, 2003). To the best of our knowledge, the only study providing uncertainty estimates of IDAF relationships is Overeem et al. (2010), where uncertainty is estimated using bootstrap resampling. However the Bayesian framework is more suitable because it inherently allows to model uncertainty and to incorporate *a priori* knowledge on the model parameters, as illustrated in Mélèse et al. (2018) for IDF relationships.

In this article, we construct a statistical model allowing to assess the severity of a storm at a given location and the related uncertainties. We consider the IDAF model of De Michele et al. (2001) combined with a Gumbel distribution, in the Bayesian framework. We estimate this model at two grid points of a high-resolution reanalysis database covering a mountainous region of southern France. The two considered locations lie a few kilometers apart -one lying over the mountain crest while the other lies in the mountain plateau. This proximity allows us to study the spatial variability of the severity at short distance on either side of the crest.

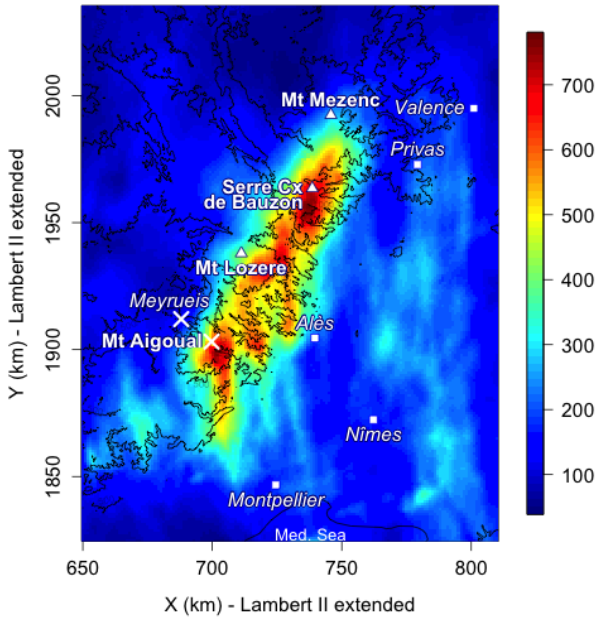

FIGURE IV.1 – Accumulated rainfall depth (mm/km^2) from 2011/11/01 at 06 UTC to 2011/11/06 at 00 UTC in the study region. The two white crosses indicate the localisation of the two considered pixels, Meyrueis and Mont Aigoual. The white triangles show the main peaks of the Massif Central crest and the white squares show the main towns.

The data are presented in Section 2. The Bayesian framework of extreme value IDAF relationships allowing to assess the storm severity and the related uncertainties is developed in Section 3. Results are presented in Section 4, with a particular focus on the severity of the November 2011 event at the two locations.

2. Data

The region of study is centered on the Massif Central range, a mountainous area of southern France that is under Mediterranean climatic influence. We focus our analysis on two locations : one is located at the Mont Aigoual peak (1565 m.a.s.l), in the southern part of the Massif Central crest. The other one lies in the Massif Central plateau, near the city of Meyrueis (800 m.a.s.l), 15 km North-West of Mont Aigoual (see the vwhite crosses in Fig. IV.1). Although close in distance, these two locations feature contrasted hydrometeorology. The Massif Central crest delineates a topographical barrier protecting the Massif Central plateau from Mediterranean moist winds bringing extreme rainfall, giving usually much larger rainfall amounts over the crest than in the plateau (Mélèse et al., 2018, 2019; Blanchet et al., 2016a; Ceresetti et al., 2010).

We use high-resolution rainfall reanalysis data based on radar-raingauge merging, as described in Boudevillain et al. (2016). These reanalyses are available at 1 km^2 spatial resolution and at 1 h temporal resolution for 50 significant rain events for the autumns 2008-2015. The duration of these events varies between a few hours to more than 8 successive days. By studying extremes based on only eight years of data, we are aware that interpretation of the results appeals for vigilance. In particular,

the large return period estimations (say larger than 20 years) need to be considered with prudence due to the large extrapolation they induce. However the contribution of this article is primary a "proof of concept" of a statistical framework allowing to estimate the multi-scale severity of a storm and the related uncertainties. Although we use the best high-resolution spatio-temporal data available in our region, more reliable results would obviously benefit from longer time series.

Considering the 46 durations $3, 4, \ldots, 48$ h and the v23 areas $1, 3^2, \ldots, 45^2$ km^2, we compute the time series of areal rainfall centered on each of the two pixels, for each pair of duration and area, considering squared surfaces centered on the focus pixels for the areal aggregation. Then two databases are constructed for each pixel. DB1 contains the annual maximum intensities for each pair of duration and area. This database will be used for the estimation of the IDAF model (Section 3). For computational reasons and owing to the fact that very dependent scales bring almost the same information, we restrict this database to 9 durations (3, 4, 6, 8, 12, 16, 24, 36 and 48 h) and 10 areas (1, 9, 25, 81, 169, 361, 625, 1089, 1521, 2025 km^2), giving for each pixel and each year a vector of 90 annual maxima. DB2 contains the event maximum intensities for all spatio-temporal scales (without restriction), giving for each pixel and each event a vector of v1058 event maxima. This second database will be used to compute the multi-scale severity of the 50 rain events, based on the estimated IDAF model (Section 4). A particular focus will be made on the event that occurred from the first to the sixth of November 2011, which resulted in the largest rainfall accumulation over the Massif Central crest during the observation period.

3. A framework of multi-scale severity modeling

The model of IDAF relationships considered in this article has been developed in De Michele et al. (2001) in a frequentist framework and used in Panthou et al. (2014). It is a particular case of the model developed in Mélèse et al. (2019) for the study region, using the same data. However a Bayesian version is considered here, in which the IDAF parameters are considered as random variables rather than scalars. The proposed model is also an extension of the Bayesian IDF model proposed in Mélèse et al. (2018) when adding the space component. For the sake of clarity, in the following, we write random variables with bold symbols to distinguish them from scalars. We first present the model in the frequentist framework, as in Mélèse et al. (2019), and then we develop the Bayesian case and its inference.

3.1. Extreme value IDAF relationships : frequentist framework

The considered model applies to the annual maxima of DB1. It relies on two assumptions. The first one follows extreme value theory (Coles et al., 2001). It is used to model the cumulative distribution function (CDF) of annual maximum intensity for some reference area A_0 and some reference duration D_0, taken in this article equal to the finest scales of the database, $A_0 = 1$ km^2 and $D_0 = 3$ h. The founding theorem of extreme value theory states that if independent and identically distributed data are blocked into sequences of observation and if each block is long enough, then the CDF of block maxima is approximately the Generalized Extreme Value (GEV) distribution. The Gumbel distribution is a particular case of the GEV distribution in which the so-called shape parameter is

fixed to 0. Although less flexible in general, Mélèse et al. (2019) showed that the Gumbel distribution is preferable for our data owing to the difficulty in estimating the GEV shape parameter based on short records (here 8 years). Thus we suppose that the random variable of annual maximum intensity for the duration and area of reference, $\boldsymbol{M}(D_0, A_0)$, follows a Gumbel distribution i.e. that :

$$\mathrm{pr}\left\{\boldsymbol{M}(D_0, A_0) < x\right\} = \exp\left[-\exp\left(-\frac{x-\mu_0}{\sigma_0}\right)\right], \tag{IV.1}$$

where $\boldsymbol{\mu}_0$ is a scalar representing the location parameter of the Gumbel distribution and $\boldsymbol{\sigma}_0$ is the non negative scalar representing the scale parameter of the Gumbel distribution. The second hypothesis relies on space-time structural properties of the rain fields. Assuming space-time scaling relationships, Mélèse et al. (2019) derived the CDF of annual maximum rainfall intensity for any pair of duration and area, $\boldsymbol{M}(D, A)$, from the CDF of annual maximum rainfall intensity for the duration and area of reference, $\boldsymbol{M}(D_0, A_0)$, as :

$$\mathrm{pr}\left\{\boldsymbol{M}(D, A) < x\right\} = \mathrm{pr}\left\{\left(\frac{D}{D_0}\right)^{-H}\left(\frac{1+\omega D^{-\beta}A^{\alpha}}{1+\omega D_0^{-\beta}A_0^{\alpha}}\right)^{\gamma}\boldsymbol{M}\left(D_0, A_0\right) < x\right\}, \tag{IV.2}$$

where H is a non negative scalar representing the temporal scaling exponent, and ω, β, α and γ are scalars modeling the spatio-temporal scaling. Note that Eq. (IV.2) is exactly the model of De Michele et al. (2001) (up to a change of notation) but it is written here for any A_0, whereas De Michele et al. (2001) considered $A_0 \approx 0$ km^2 corresponding to the surface of a rain gauge. However Mélèse et al. (2019) showed that Eq. (IV.2) is overparametrized for our data since there is no loss of generality in considering $\gamma = 1$ due to compensation effects between ω, β, α and γ. The authors also showed that a more flexible model is to replace the term $\omega D^{-\beta}$ in Eq. (IV.2) by $\omega D^{-\beta} + \omega_2 D^{-\beta_2}$ in order to model that different scaling relationships may govern areal rainfall depending on the duration. However the additional term $\omega_2 D^{-\beta_2}$ reveals to be unnecessary for the two pixels of this study.

Combining Eqs. (IV.1) and (IV.2) with $\gamma = 1$ implies that the random variable of annual maximum rainfall intensity for any duration D and any area A follows a Gumbel distribution, i.e. that :

$$\mathrm{pr}\left\{\boldsymbol{M}(D, A) < x\right\} = \exp\left[-\exp\left(-\left(\frac{D}{D_0}\right)^{H}\left(\frac{1+\omega D^{-\beta}A^{\alpha}}{1+\omega D_0^{-\beta}A_0^{\alpha}}\right)^{-1}\frac{x}{\sigma_0} + \frac{\mu_0}{\sigma_0}\right)\right], \tag{IV.3}$$

where $\theta = (\mu_0, \sigma_0, H, \omega, \beta, \alpha)$ is the set of model parameters.

Let consider an event maximum i in DB2 associated with a duration D and an area A. Its return period is obtained from Eq. (IV.3) combined with the expression of Stedinger et al. (1993) linking the return period of large values to the return period of annual maxima, giving :

$$T_{D,A,i} = \left\{\exp\left(-\left(\frac{D}{D_0}\right)^{H}\left(\frac{1+\boldsymbol{\omega} D^{-\beta}A^{\alpha}}{1+\omega D_0^{-\beta}A_0^{\alpha}}\right)^{-1}\frac{i}{\sigma_0} + \frac{\mu_0}{\sigma_0}\right)\right\}^{-1}. \tag{IV.4}$$

$T_{D,A,i}$ can be interpreted has the mean number of years between two consecutive rainfall intensities at scales (D, A) that exceed the intensity i. Following Ramos et al. (2005), we define the multi-scale severity of a given event as the set of return periods associated with all event maxima, when

considering the continuum of durations and areas. Note that a slightly different definition is considered in Cattiaux and Ribes (2018), where the minimum probability of exceedance is considered rather than the return period of the event maximum.

3.2. Extreme value IDAF relationships : Bayesian framework

The Bayesian framework differs from the frequentist framework in that the model parameters are considered as random variables rather than as scalars. As will be seen in Section 3.3.3, Bayesian inference gives a direct and flexible estimation of uncertainty through probability density functions. Mélèse et al. (2018) illustrated this flexibility with respect to the frequentist case for IDF relationships. The above Eqs. (IV.1) to (IV.3) still hold in the Bayesian case but the probabilities in the left-hand sides are conditional to the random variable of model parameters, $\boldsymbol{\theta}$, being equal to some value $\theta = (\mu_0, \sigma_0, H, \omega, \beta, \alpha)$. The return period is also given by Eq. IV.4 but the equality applies to random variables.

3.3. Bayesian inference

For the sake of conciseness, we write $\underline{m}$ the set of annual maximum rainfall intensities for all durations and all areas, i.e. $\underline{m} = \{m_{D,A,y}; D \in \mathcal{D}, A \in \mathcal{A}, y \in \mathcal{Y}\}$ where $\mathcal{D}$ is the set of durations, $\mathcal{A}$ is the set of areas and $\mathcal{Y}$ is the set of years. In the Bayesian framework, inference requires estimating the density of the parameters knowing the data i.e. $f(\theta|\underline{m})$, called the posterior density. The Bayes formula states that :

$$f(\theta|\underline{m}) = \frac{f(\underline{m}|\theta) f_\theta(\theta)}{\int_\theta f(\underline{m}|\theta) f_\theta(\theta) d\theta}, \tag{IV.5}$$

where $f(\underline{m}|\theta)$ is the likelihood function and f_θ is the density of $\boldsymbol{\theta}$ called the prior density. We suppose independence of the model parameters, i.e. that

$$f_\theta(\theta) = f_{\mu_0}(\mu_0) f_{\sigma_0}(\sigma_0) f_H(H) f_\omega(\omega) f_\beta(\beta) f_\alpha(\alpha), \tag{IV.6}$$

where f denote univariate densities. In this study, the six chosen prior densities are weakly informative, using uniform densities for $\boldsymbol{\mu}_0$, $\boldsymbol{\sigma}_0$ and $\boldsymbol{H}$ and Gaussian densities for $\boldsymbol{\omega}$, $\boldsymbol{\beta}$, $\boldsymbol{\alpha}$ (see details in Appendix B.6.2.1). Under the assumptions that : i) annual maxima are independent from one year to another and ii) annual maxima of a given year at different durations and areas are independent, the expression of the likelihood function $f(\underline{m}|\theta)$ is given by :

$$f_{ind}(\underline{m}|\theta) = \prod_{y \in \mathcal{Y}} \prod_{A \in \mathcal{A}} \prod_{D \in \mathcal{D}} f_{D,A}(m_{D,A,y}|\theta), \tag{IV.7}$$

where $f_{D,A}$ is the Gumbel density associated with Eq. (IV.3). However the assumption ii) above is likely to be misspecified. As a consequence, the likelihood f_{ind} is likely not to be the true probability of the observed data, and the posterior density (IV.5) under (IV.7) can be misleading. Adjustments of composite likelihoods such as the independence likelihood f_{ind} in a Bayesian framework have been proposed in Ribatet et al. (2012) and Pauli et al. (2011), in order to retrieve some of the desirable properties of the full likelihood. They are used in Van de Vyver (2015) for IDF relationships. Here we consider the so-called magnitude adjustment, which replaces the independence likelihood f_{ind} by

the adjusted likelihood :

$$f_{adj}(\underline{m}|\theta) = \{f_{ind}(\underline{m}|\theta)\}^{k(\hat{\theta}_{ind})}, \tag{IV.8}$$

where $k(\hat{\theta}_{ind})$ is given in Appendix A. Plugging (IV.8) in (IV.5) gives the adjusted posterior density

$$f_{adj}(\theta|\underline{m}) = \frac{f_{adj}(\underline{m}|\theta) f_\theta(\theta)}{\int_\theta f_{adj}(\underline{m}|\theta) f_\theta(\theta) d\theta}. \tag{IV.9}$$

Markov Chain Monte Carlo (MCMC) techniques provide a way of simulating from complex distribution, such as the posterior density $f_{adj}(\theta|\underline{m})$, by simulating Markov chains which have the target distributions as their stationary distributions. The posterior density can be obtained from the simulated samples at convergence of the Markov chains. In this article, we use the DRAM algorithm developed in Haario et al. (2006). It combines an Adaptive Metropolis (AM) sampler and Delayed Rejection (DR), improving the efficiency of the Metropolis-Hasting algorithm (see details in Appendix B.6.2.2).

Given the MCMC samples, samples of the posterior density $f(\boldsymbol{T}_{D,A,i}|\underline{m})$ are obtained by applying Eq. (IV.4) to the samples of $\boldsymbol{\mu}_0, \boldsymbol{\sigma}_0, \boldsymbol{H}, \boldsymbol{\omega}, \boldsymbol{\beta}, \boldsymbol{\alpha}$. This gives an estimate of the return period posterior density $f(\boldsymbol{T}_{D,A,i}|\underline{m})$. When needed, summary of the latter will be obtained by considering the mode of the posterior distribution -which is interpreted as the most likely mean number of years between two consecutive exceedances of the level i-, together with the 2.5%- and 97.5%-quantiles, respectively noted $\hat{T}^{mode}_{D,A,i}$, $\hat{T}^{low}_{D,A,i}$ and $\hat{T}^{up}_{D,A,i}$. Likewise, summary of the multi-scale severity of an event will be given by the set of $(T^{mode}_{D,A,i}, \hat{T}^{low}_{D,A,i}, \hat{T}^{up}_{D,A,i})$ when D and A range the continuum of scales.

4. Results

4.1. MCMC monitoring

The IDAF model developed in Section 3 is estimated at the two considered locations based on the annual maxima of DB1. For each pixel, we run the DRAM algorithm four times, giving four MCMC chains whose convergence is monitored using the $\hat{R}$ convergence criteria of Gelman et al. (2014), chapter 6. We consider that convergence is reached for $\hat{R} < 1.05$, which is obtained after $200,000$ iterations. The burn-in period is set to the first half of iterations. Every 100th iteration of the remaining $100,000$ iterations of the four MCMC chains is considered for estimating the posterior densities in order to reduce the dependence within the sample. The posterior density estimates are obtained from these $4,000$ iterations.

4.2. Model validation

We assess goodness-of-fit of the Bayesian Gumbel-IDAF model but comparing the empirical and modeled quantiles. The empirical quantiles at a given scale (D, A) are the sorted annual maxima. Let $m_{D,A,(j)}$ be the j-th largest maxima in the annual maxima series for duration D and area A at a given pixel, for $j = 1, \ldots, 8$. This quantile is associated with a non-exceedance probability p_j. Different

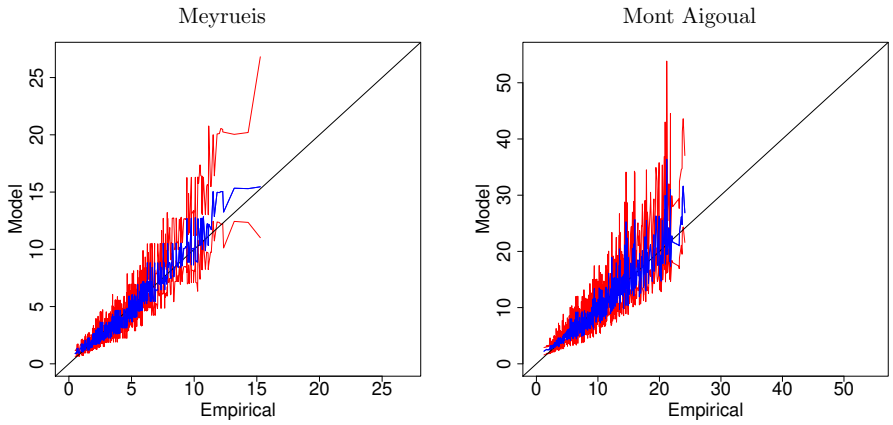

FIGURE IV.2 – QQ plot for Meyrueis and Mont Aigoual for all spatio-temporal scales (D, A). The blue line shows the posterior modes of the quantile densities. The red lines show the 95% credibility intervals. Unit is mm/h/km^2.

definitions are possible for p_j ; here we take the probability returned by the function 'ppoints' of the R language (R Core Team, 2019). The estimated quantile associated with this probability is obtained by inverting $\text{pr}\{\boldsymbol{M}(D, A)|\theta\} = p_j$ using Eq. (IV.3). Plugging the MCMC samples of the parameters θ in Eq. (IV.3) gives a sample of posterior quantiles associated with p_j, and hence an estimate of its posterior density. Fig. IV.2 compares the empirical quantiles with the posterior quantiles, for all possible pairs of scales, summarizing the quantile posterior density using the posterior mode together with the 95% credibility interval. It shows a quite satisfying fit, with the posterior modes mainly aligned along the diagonal line corresponding to a perfect adequacy with the observed data. In particular, there is also no systematic over- or underestimation of the quantiles despite the use of a Gumbel rather than a GEV distribution.

4.3. Multi-scale severity of the 2011 event

A particular focus is made on the event of DB2 that gave the largest rainfall accumulation over the Massif Central crest. This event occurred from the first to the sixth of November 2011. Although several deep convective systems were triggered during the 1st, 4th and 5th in the foothills, the great majority of this event corresponds to quasi-continuous orographic rainfall in time and space over the Massif Central crest from the 2nd to the 6th (Boudevillain et al., 2016). Fig. IV.1 displays the map of the accumulated rainfall depth during this event. More than 700 mm/km^2 rainfall were recorded at the South of Serre Croix de Bauzon and Mont Aigoual. This event is a typical case of shallow convection characterized by north-south rain bands triggered by the interaction of moist southern winds and details of the topography (Miniscloux et al., 2001; Anquetin et al., 2003; Godart et al., 2009).

Fig. IV.3 compares the return period posterior density estimates of this event. For illustration purpose, we focus here on two scales that are relevant from a hydrological point of view, considering (3 h, 89 km^2) and (24 h, 1089 km^2) (Marchi et al., 2010). For either pixel, the posterior density varies greatly when passing from one spatio-temporal scale to another, which was obviously expected since rainfall neither accumulates uniformly in time nor in space. For both scales, Mont Aigoual and its neighborhood received twice as much rainfall as Meyrueis, illustrating the mask effect induced

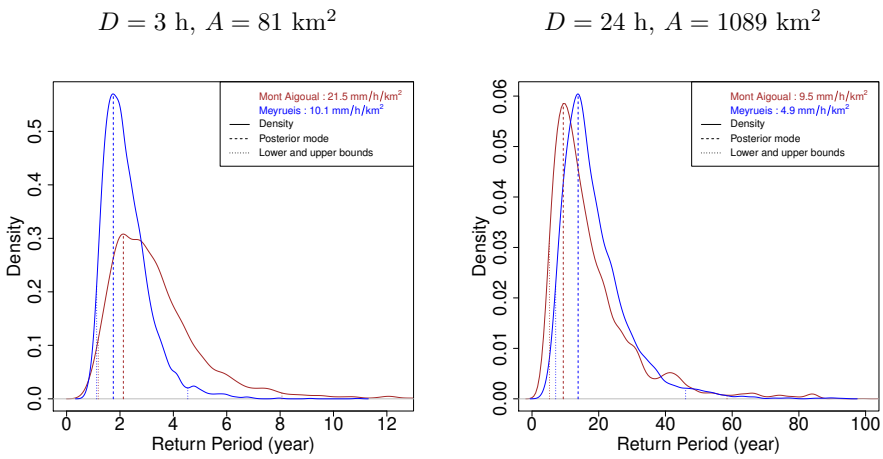

FIGURE IV.3 – Posterior density estimates of the 2011 event return periods in Mont Aigoual and Meyrueis at $D = 3$ h, $A = 81$ km^2 (left) and at $D = 24$ h, $A = 1089$ km^2 (right). The dashed vertical lines show the mode of the posterior density. The dotted vertical lines show the lower and upper bounds of the 95% credibility intervals.

by the crest that protects the Massif Central plateau from the moist southern winds bringing rainfall extremes. Despite this factor 2, the return period posterior densities are quite similar at both locations. The 2011 event featured long lasting orographic rainfalls leading to quite ordinary rainfall intensities for short durations (return periods of a few years) but much more extraordinary accumulations at daily scale (return periods of several tens of years).

Fig. IV.3 also reveals that whatever scale and pixel, the posterior densities are asymmetric with heavier right tails than the left tails, even more in Mont Aigoual than in Meyrueis . To quantify this, we consider the ratio of asymmetry defined as $e = (\hat{T}^{up}_{D,A,i} - \hat{T}^{mode}_{D,A,i})/(\hat{T}^{mode}_{D,A,i} - \hat{T}^{low}_{D,A,i})$. Values of $e = 1$, $e > 1$ and $e < 1$ respectively correspond to symmetric, right-skewed and left-skewed posterior densities. The asymmetry ratio e is more than twice as big in Mont Aigoual than in Meyrueis for both scales of Fig. IV.3, with values from 3 to 11. This implies that, for both scales and both locations, there is actually a much greater likelihood for the true 2011 return periods to be larger than $\hat{T}^{mode}$ rather than lower. Estimating return period as its most likely values $\hat{T}^{mode}$, omitting uncertainties, is likely to lead to an underestimation of the true return period.

As a way of generalizing the previous results for the continuum of scales, we visualize in Fig. IV.4 the multi-scale maxima together with the multi-scale severity of the 2011 event, in the vein of the severity diagrams of Ramos et al. (2005) but considered here at a given location rather than at regional scale. The maximum intensity diagrams of the two locations confirm the mask effect induced by the topography, with decreasing maximum rainfall intensity as the area increases in Mont Aigoual, whereas the contrary applies to Meyrueis.

Keeping in mind the shortness of the database, we comment below the main patterns of the severity diagrams, interpreting the largest return period estimates in a rough way rather than commenting on the exact numbers. Comparing the diagrams of maximum intensity and severity mode shows that the spatio-temporal scales featuring the largest maxima do not correspond to those featuring the largest return periods. In Mont Aigoual, the maximum rainfall intensities produced during the 2011 event were quite ordinary for durations $3-4$ h, with most likely return periods around a few years. On the contrary, they were very exceptional for durations ranging $16-36$ h over areas extending from 10 to

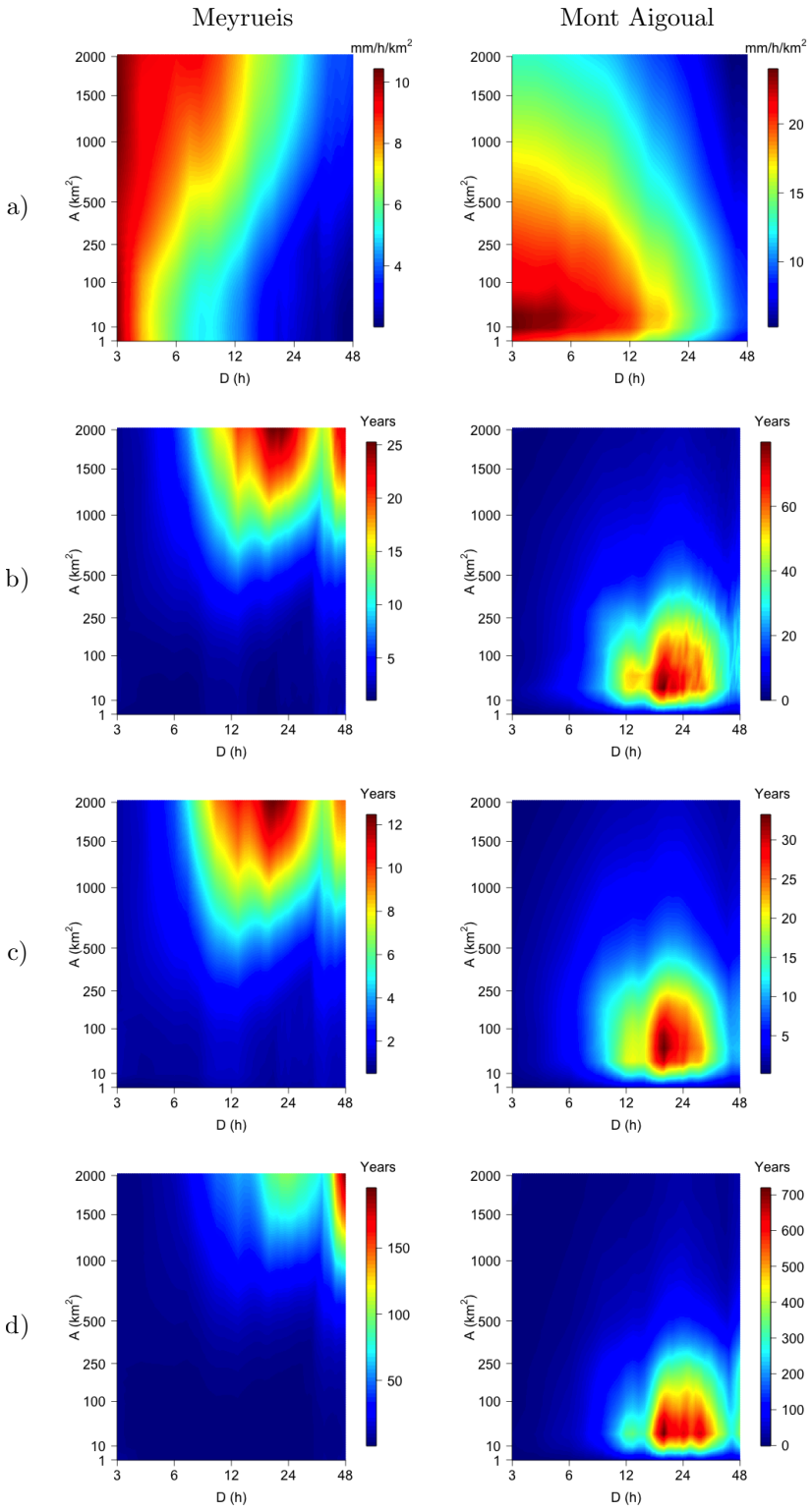

FIGURE IV.4 – Severity of the 2011 event in Meyrueis and Mont Aigoual : a) event maximum, b) posterior mode of the return period densities, c) lower bound of the 95% credibility interval, d) upper bound of the 95% credibility interval. Note that the color scale changes from one plot to another.

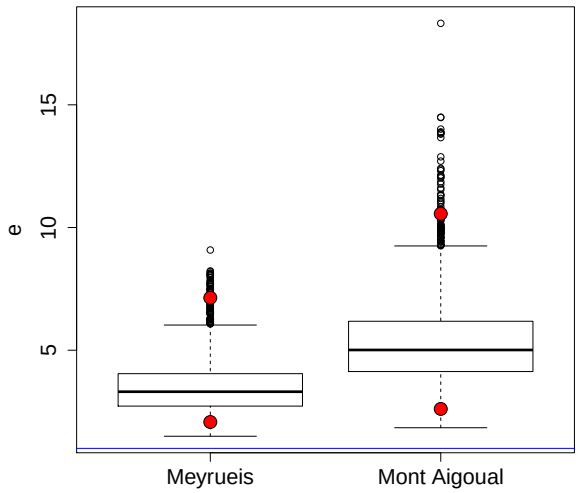

FIGURE IV.5 – Boxplot of the ratio $e = d_{upper}/d_{lower}$ for Mont Aigoual and Meyrueis for all event maxima with $\hat{T}^{mode}_{D,A,i} \geq 2$ years, excluding the 2011 event. The upper and lower red points show the quantiles of order 0.975 and 0.025, respectively. The blue horizontal line at 1 corresponds to symmetric density.

250 km^2, with most likely return periods of several tens of years. This shows that, at a given location, a storm can be both ordinary and exceptional depending on the considered spatio-temporal scales, as also shown in Ramos et al. (2005). The most severe spatio-temporal scales (i.e. corresponding to the largest return periods) for the 2011 event in Meyrueis are 10 h - 30 h and 800 km^2 - 2000 km^2. In Mont Aigoual, similar temporal scales are found (16 h - 30 h) but they are associated with much lower areas (10 km^2 - 250 km^2) due to the topographical effect intensifying rainfall over the crest.

As expected, the patterns of the lower and upper bounds of the credibility intervals are broadly similar to that of the mode since larger return periods tend to come with larger uncertainties. However, a closer look reveals some non linearities. The lower bound of the credibility intervals is located at $25-90\%$ of the mode across all scales in both locations. The upper bound equals $150-850\%$ of the mode for Meyrueis and $300-1500\%$ of the mode for Mont Aigoual, with the most severe scales displaying among the largest values. This reveals a larger uncertainty of the return period on the right side, and particularly for the most severe scales and for Mont Aigoual where the asymmetry ratio is up to 24 (up to 6 in Meyrueis).

4.4. Generalization to other events

The asymmetry of the return period densities showed above for the 2011 event is actually generalizable to all the significant event maxima across all scales. To show this, we consider the event maxima of DB2 whose posterior modes are larger than 2 years, excluding the 2011 event which was already described in the previous section. There are v4072 such cases for Mont Aigoual and v3962 for Meyrueis. Fig. IV.5 shows the asymmetry ratio e for each of these event maxima. There is no left-skewed return period density (i.e. all asymmetry ratios are larger than 1). The 342 event maxima of Mont Aigoual whose mode exceeds 20 years show an average e of 6 (up to 22).

Fig. IV.6 shows the posterior modes of the severity diagrams of the four second-most severe events in Mont Aigoual. The 2010 and 2008 events (a and b) are cases of shallow convection organized in north-south rain bands, as the 2011 event (see Fig. IV.1). The 2015 and 2014 events (c and d) show situations of deep convection during which the circulation of the Mesoscale Convective System (MCS) is modified by the interaction with the topography at different scales. This interaction more or less stabilizes the MCS upstream from the crest, over the foothills (Ducrocq et al., 2008). Considering the pattern of the severity diagrams (i.e. the colors) rather than the absolute values of the return periods, Fig. IV.6 reveals the variety of severity patterns both within a given class of precipitation (vdeep convection or shallow convection) and between the two classes. Although the pattern of the severity diagram of the 2010 event may appear somewhat similar to that of the 2011 event (see Fig. IV.4), it actually shows a case of severe precipitation over much shorter durations. Broadly speaking, in both Meyrueis and Mont Aigoual, the spatio-temporal "dynamics" of the 2010 event (as represented by the return period) was similar to that of the 2011 event but during a much shorter time. The 2008 event, although corresponding to the same class of shallow banded convection, shows a much more different pattern of severity. It was indeed quite ordinary in Mont Aigoual and its neighborhood at sub-daily to daily scale but it was more unusual at all spatial scales for $24-48$ h durations. Rainfall intensities were basically less intense but more spread in time and space around Mont Aigoual than during the 2010 and 2011 events. The two cases of deep convection show also very different severities in both Mont Aigoual and Meyrueis. In Mont Aigoual, the largest severities of the 2015 event are found for quite small areas ($10-300$ km^2) and medium durations ($6-24$ h), roughly like the 2011 event of Fig. IV.4. However a noteworthy difference is that the medium severities (relatively to the largest values) extend down to 3 h and up to 2000 km^2 due to the stabilization of the MCS upstream from the crest. On the contrary, the 2015 event shows almost uniform severities over all spatio-temporal scales. In Meyrueis, the daily scale and large areas feature among the largest severities, which is again the signature of the MCS staibilization upstream from the crest. Although obviously non exhaustive, these examples illustrate that the multi-scale severity diagram is a powerful tool to visualize the "specialness" of a given event at a given location. Neither an accumulation map nor a couple of return periods estimates can provide such a comprehensive description of how "special" an event was across the scales.

5. Conclusion

In this article we assessed the multi-scale severity of a given storm at a given location. A Bayesian framework was proposed to compute the severity and the associated uncertainties at multiple scales. The multi-scale severity of 50 events were computed at two nearby locations of the Massif Central, using a raingauge-radar reanalysis database. Three main results were found. First, the study revealed right-skewed posterior densities of return periods across all scales, and particularly for the largest return periods, evidencing the benefit of considering uncertainty in order to avoid a systematic underestimation of the frequency of occurrence of the severe events. Second, we showed the variability of the storm return period at a given location depending on the spatio-temporal scales, showing the benefit of assessing and visualizing the severity over the continuum of durations and areas rather than at predetermined spatio-temporal scales. Finally, we showed the strong spatial variability of

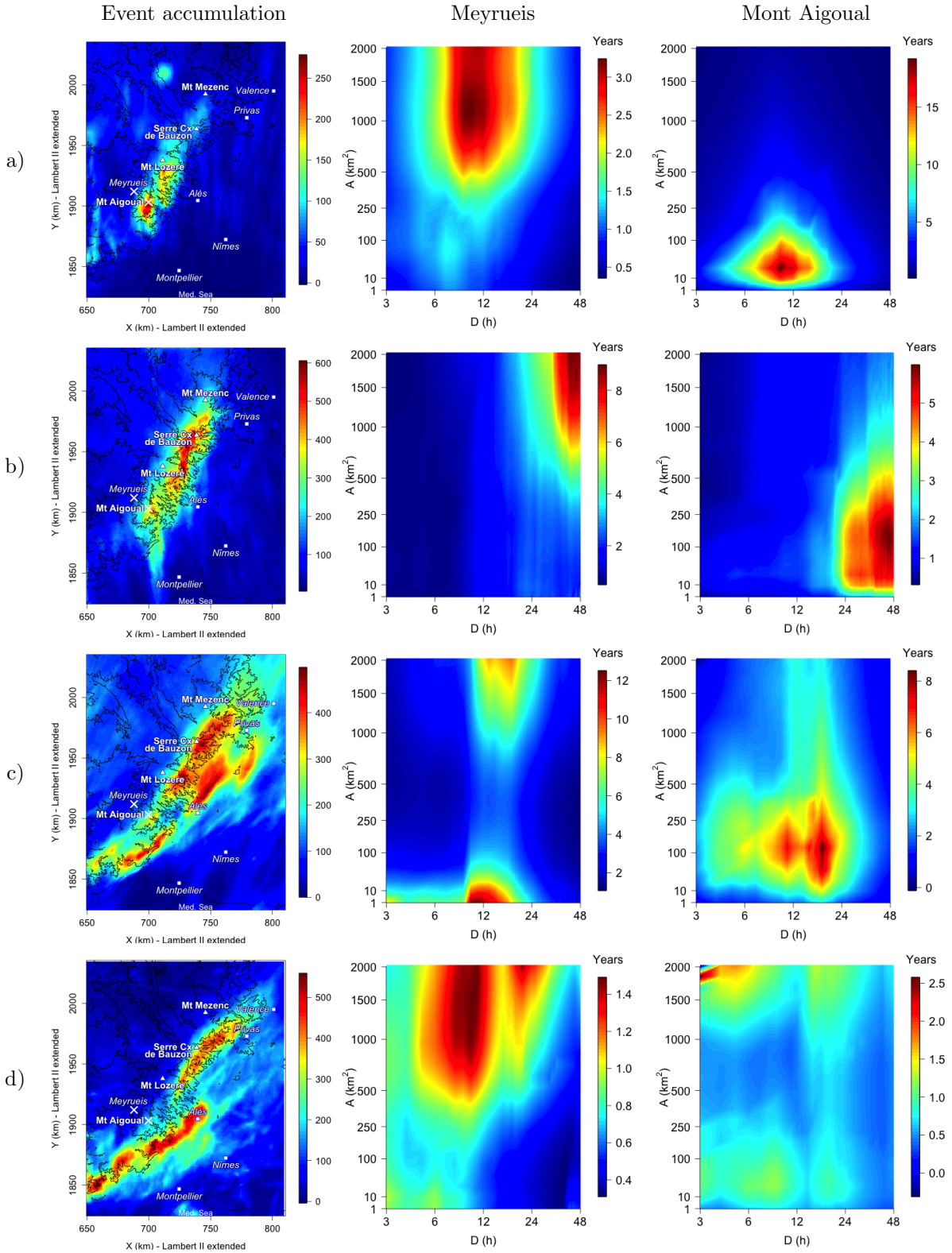

FIGURE IV.6 – Accumulated rainfall depth (mm/km^2) and severity diagrams (posterior modes) of the four second-most severe events in Mont Aigoual : a) from 2010/10/03 06 UTC to 2010/10/05 00 UTC, b) from 2008/10/31 06 UTC to 2008/11/03 06 UTC, c) from 2015/09/11 06 UTC to 2015/09/18 06 UTC, d) from 2014/09/15 at 06 UTC to 2014/09/21 at 00 UTC.

the severity at short distance. This variability is partly due to the inherent rainfall variability but it is exacerbated here by the topography of the region. This result emphasizes the merit of using high-resolution radar data rather than a sparser raingauge network.

Despite a significant progress brought in the area of rainfall severity assessment, a limitation of the present study is that the considered spatial scales of aggregation, which are squared, do not coincide with the hydrological risk, that depends on the shape of watershed over which rainfall accumulates. An improvement of this study will be to consider the severity over areas matching the watersheds. However a difficulty is that the watersheds of interest in the region extend from the Massif Central crest to the foothills. The latter undergoes deep convective systems whose positioning is unpredictable, making their sampling difficult within a short observation period (Mélèse et al., 2019). Methods based on stochastic storm transposition (Foufoula-Georgiou, 1989; Wright et al., 2013; Zhou et al., 2019) reshuffling the reanalysis data to construct longer series of rain fields in the foothills seem an interesting idea to pursue.

6. Appendix

6.1. Adjusted likelihood

In view of retrieving some of the desirable properties of the full likelihood, the magnitude adjustment replaces the independence likelihood

$$f_{ind}(\underline{m}|\theta) = \prod_{y\in\mathcal{Y}} f_y(\underline{m}|\theta) = \prod_{y\in\mathcal{Y}} \prod_{A\in\mathcal{A}} \prod_{D\in\mathcal{Y}} f_{D,A}(m_{D,A,y}|\theta) \tag{IV.10}$$

by the adjusted likelihood (Pauli et al., 2011; Ribatet et al., 2012; Van de Vyver, 2015) :

$$f_{adj}(\underline{m}|\theta) = \{f_{ind}(\underline{m}|\theta)\}^{k(\hat{\theta}_{ind})}, \tag{IV.11}$$

where, denoting n the number of parameters ($n = 6$ in our case),

$$k(\hat{\theta}_{ind}) = n/\mathrm{tr}(I(\hat{\theta}_{ind})^{-1}V(\hat{\theta}_{ind})), \tag{IV.12}$$

with $\hat{\theta}_{ind}$ the set of parameters maximizing the independence likelihood (IV.10), tr the trace of the matrix and $I(\hat{\theta}_{ind})$ and $V(\hat{\theta}_{ind})$ the $n \times n$ matrices $I(\theta) = E(-\nabla^2 \log f_{ind}(\underline{m}|\theta))$ and $V(\theta) = cov(\nabla \log f_{ind}(\underline{m}|\theta))$ evaluated in $\hat{\theta}_{ind}$, which can be approximated by :

$$I(\theta) = -\sum_{y\in\mathcal{Y}} \frac{\partial^2 \log f_y(\underline{m}|\theta)}{\partial\theta\partial\theta^T}, \tag{IV.13}$$

$$V(\theta) = \sum_{y\in\mathcal{Y}} \frac{\partial \log f_y(\underline{m}|\theta)}{\partial\theta} \frac{\partial \log f_y(\underline{m}|\theta)}{\partial\theta^T}. \tag{IV.14}$$

The same I and V matrices are used in Mélèse et al. (2018) in a frequentist framework for correcting likelihood misspecification in IDF relationships. They are used in Van de Vyver (2015) in a Bayesian framework.

6.2. Technical details on the MCMC algorithm

6.2.1. Choice of the priors

For generality purpose, we use weakly informative priors for each of the six parameters, using either Gaussian or uniform densities. The parameters of these densities are set at region scale, based on the classification of the areal rainfall structure obtained in Mélèse et al. (2019) as follows. First, we consider the frequentist version of the IDAF model defined by Eq. (IV.3), which we estimate by maximum likelihood at 2149 pixels spread over the Massif Central and the foothills, including Mont Aigoual and Meyrueis pixels. Then, as a way of grouping together the pixels featuring similar extreme areal rainfall structure, we classify with K-means the normalized curves of Areal Reduction Factor (ARF) derived from Eq. (IV.2) as the multiplicative factor allowing to pass from the CDF of annual maxima for any (D, A_0) to that for any (D, A). Finally we consider the classes associated with Mont Aigoual and Meyrueis pixels, which are not the same.

For the Gumbel location parameter at the reference scale, $\boldsymbol{\mu}_0$, we choose a uniform prior density. Since rainfall intensity can not be negative, the lower bound is set to 0 mm/h/km^2. The upper bound is set to five times the maximum value of the maximum likelihood estimates of the location parameter within the corresponding class i.e. to 125 mm/h/km^2 for Mont Aigoual and to 55 mm/h/km^2 for Meyrueis. Likewise, we use a uniform prior density for the positive scale parameter at the reference scale, $\boldsymbol{\sigma}_0$, with the lower bound equal to 0.1 mm/h/km^2. The upper bound is set to 54.75 mm/h/km^2 for Mont Aigoual and to 21.75 mm/h/km^2 for Meyrueis. For the scaling parameter $\boldsymbol{H}$, we use a uniform prior density between 0 and 1 as in Van de Vyver (2015) and Mélèse et al. (2018) in an IDF framework. For $\boldsymbol{\omega}$, $\boldsymbol{\beta}$ and $\boldsymbol{\alpha}$ we use Gaussian prior densities. The Gaussian mean parameters are set to the averages of the maximum likelihood estimates of ω, β, α within the corresponding class, i.e. respectively to -0.039, 0.125, 0.401 for Mont Aigoual and -0.126, -0.003, 0.404 for Meyrueis. The Gaussian scale parameters are set to five times the standard deviation of the maximum likelihood estimates of ω, β, α within the corresponding class, i.e. respectively to 0.892, 0.713, 1.096 for Mont Aigoual and 1.838, 2.268, 1.813 for Meyrueis.

6.2.2. DRAM algorithm

One of the most popular MCMC techniques is the Metropolis-Hastings (MH) algorithm. At each step of the MH sampling, a new candidate is proposed for the parameter at hand using a jumping distribution and the acceptance ratio is computed. This acceptance ratio is used to decide whether to accept or reject the candidate. The DRAM algorithm improves the efficiency of the MH algorithm. It is based on two ideas : Delayed Rejection (DR) and Adaptive Metropolis (AM) sampling. The idea behind DR is that upon rejection of a candidate in a MH step, a second candidate is proposed based on a second jumping distribution. The AM step allows to tune the two jumping distributions based on the past sampled chain for better convergence. Here we consider symmetric jumping distributions. In order to correct for independence likelihood misspecification, we use the adjusted posterior density and the adjusted likelihood of Appendix A. In details DRAM algorithms proceeds as follows :

i. Draw a starting point $\theta^{(0)}$ for which $f(\theta^{(0)}|\underline{m})$ is defined and nonzero.

ii. At each step $t= 1, 2, ...,$

(a) Draw a candidate θ_1^* from a symmetric jumping distribution $J_{t,1}(\theta_1^*|\theta^{(t-1)})$.

(b) Derive the acceptance probability a_1 :

$$a_1 = \min\left\{1, \frac{f_{adj}(\theta_1^*|\underline{m})}{f_{adj}(\theta^{(t-1)}|\underline{m})}\right\} = \min\left\{1, \frac{f_{adj}(\underline{m}|\theta_1^*)f(\theta_1^*)}{f_{adj}(\underline{m}|\theta^{(t-1)})f(\theta^{(t-1)})}\right\}. \tag{IV.15}$$

(c) Accept the candidate θ_1^*, i.e. set $\theta^{(t)} = \theta_1^*$ with probability a_1, or continue the algorithm.

(d) Draw a second candidate θ_2^* from a second symmetric jumping distribution $J_{t,2}(\theta_2^*|\theta^{(t-1)})$.

(e) Derive the second acceptance probability a_2 :

$$a_2 = \min\left\{1, \frac{J_{t,1}(\theta_1^*|\theta_2^*)\left[f_{adj}(\theta_2^*|\underline{m}) - f_{adj}(\theta_1^*|\underline{m})\right]}{J_{t,1}(\theta_1^*|\theta^{(t-1)})\left[f_{adj}(\theta^{(t-1)}|\underline{m}) - f_{adj}(\theta_1^*|\underline{m})\right]}\right\}. \tag{IV.16}$$

(f) Accept or reject the candidate θ_2^*, i.e. set

$$\theta^{(t)} = \begin{cases} \theta_2^* \text{ with probability } a_2, \\ \theta^{(t-1)} \text{ otherwise.} \end{cases} \tag{IV.17}$$

The jumping distributions $J_{t,1}(.|\theta^{(t-1)})$ and $J_{t,2}(.|\theta^{(t-1)})$ are chosen to be Gaussian with means $\theta^{(t-1)}$ and covariance matrices respectively equal to $\Sigma_{t,1}$ and to $\Sigma_{t,2} = 0.1\Sigma_{t,1}$, as used in the test examples of Haario et al. (2006). The particular case when $\Sigma_{t,1}$ is hold fixed corresponds to the DR algorithm.

Initialization of $\Sigma_{0,1}$ is made in a preliminary step by running 1,000 iterations of the Metropolis algorithm, sampling the posterior distributions of the six model parameters separately. It uses univariate Gaussian jumping distributions whose standard deviations are tuned so that the acceptance rate (i.e. the proportion of candidates that are accepted) is between 30% and 50% since the optimal acceptance rate is approximately 0.44 for one dimensional target distributions (see Gelman et al., 2014, chapter 12).

vThen the DRAM algorithm used in this article includes three periods. The first period applies the DR algorithm up to iteration t_1. During this period $\Sigma_{t,1}$ is set to the diagonal matrix $\Sigma_{0,1}$.

The second period applies the DRAM algorithm up to iteration t_2. During this period we set

$$\Sigma_{t,1} = s_t\left\{C_{t-1} + \epsilon I_d\right\}, \tag{IV.18}$$

where C_{t-1} is the covariance matrix of $\underline{\theta}^{(t-1)} = \left(\theta^{(t_0)}, \ldots, \theta^{(t-1)}\right)$, I_d is a $d \times d$ identity matrix and $\epsilon = 10^{-5}$. The scalar s_t is initialized to $2.4^2/6$, which is the most efficient factor for six parameters following Gelman et al. (2014), chapter 12. Then it is tuned so that the acceptance rate is between 20% and 30%, since the optimal acceptance is 0.23 for a target distribution with dimension greater than 5 (see Gelman et al., 2014, chapter 12).

Finally, the third period applies the DR algorithm up to iteration t_3. During this period $\Sigma_{t,1}$ is hold fixed to $\Sigma_{t_2,1}$, the covariance matrix of Eq. (IV.18) obtained at iteration t_2 of the second period. The posterior density samples are obtained from this third period. In the article, t_1 and t_2 are respectively set to 2% and 50% of the MCMC chain length, which equals $t_3 = 200,000$ iterations. $\theta^{(0)}$ is set to the maximum likelihood estimate for the pixel.

Chapitre V

Rappel des principaux résultats et perspectives

1. Rappel des principaux résultats

La thèse présentée s'intéresse à la modélisation de l'aléa pluviométrique dans la région du Sud-Est de la France centrée sur les Cévennes. Elle propose un cadre d'estimation de l'aléa pluviométrique basé sur les propriétés d'invariance de la pluie, valide pour le continuum d'échelles spatio-temporelles, et permettant une quantification des incertitudes liées aux estimations des périodes et niveaux de retour.

Le Chapitre II s'est concentré sur les maxima ponctuels automnaux sur le continuum d'échelles temporelles. Un modèle IDF, basé sur des propriétés d'invariance par changement d'échelle, couplé à une distribution GEV fut estimée en 406 pluviomètres horaires à la fois dans le cadre fréquentiste et dans le cadre bayésien. Ceci a permis de montrer que le cadre bayésien est le cadre d'inférence le plus propice à la quantification de l'aléa pluviométrique notamment car l'estimation des incertitudes y est plus flexible et plus stable au nombre de données que dans le cadre fréquentiste. Le Chapitre III s'est concentré sur les maxima surfaciques automnaux sur le continuum d'échelles spatio-temporelles. Un modèle IDAF, basé sur des hypothèses d'invariance par changement d'échelle, a été développé dans le cadre fréquentiste. Ce modèle fut estimé en 2149 pixels issus de réanalyses radar. Ces dernières ont permis une analyse fine (jusqu'à 1 km^2 et 3 h) de la structure des maxima, précisant la compréhension des interactions entre les systèmes précipitants et la topographie à différentes échelles et mettant au jour de fortes disparités de l'aléa pluviométrique à faible distance. Enfin, dans le Chapitre IV, un cadre bayésien d'analyse de l'aléa pluviométrique pour le continuum d'échelles spatio-temporelles est développé. A partir du modèle de De Michele et al. (2001), développé ici dans un cadre bayésien, la

sévérité des 5 événements les plus rares apparus au sud de la crête des Cévennes durant la période 2008-2015, a été étudiée. L'aspect bayésien de ce cadre a permis de montrer l'apport de l'étude des incertitudes pour éviter une sous-estimation de la fréquence d'occurrence de ces événements. La forte variabilité de l'aléa pluviométrique à la fois à courtes distances ($\sim$ 15 km) et sur le continuum d'échelles spatio-temporelles, en un lieu donné, a été mise en avant.

2. Perspectives

2.1. Détection des régions sous échantillonnées (6 mois) et augmentation des données (-)

La période d'observation des réanalyses étant courte (8 ans) il est probable que certaines parties de notre région d'étude soient sous échantillonnées. Une étude de la sensibilité à l'estimation des modèles considérés dans les Chapitre III et IV peut permettre de détecter ces régions.

Une remarque préambulaire : le Chapitre I explique que les situations engendrant des systèmes pluviométriques intenses dans notre région d'étude sont principalement issues de l'interaction entre la topographie et les systèmes convectifs de méso-échelle. Sur le relief l'interaction entre les détails de la topographie et ces systèmes crée des bandes pluvieuses orientées nord-sud, caractérisées par une convection peu profonde, s'intensifiant le long de la crête. Dans le piémont l'interaction produit essentiellement des systèmes pluviométriques caractérisés par une convection plus profonde et dont la position est très variable d'un système à l'autre. Ceci combiné aux premiers tests effectués dans le cadre du Chapitre III nous porte à craindre que les 8 années d'observation sont insuffisantes pour échantillonner les maxima automnaux dans le piémont au contraire du relief. Cette section propose de confirmer ces dires en détectant de manière statistique les sous-régions sous échantillonnées.

On se place dans le cadre du Chapitre IV. Une procédure possible pour détecter ces régions est la suivante : pour chaque pixel, on dispose de la base de données, DBch2, des intensités maximales pour le continuum d'échelles spatio-temporelles dont la construction est expliquée au Chapitre III. On construit une nouvelle base de données de maxima, DBM, à partir des réanalyses où on a enlevé l'événement le plus rare (au sens décrit ci-dessous), EVTf, enregistré au pixel considéré. On dispose donc de deux bases de données de maxima : DBch2 et DBM. En chaque pixel, on estime le modèle du Chapitre IV sur chacune de ces bases de données. Pour chaque couple (D, A), on obtient donc deux estimations de la densité *a posteriori* de la période de retour de l'événement EVTf. Enfin, pour chaque couple (D, A) on calcule une distance entre ces deux densités.

Deux difficultés sont alors à résoudre. La première est la caractérisation de l'événement le plus rare. Ce choix sera probablement guidé par un compromis entre les valeurs des périodes de retour de DBch2 et leurs extensions en termes d'échelles spatio-temporelles. La seconde est le choix de la distance entre les deux densités et le seuil à partir duquel on considère le pixel comme sous échantillonnée. Une distance possible est la distance de Hellinger, notée He ci-après, dont le carré est défini pour deux densités f et g par :

$$He^2(f,g) = \frac{1}{2}\int \left\{\sqrt{f(x)} - \sqrt{g(x)}\right\}^2 dx.$$

Pour chaque couple (D, A) on obtient une valeur de cette distance et donc un diagramme de He en fonction de (D, A), ceci pour chaque pixel de notre région. Le seuil à partir duquel on considère un pixel comme sous échantillonné devra être défini en visualisant à quelle écart entre les densités correspond la distance He. Enfin, si des sous ensembles de couples (D, A) peuvent être identifier comme ayant des valeurs similaires de He, on pourra définir un seuil de détection global pour ces sous ensembles. Sinon il faudra définir ce seuil pour chaque couple (D, A).

Une fois les régions sous-échantillonnées détectées une méthode appelée transposition stochastique de tempête (*Stochastic storm transposition* - SST - en anglais) développée dans Foufoula-Georgiou (1989) permettrait d'augmenter le nombre de données pluviométriques dans ces régions. Cette méthode utilise la structure spatiales des événements pluviométriques et est donc particulièrement adaptée aux données radar (Wright et al., 2013, 2014). Cette méthode peut être vue comme un reéchantillonnage des événements pluviométriques les plus intenses par transposition spatiale. Cependant la région des Cévennes est caractérisée par une grande hétérogénéité et un positionnement des précipitations forcé par la topographie. Il semble alors difficile d'appliquer cette méthode telle qu'elle est présentée dans Wright et al. (2013). La méthode et les critères de transposition devraient alors être repensés.

2.2. Non stationnarité de la sévérité (18 mois)

Blanchet et al. (2016b) montre une tendance d'augmentation des maxima annuels de cumul journalier ces 30 dernières années sur notre région d'étude (de l'ordre de 40 mm/jour durant la période 1985-2014 sur la crête et environ 30% d'augmentation sur la crête et la partie est du piémont, voir la Fig. V.1). Ainsi l'hypothèse de climat stationnaire faite dans ce document est discutable et peut mener à une sous estimation des périodes et niveaux retour ainsi que des incertitudes associées. Pour prendre en compte la non stationnarité du climat et ainsi les changements possibles de l'intensité maximale au cours du temps, il est commun d'introduire une dépendance entre les paramètres de la distribution des maxima considérée et le temps (Blanchet et al., 2016b). Cheng and AghaKouchak (2014) et Sarhadi and Soulis (2017) introduisent une telle dépendance dans des modèles IDF pour en étudier la non stationnarité. A notre connaissance aucune étude sur la non stationnarité des courbes IDAF a été proposée.

On considère que $\boldsymbol{M}(D_0, A_0)$, la variable aléatoire des intensités maximales automnales pour une durée D_0 et une aire A_0, suit une distribution GEV

$$\mathrm{pr}\left\{\boldsymbol{M}(D_0, A_0) < x\right\} = \exp\left\{-\left[1 + \xi\left(\frac{x - \mu_0}{\sigma_0}\right)\right]^{-1/\xi}\right\}, \tag{V.1}$$

avec $1 + \xi\left(\frac{x-\mu_0}{\sigma_0}\right) > 0$ et où μ_0, σ_0 et ξ sont, respectivement, les paramètres de lieu, d'échelle et de forme de la distribution GEV. Le modèle IDAF développé au Chapitre III stipule que, quelque soit (D, A), la distribution de la variable aléatoire des intensités maximales automnales pour une durée D et une aire A, $\mathrm{pr}\left\{\boldsymbol{M}(D, A) < x\right\}$, suit une distribution GEV

$$\mathrm{pr}\left\{\boldsymbol{M}(D, A) < x\right\} = \exp\left\{-\left[1 + \xi\left(\frac{x - \mu_{D,A}}{\sigma_{D,A}}\right)\right]^{-1/\xi}\right\}, \tag{V.2}$$

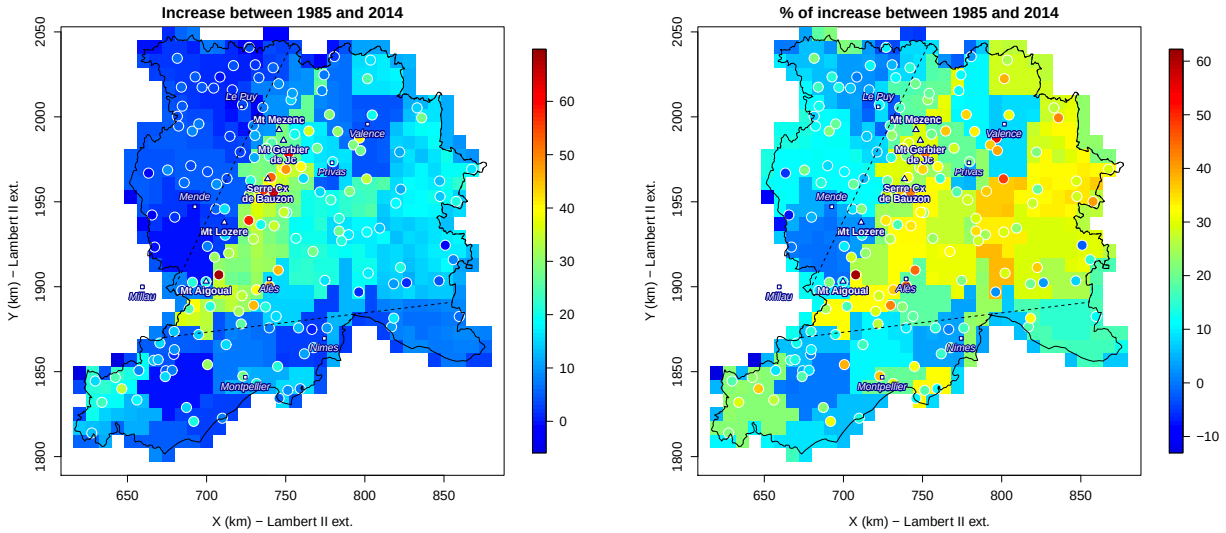

FIGURE V.1 – Tendance de l'évolution des maxima annuels journaliers entre 1985 et 2014, issu de Blanchet et al. (2016b). Droite : évolution en intensité (mm/jour). Gauche : évolution en pourcentage par rapport à la moyenne des maxima annuels de chaque série temporelle. Les deux lignes en point-tillés délimitent la zone où on trouve la majeur partie des tendances significatives.

de paramètres de lieu $\mu_{D,A} = r_{D_0}(D, A, A_0)\mu_0$, d'échelle $\sigma_{D,A} = r_{D_0}(D, A, A_0)\sigma_0$ et de forme ξ. On rappelle que

$$r_{D_0}(D, A, A_0) = \left(\frac{D}{D_0}\right)^{-H} \left(\frac{1 + \sum_{i=1}^{R} \omega_i D^{-\beta_i} A^{\alpha_i}}{1 + \sum_{i=1}^{R} \omega_i D_0^{-\beta_i} A_0^{\alpha_i}}\right)^{\gamma}, \tag{V.3}$$

modélise la structure spatio-temporelle des maxima. Ainsi sous hypothèse que la structure des pluies les plus rares ne varie pas au cours des années (r stationnaire) mais que leurs distributions à (D_0, A_0) évoluent , on peut considérer une dépendance au temps des paramètres μ_0, σ_0 et ξ. Le paramètre ξ étant difficile à estimer, il est raisonnable de considérer cette dépendance seulement pour μ_0, σ_0. Autrement dit on pose $\mu_0 = f(t)$ et $\sigma_0 = g(t)$ avec f et g des fonctions, respectivement, à valeur dans $\mathbb{R}$ et $\mathbb{R}_+^*$, et t le temps.

Un premier point de blocage à cette méthode est qu'elle impose que la tendance sur $\mu_{D,A}$ et $\sigma_{D,A}$ hérite directement de la tendance sur μ_0 et σ_0. Par exemple, si μ_0 augmente de 10% en 50 ans alors chaque $\mu_{D,A}$ augmente de $r \times 10\%$ en 50 ans. Or, il est peu probable que l'évolution de la distribution des maxima automnaux soit transposable à toutes les échelles spatio-temporelles (D, A), ceci car les maxima pour des grandes durées et aires ne proviennent pas nécessairement des mêmes systèmes précipitants que les maxima de petite durées et aires. Il faudrait alors détecter des classes d'échelles spatio-temporelles susceptibles de présenter une évolution similaire et estimer le modèle sur chacune des ces classes. Une hypothèse pourrait être de considérer qu'un type de systèmes précipitants donné (par exemple les systèmes en V, ou encore les systèmes en bandes, présentés au Chapitre I) est susceptible de présenter une évolution temporelle similaire sur les échelles spatio-temporelles qu'il impacte le plus. Un premier travail serait donc de produire une classification des événements en type de systèmes précipitants. Cette classification devra être faite en collaboration avec un hydrométéorologue.

Un second point de blocage est qu'un tel modèle ne peut pas être estimé à partir des réanalyses radar présentées au Chapitre I et utilisées aux Chapitre II et III du fait de leurs courte période d'observation (8 ans). La base de données de précipitation surfacique SPAZM (Penot, 2014; Gottardi et al., 2012), de résolution spatiale 1 km^2 et temporelle 24 h, avec 52 années observées pourrait alors être utilisée. Cette base de données étant construite à partir d'une interpolation de pluviomètres, l'estimation des intensités pluviométriques les plus fortes pour les petites échelles surfaciques (< 100 km^2) est de moins bonne qualité par rapport à celle issue des réanalyses (Penot, 2014). Il faudrait donc sélectionner les échelles surfaciques A pour lesquelles l'estimation des intensités les plus fortes issue de SPAZM s'approche, en terme de distance euclidienne, de celle issue des réanalyses.

Ces deux points de blocage levés, la première étape pour l'étude de la non stationnarité de la sévérité serait d'estimer le modèle défini à l'Eq. (V.2), sous hypothèse de stationnarité, sur des fenêtres glissantes de 20 ans. Pour chaque fenêtre on obtiendrait alors une estimation des paramètres μ_0 et σ_0 permettant ainsi de les visualiser en fonction de t et donc de choisir les fonctions f et g.

Néanmoins différentes études montrent une évolution de la structure des précipitations les plus intenses (par exemple Blanchet et al. (2018) en Afrique de l'ouest et Wasko et al. (2016) en Australie). Ainsi, dans un second temps, on pourrait investiguer l'évolution de la structure des précipitations extrêmes. Le ratio r de l'Eq. (V.3) modélisant la structure spatio-temporelle, cela reviendrait à faire dépendre ses paramètres du temps. Un point de blocage est que les paramètres $(\omega_i, \beta_i, \alpha_i, \gamma)$ de l'Eq. (V.3) sont non identifiables pour $R > 1$ et non orthogonaux (effets de compensation). Il faudrait alors reparamétriser ce modèle pour obtenir un modèle aux paramètres plus identifiables.

2.3. Vers une meilleure estimation de l'aléa pluviométrique et des incertitudes associées en relâchant l'hypothèse d'indépendance entre les maxima de différentes échelles spatio-temporelles (36 mois)

La vraisemblance considérée dans les Chapitres III et dans IV est définie sous hypothèse d'indépendance entre les maxima des différentes échelles spatio-temporelles. Son expression logarithmique s'écrit

$$l(\theta) = \sum_{A \in \mathcal{A}} \sum_{D \in \mathcal{D}} \sum_{y \in \mathcal{Y}} \log f_{D,A}(m_{D,A,y}; \theta) \tag{V.4}$$

où $f_{D,A}$ est la densité d'une GEV associée à un couple (D, A), θ représente les paramètres qui régissent cette densité, $\mathcal{A}$ est l'ensemble des aires considérées, $\mathcal{D}$ est l'ensemble des durées, $\mathcal{Y}$ est l'ensemble des années et $m_{D,A,y}$ le maxima pour la durée D, la surface A et l'année y. Cette hypothèse est discutable car, par exemple, pour un lieu et une année donnés, l'intensité maximale à (4 h, 50 km^2) peut être issue de l'intensité maximale à (3 h, 50 km^2). Dans les modèles IDF et IDAF présentés dans ce document, on s'intéresse aux distributions marginales. Comme le montrent Sebille et al. (2017) et Schellander and Hell (2018), l'influence du relâchement de cette hypothèse devrait être faible sur les estimations des niveaux et périodes retour (i.e. sur leurs modes ou moyennes *a posteriori* dans le cadre bayésien). Cependant elle peut avoir une certaine incidence sur l'estimation des incertitudes.

En enlevant l'hypothèse d'indépendance entre les maxima pour différentes échelles spatio-temporelles on obtient :

$$l(\theta, \psi) = \sum_{y \in \mathcal{Y}} \log f(m_{1,y} \dots m_{n,y}; \theta, \psi) \tag{V.5}$$

avec ψ les paramètres régissant la dépendance entre les maxima pour différentes échelles spatio-temporelles et où les $m_{i,y}$ sont les maxima pour les couples (D, A) considérés pour l'estimation, et pour l'année y. Il y a $n = 90$ couples (D, A) considérés pour l'estimation dans les Chapitres III et IV. La variable aléatoire des maxima pour tous les couples (D, A), $M = \{M_i, i \in \mathcal{D} \times \mathcal{A}\}$, peut être vue comme un processus spatial sur l'espace des couples (D, A), i.e. sur $\mathcal{D} \times \mathcal{A}$. Chaque $m_{1,y} \dots m_{n,y}$ est alors une réalisation de M en n points de $\mathcal{D} \times \mathcal{A}$. La théorie des extrêmes spatiaux Davison et al. (2012) nous dit alors que f est modélisable par un processus max stable sur l'espace $\mathcal{D} \times \mathcal{A}$. Pour fixer les idées, on choisit dans la suite d'illustrer nos propos avec M suivant un processus de Brown-Resnick (Kabluchko et al., 2009) car il est l'un des plus flexibles et robustes (Nicolet et al., 2017). Cependant d'autres modèles max-stables ou max stables inverses (Le et al., 2018) pourraient être envisagés.

Une expression de la distribution bivariée d'un processus de Brown-Resnick (Kabluchko et al., 2009) est

$$\text{pr}(M_i < m_i, M_j < m_j) = \exp\left\{-\frac{1}{z_i}\Phi\left(\frac{a_{ij}}{2} + \frac{1}{a_{ij}}\log\frac{z_j}{z_i}\right) - \frac{1}{z_j}\Phi\left(\frac{a_{ij}}{2} + \frac{1}{a_{ij}}\log\frac{z_i}{z_j}\right)\right\}, \tag{V.6}$$

où M_i et M_j sont, respectivement, les variables aléatoires des maxima pour i-ième et le j-ième couple (D, A), $a_{ij} = \{2\gamma(||e_i - e_j||)\}^{1/2}$ avec $||e_i - e_j||$ la distance entre le i-ème et le j-ème couple (D, A). Un choix possible de γ est le suivant Kabluchko et al. (2009)

$$\gamma(||e_i - e_j||) = \left(\frac{||e_i - e_j||}{\lambda}\right)^{\kappa}$$

avec $\lambda > 0$ et $0 < \kappa < 2$. A noter qu'un premier travail sera de définir une distance sur $\mathcal{D} \times \mathcal{A}$. également, ona

$$z_p = \left\{1 + \xi\left(\frac{m_p - \mu_p}{\sigma_p}\right)\right\}^{1/\xi},$$

où l'indice p représente le p-ième couple (D, A) et donc μ_p et σ_p les paramètres de position et d'échelle de la distribution marginale M_p qui est une GEV(μ_p, σ_p, ξ). L'Eq. (V.6) permet de modéliser la dépendance entre deux maxima à deux échelles spatio-temporelles différentes et ainsi de prendre en compte la structure de dépendance entre tous les maxima à différentes échelles spatio-temporelles.

Dans le cadre de la modélisation IDAF présenté au Chapitre IV, le modèle de l'Eq. (V.6) contient 9 paramètres qui sont les paramètres des lois marginales, i.e. $\theta = (\mu_0, \sigma_0, \xi, H, \omega, \alpha, \beta)$, et les paramètres modélisant la dépendance entre le i-ième et le j-ième couple (D, A), i.e. $\psi = (\lambda, \kappa)$. En supposant que les intensités maximales sont indépendantes d'une année à l'autre, la log vraisemblance d'un tel modèle correspond à l'Eq. (V.5) avec f la densité d'un processus de Brown-Resnick n varié. Cependant, on ne connait l'expression analytique de la distribution jointe d'un tel processus que pour n petit ($n = 2$ ou $n = 3$) et, même si cette distribution était connue pour n termes, sa dérivation pour obtenir la densité f de l'Eq. (V.5) serait numériquement impossible car elle mettrait

en jeu un nombre de termes correspondant au n-ième nombre de Bell (Davison and Gholamrezaee, 2011). Padoan et al. (2010) proposent de remplacer l'optimisation de la vraisemblance de l'Eq. (V.4) par l'optimisation d'une vraisemblance composite Varin et al. (2011) qui est, dans notre cas, appelée vraisemblance par paire. Son expression est

$$l(\theta, \psi) = \sum_{y \in \mathcal{Y}} \sum_{1<i<j<n} \log f_{ij}(m_{i,y}, m_{j,y}; \theta, \psi), \tag{V.7}$$

où f_{ij} est la densité associée à la distribution bivariée d'un processus de Brown-Resnick (Eq. V.6), θ représente les paramètres des distributions GEV marginales et ψ les paramètres modélisant la dépendance entre le i-ième et le j-ième couple (D, A). Padoan et al. (2010) montrent que l'estimateur de maximum de vraisemblance par paire est asymptotiquement non biaisé.

Dans les Chapitres III et IV, on considère 90 couples (D, A) pour l'estimation du modèle IDAF. Sous hypothèse d'indépendance, la vraisemblance associée à ces modèles est écrite à l'Eq. (V.4) avec $f_{D,A}$ la densité d'une distribution de Gumbel. Ainsi à chaque fois que la vraisemblance est calculée, la densité $f_{D,A}$ est calculée 720 fois (nombre d'années multiplié par le nombre de couples (D, A)). Lorsqu'on relâche l'hypothèse d'indépendance, on optimise la vraisemblance composite de l'Eq. (V.7). En considérant 90 couples (D, A), on obtient alors 4005 paires (D, A), (D', A') et donc, à chaque fois que la vraisemblance sera calculée, la densité f_{ij} sera calculée 32040 fois (nombre d'années multiplié par nombre de paires (D, A) (D', A')) ce qui posera des difficultés numériques. il sera donc compliqué numériquement de faire assez d'itérations pour atteindre la convergence. Une possibilité est de considérer un sous ensemble de l'ensemble des paires (D, A),(D', A') pour l'optimisation afin de réduire le nombre de termes. A noter également que dans les cas des Chapitres III et IV la distribution marginale des valeurs extrêmes considérée est une distribution de Gumbel. Dans le cas d'une distribution GEV, l'optimisation de la fonction définie à l'Eq. (V.7) est plus compliqué car la GEV n'est pas définie partout.

Enfin le modèle de Brown-Resnick, présenté à l'Eq. (V.6), est écrit dans le cadre fréquentiste. Cependant on a montré que le cadre bayésien est plus propice à l'estimation de l'aléa pluviométrique. Un point de blocage est que la vraisemblance par paire définie à l'Eq. (V.7) n'est pas une vraisemblance. Son utilisation dans la formule de Bayes conduit à des distributions *a posteriori* biaisées et trop concentrées car elle traite les observations de paires comme si elles étaient mutuellement indépendantes. Il conviendra donc d'ajuster l'échantillonnage par MCMC pour obtenir les densités *a posteriori* qu'on est sensé obtenir avec la vraisemblance jointe. Une première possibilité serait de recourir aux corrections de la vraisemblance par paire proposées par Ribatet and Sedki (2012) et utilisé par Van de Vyver (2015) dans un cadre IDF. Une seconde alternative serait d'avoir recours à de l'échantillonnage bayésien approximé (Erhardt and Smith, 2012).

2.4. Aléa pluviométrique sur des bassins versants (24 mois)

L'aléa hydrologique dépend de la forme des bassins versant sur lesquels la pluie s'accumule. Ainsi il serait intéressant d'étudier l'aléa pluviométrique en considérant la forme des bassins versants pour l'accumulation surfacique de la pluie alors que dans les Chapitres III et IV on considérait des surfaces carrées.

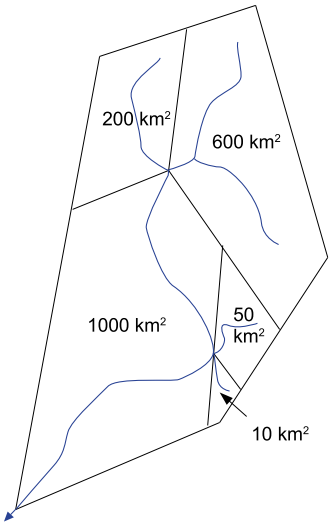

FIGURE V.2 – Schéma d'un exemple de maillage d'un bassin versant en sous bassins de différentes surfaces. Les traits bleus représentent les rivières et la flèche en bas à gauche l'exutoire.

La Fig. V.2 représente un schéma de maillage d'un bassin versant en sous bassins de différentes surfaces. A noter que cette figure sert à titre d'illustration, et que dans un cas réel le maillage d'un bassin sera conduit en collaborations avec un hydrologue permettant d'obtenir un maillage qui considère les sous bassins propices aux crues. On appelle BV le bassin versant. BV est maillé en 5 sous bassins de surfaces 10, 50, 200, 600 et 1000 km^2. La surface totale de BV est donc 1860 km^2. L'idée est de construire des séries d'intensité maximale pluviométrique surfacique en respectant la forme et la surface de BV et de ses sous bassins. Pour cela, à partir des réanalyses, on accumule les précipitations sur BV et chacun de ses sous bassins ce qui nous donne des séries d'intensité surfacique horaire pour les surfaces 10, 50, 200, 600 et 1000 km^2. On extrait ensuite les séries d'intensité maximale pluviométrique pour des agrégations temporelles 3, 4, 6, 8, 12, 16, 24, 36 et 48 h.

Une première étape pourrait être alors de construire un modèle IDF pour BV et chacun de ses sous bassins séparément. Pour un bassin donné, on pourra commencer par vérifier les hypothèses de changement d'échelle simple sur les maxima de chaque sous bassin, avec les méthodes décrites dans la Section 4 du Chapitre II. Plus précisément la Fig. V.3 donne quatre maillages plus ou moins fins de notre région en bassins versants. On pourrait alors estimer un modèle IDF sur chaque bassin de chaque maillage et regarder comment varie la distribution des intensités maximales lorsqu'on passe d'un maillage à un autre. Le paramètre d'abattement temporel H pourra en particulier nous informer sur la variabilité temporelle des précipitations engendrant des maxima aux différentes échelles temporelles. Par exemple un H plus petit lorsque la taille des sous-bassins augmente signifierait que les précipitations produisant des maxima sur des petites échelles ont tendance à être plus concentrées que celles qui produisent des maxima sur une plus grande échelle.

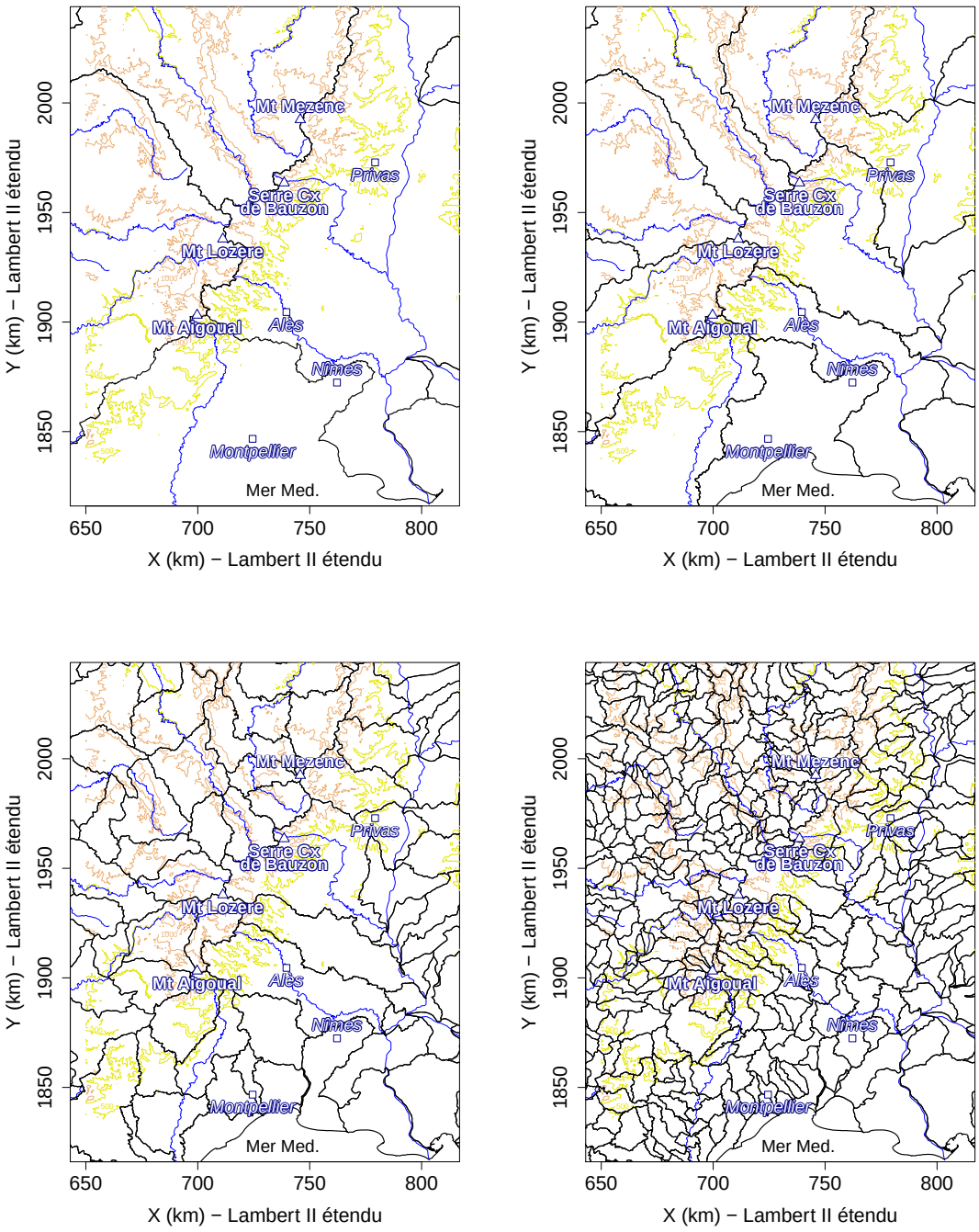

FIGURE V.3 – Maillage plus ou moins fin de notre région d'étude en bassins versants, issu de la base de donnée Carthage. Les frontières des bassins versants sont représentées en noire, les principales rivières en bleu, le relief avec les courbes de niveau 500 (jaune) et 1000 (marron) mètres au dessus du niveau de la mer.

Toujours dans l'idée de mieux comprendre comment s'organisent dans l'espace les précipitations donnant des maxima à différentes échelles spatiales, une seconde étape pourrait par exemple regarder si les maxima de sous-bassins d'une échelle donnée "résonnent" de manière concomitante : les maxima des sous bassins ont ils tendance à être particulièrement fort "en même temps" ? Une limite à cela est que la concomitance est ici à attendre à l'échelle annuelle.

Le même raisonnement pourrait être conduit entre un bassin à une échelle spatiale donnée et ses sous bassins aux échelles spatiales inférieures. Cela permettrai, par exemple, de comprendre si les maxima du bassin considéré ont tendance à être produits par des maxima d'un de ses sous bassins en particulier, ou bien, par des fortes pluies sur tout le bassin, c'est à dire des fortes pluies concomitantes à tous ses sous bassins. Cette étude pourrait être faite en faisant varier la durée D pour étudier les différences de résonance spatiale des maxima selon la durée considérée.

Une difficulté à ces études est le fait que la région du piémont est probablement sous échantillonnée dans les réanalyses radar à disposition. A partir de l'étude de la Section 2.1 il faudra voir si certains bassins versants sont bien échantillonnés, et si ce n'est pas le cas utilisé la base de donnée de précipitation journalière SPAZM en sachant qu'on pourra alors seulement étudier l'aléa lié aux réactions assez lentes des bassins versants puisque SPAZM a une résolution journalière et les maxima sur les petites échelles surfaciques sont sous estimés (Penot, 2014).

Bibliographie

Allen, R. and Degaetano, A. (2005). Areal reduction factors for two eastern united states regions with high rain-gauge density. 10 :327–335.

Anquetin, S., Minsicloux, F., Creutin, J.-D., and Cosma, S. (2003). Numerical simulation of orographic rainbands. Journal of Geophysical Research : Atmospheres, 108(D8). 8386.

Beirlant, J., Goegebeur, Y., Teugels, J., and Segers, J. (2005). Statistics of Extremes. John Wiley & Sons, Ltd.

Berger, J. (2006). The case for objective bayesian analysis. Bayesian Anal., 1(3) :385–402.

Berne, A. and Krajewski, W. (2013). Radar for hydrology : Unfulfilled promise or unrecognized potential ? Advances in Water Resources, 51 :357 – 366. 35th Year Anniversary Issue.

Blanchet, J., Aly, C., Vischel, T., Panthou, G., Sané, Y., and Kane, M. D. (2018). Trend in the co-occurrence of extreme daily rainfall in West Africa since 1950. Journal of Geophysical Research : Atmospheres. 2017JD027219.

Blanchet, J., Ceresetti, D., Molinié, G., and Creutin, J.-D. (2016a). A regional GEV scale-invariant framework for intensity duration frequency analysis. Journal of Hydrology, 540 :82 – 95.

Blanchet, J. and Creutin, J.-D. (2017). Co-Occurrence of Extreme Daily Rainfall in the French Mediterranean Region. Water Resources Research, 53(11) :9330–9349.

Blanchet, J., Molinié, G., and Touati, J. (2016b). Spatial analysis of trend in extreme daily rainfall in southern France. Climate Dynamics, pages 1–14.

Borga, M., Vezzani, C., and Fontana, G. D. (2005). Regional rainfall depth–duration–frequency equations for an alpine region. Natural Hazards, 36(1) :221–235.

Boudevillain, B., Delrieu, G., Wijbrans, A., and Confoland, A. (2016). A high-resolution rainfall re-analysis based on radar-raingauge merging in the Cévennes-Vivarais region, France. Journal of Hydrology, 541(Part A) :14 – 23. Flash floods, hydro-geomorphic response and risk management.

Bougadis, J. and Adamowski, K. (2006). Scaling model of a rainfall intensity-duration-frequency relationship. Hydrological Processes, 20(17) :3747–3757.

Bousquet, O., Ribaud, J.-F., Grazioli, J., Berne, A., and Delanoë, J. (2013). Interactions between airflow dynamics and cloud microphysics in complex terrain : The 24 september 2012 hpe observed during HyMeX IOP6. HyMeX Workshop, Cassis, France.

Burlando, P. and Rosso, R. (1996). Scaling and muitiscaling models of Depth-Duration-Frequency curves for storm precipitation. Journal of Hydrology, 187(1) :45–64.

Byrd, R. H., Lu, P., Nocedal, J., and Zhu, C. (1995). A limited memory algorithm for bound constrained optimization. SIAM Journal on Scientific Computing, 16(5) :1190–1208.

Carreau, J., Neppel, L., Arnaud, P., and Cantet, P. (2013). Extreme Rainfall Analysis at Ungauged Sites in the South of France : Comparison of Three Approaches. Journal de la Société Française de Statistique, 154(2) :119–138.

Cattiaux, J. and Ribes, A. (2018). Defining single extreme weather events in a climate perspective. Bulletin of the American Meteorological Society, 99(8) :1557–1568.

Ceresetti, D. (2011). Space-time structure of heavy rainfall events : application to the Cévennes-Vivarais region. Theses, Université Joseph-Fourier - Grenoble I.

Ceresetti, D., Anquetin, S., Molinié, G., Leblois, E., and Creutin, J.-D. (2012). Multiscale evaluation of extreme rainfall event predictions using severity diagrams. Weather and Forecasting, 27(1) :174–188.

Ceresetti, D., Molinié, G., and Creutin, J.-D. (2010). Scaling properties of heavy rainfall at short duration : a regional analysis. Water Resources Research, 46(9).

Chandra, R., Saha, U., and Mujumdar, P. (2015). Model and parameter uncertainty in IDF relationships under climate change . Advances in Water Resources, 79 :127 – 139.

Cheng, L. and AghaKouchak, A. (2014). Nonstationary precipitation Intensity-Duration-Frequency curves for infrastructure design in a changing climate. Scientific reports, 4.

Coles, S., Bawa, J., Trenner, L., and Dorazio, P. (2001). An introduction to statistical modeling of extreme values, volume 208. Springer.

Coles, S. and Pericchi, L. (2003). Anticipating catastrophes through extreme value modelling. Journal of the Royal Statistical Society : Series C (Applied Statistics), 52(4) :405–416.

Coles, S. G. and Tawn, J. A. (1996). A bayesian analysis of extreme rainfall data. Journal of the Royal Statistical Society. Series C (Applied Statistics), 45(4) :463–478.

Cooley, D., Cisewski, J., Erhardt, R. J., Jeon, S., Mannshardt, E., Omolo, B. O., and Sun, Y. (2012). A survey of spatial extremes : Measuring spatial dependence and modeling spatial effects. REVSTAT, 10(1) :135–165.

Davison, A. and Huser, R. (2015). Statistics of Extremes. Annual Review of Statistics and Its Application, 2(1) :203–235.

Davison, A. C. (2008). Statistical Models. Cambridge University Press, 1 edition.

Davison, A. C. and Gholamrezaee, M. M. (2011). Geostatistics of extremes. Proceedings of the Royal Society of London A : Mathematical, Physical and Engineering Sciences.

Davison, A. C., Padoan, S. A., and Ribatet, M. (2012). Statistical modeling of spatial extremes. Statistical science, pages 161–186.

De Michele, C., Kottegoda, N., and Rosso, R. (2002). IDAF (Intensity-Duration-Area-Frequency) curves of extreme storm rainfall : a scaling approach. Water Science & Technology, 45(2) :83–90.

De Michele, C., Kottegoda, N. T., and Rosso, R. (2001). The derivation of areal reduction factor of storm rainfall from its scaling properties. Water Resources Research, 37(12) :3247–3252.

De Michele, C., Zenoni, E., Pecora, S., and Rosso, R. (2011). Analytical derivation of rain Intensity-Duration-Area-Frequency relationships from event maxima. Journal of Hydrology, 399(3) :385 – 393.

Delrieu, G., Nicol, J., Yates, E., Kirstetter, P.-E., Creutin, J.-D., Anquetin, S., Obled, C., Saulnier, G.-M., Ducrocq, V., Gaume, E., Payrastre, O., Andrieu, H., Ayral, P.-A., Bouvier, C., Neppel, L., Livet, M., Lang, M., du Châtelet, J. P., Walpersdorf, A., and Wobrock, W. (2005). The catastrophic flash-flood event of 8 and 9 september 2002 in the gard region, france : A first case study for the cévennes vivarais mediterranean hydrometeorological observatory. Journal of Hydrometeorology, 6(1) :34–52.

Delrieu, G., Wijbrans, A., Boudevillain, B., Faure, D., Bonnifait, L., and Kirstetter, P.-E. (2014). Geostatistical radar-raingauge merging : A novel method for the quantification of rain estimation accuracy. Advances in Water Resources, 71 :110 – 124.

Drobinski, P., Ducrocq, V., Alpert, P., Anagnostou, E., BÃl'ranger, K., Borga, M., Braud, I., Chanzy, A., Davolio, S., Delrieu, G., Estournel, C., Boubrahmi, N. F., Font, J., Grubišié, V., Gualdi, S., Homar, V., Ivančan-Picek, B., Kottmeier, C., Kotroni, V., Lagouvardos, K., Lionello, P., Llasat, M. C., Ludwig, W., Lutoff, C., Mariotti, A., Richard, E., Romero, R., Rotunno, R., Roussot, O., Ruin, I., Somot, S., Taupier-Letage, I., Tintore, J., Uijlenhoet, R., and Wernli, H. (2014). HyMeX : A 10-Year Multidisciplinary Program on the Mediterranean Water Cycle. Bulletin of the American Meteorological Society, 95(7) :1063–1082.

Duclos, P., Vidonne, O., Beuf, P., Perray, P., and Stoebner, A. (1991). Flash flood disaster-Nîmes, France, 1988. European Journal of Epidemiology, 7(4) :365–371.

Ducrocq, V., Braud, I., Davolio, S., Ferretti, R., Flamant, C., Jansa, A., Kalthoff, N., Richard, E., Taupier-Letage, I., Ayraland, P., Belamariand, S., Berneand, A., Borgaand, M., Boudevillain, B.,

Bock, O., Boichard, J.-L., Bouin, M.-N., Bousquet, O., Bouvier, C., Chiggiato, J., Cimini, D., Corsmeier, U., Coppola, L., Cocquerez, P., Defer, E., Delanoë, J., Di Girolamo, P., Doerenbecher, A., Drobinski, P., Dufournet, Y., FourriÃl', N., Gourley, J., Labatut, L., Lambert, D., Le Coz, J., Marzano, F., Molinié, G., Montani, A., Nord, G., Nuret, M., Ramage, K., Rison, B., Roussot, O., Said, F., Schwarzenboeck, A., Testor, P., Van-Baelen, J., Vincendon, B., Aran, M., and Tamayo, J. (2013). Hymex-sop1, the field campaign dedicated to heavy precipitation and flash-flooding in the northwestern mediterranean. Available on line.

Ducrocq, V., Nuissier, O., Ricard, D., Lebeaupin, C., and Thouvenin, T. (2008). A numerical study of three catastrophic precipitating events over southern france. II : Mesoscale triggering and stationarity factors. Quarterly Journal of the Royal Meteorological Society, 134(630) :131–145.

Durrans, S. R., Julian, L. T., and Yekta, M. (2002). Estimation of depth-area relationships using radar-rainfall data. Journal of Hydrologic Engineering, 7(5) :356–367.

Efron, B. (2005). Bayesians, frequentists, and scientists. Journal of the American Statistical Association, 100(469) :1–5.

Eggert, B., Berg, P., Haerter, J. O., Jacob, D., and Moseley, C. (2015). Temporal and spatial scaling impacts on extreme precipitation. Atmospheric Chemistry and Physics, 15(10) :5957–5971.

Erhardt, R. J. and Smith, R. L. (2012). Approximate bayesian computing for spatial extremes. Computational Statistics & Data Analysis, 56(6) :1468 – 1481.

Evin, G., Blanchet, J., Paquet, E., Garavaglia, F., and Penot, D. (2016). A regional model for extreme rainfall based on weather patterns subsampling. Journal of Hydrology, 541(B) :1185–1198.

Foufoula-Georgiou, E. (1989). A probabilistic storm transposition approach for estimating exceedance probabilities of extreme precipitation depths. Water Resources Research, 25(5) :799–815.

Gaume, E., Livet, M., Desbordes, M., and Villeneuve, J.-P. (2004). Hydrological analysis of the river aude, france, flash flood on 12 and 13 november 1999. Journal of Hydrology, 286(1 4) :135 – 154.

Gelman, A., Carlin, J. B., Stern, H. S., Dunson, D. B., Vehtari, A., and Rubin, D. B. (2014). Bayesian Data Analysis. Chapman & Hall/CRC Texts in Statistical Science. Chapman and Hall/CRC, 3 edition.

Godart, A., Anquetin, S., and Leblois, E. (2009). Rainfall regimes associated with banded convection in the cévennes-vivarais area. Meteorology and atmospheric physics, 103(1) :25–34.

Godart, A., Anquetin, S., Leblois, E., and Creutin, J.-D. (2011). The contribution of orographically driven banded precipitation to the rainfall climatology of a mediterranean region. Journal of Applied Meteorology and Climatology, 50(11) :2235–2246.

Gottardi, F., Obled, C., Gailhard, J., and Paquet, E. (2012). Statistical reanalysis of precipitation fields based on ground network data and weather patterns : Application over French mountains. Journal of Hydrology, 432âĂŞ433(0) :154 – 167.

Guillot, P. (1993). The arguments of the gradex method : a logical support to assess extreme floods. Proceedings of the Yokohama Symposium, pages 287–287.

Gupta, V. K. and Waymire, E. (1990). Multiscaling properties of spatial rainfall and river flow distributions. Journal of Geophysical Research : Atmospheres, 95(D3) :1999–2009.

Haario, H., Laine, M., Mira, A., and Saksman, E. (2006). DRAM : Efficient adaptive MCMC. Statistics and Computing, 16(4) :339–354.

Hailegeorgis, T. T., Thorolfsson, S. T., and Alfredsen, K. (2013). Regional frequency analysis of extreme precipitation with consideration of uncertainties to update {IDF} curves for the city of trondheim. Journal of Hydrology, 498 :305 – 318.

Hartigan, J. A. and Wong, M. A. (1979). Algorithm as 136 : A k-means clustering algorithm. Journal of the Royal Statistical Society. Series C (Applied Statistics), 28(1) :100–108.

Huard, D., Mailhot, A., and Duchesne, S. (2010). Bayesian estimation of intensity–duration–frequency curves and of the return period associated to a given rainfall event. Stochastic Environmental Research and Risk Assessment, 24(3) :337–347.

Iturbe, I. R. and Mejìa, J. M. (1974). On the transformation of point rainfall to areal rainfall. Water Resources Research, 10(4) :729–735.

Jeffreys, H. (1998). The theory of probability. OUP Oxford.

Kabluchko, Z., Schlather, M., and de Haan, L. (2009). Stationary max-stable fields associated to negative definite functions. Ann. Probab., 37(5) :2042–2065.

Kass, R. E. and Wasserman, L. (1996). The selection of prior distributions by formal rules. Journal of the American Statistical Association, 91(435) :1343–1370.

Kim, J., Lee, J., Kim, D., and Kang, B. (2019). The role of rainfall spatial variability in estimating areal reduction factors. Journal of Hydrology, 568 :416 – 426.

Koutsoyiannis, D. (2004a). Statistics of extremes and estimation of extreme rainfall : I. Theoretical investigation / Statistiques de valeurs extrêmes et estimation de précipitations extrêmes : I. Recherche théorique. Hydrological Sciences Journal, 49(4) :null–590.

Koutsoyiannis, D. (2004b). Statistics of extremes and estimation of extreme rainfall : II. Empirical investigation of long rainfall records / Statistiques de valeurs extrêmes et estimation de précipitations extrêmes : II. Recherche empirique sur de longues séries de précipitations. Hydrological Sciences Journal, 49(4) :null–610.

Langousis, A., Carsteanu, A. A., and Deidda, R. (2013). A simple approximation to multifractal rainfall maxima using a generalized extreme value distribution model. Stochastic Environmental Research and Risk Assessment, 27(6) :1525–1531.

Langousis, A., Veneziano, D., Furcolo, P., and Lepore, C. (2009). Multifractal rainfall extremes : Theoretical analysis and practical estimation. Chaos, Solitons & Fractals, 39(3) :1182–1194.

Le, P. D., Davison, A. C., Engelke, S., Leonard, M., and Westra, S. (2018). Dependence properties of spatial rainfall extremes and areal reduction factors. Journal of Hydrology, 565 :711 – 719.

Lebel, T. and Laborde, J. P. (1988). A geostatistical approach for areal rainfall statistics assessment. Stochastic Hydrology and Hydraulics, 2(4) :245–261.

Liu, J., Doan, C. D., Liong, S.-Y., Sanders, R., Dao, A. T., and Fewtrell, T. (2015). Regional frequency analysis of extreme rainfall events in Jakarta. Natural Hazards, 75(2) :1075–1104.

Lombardo, F., Napolitano, F., and Russo, F. (2006). On the use of radar reflectivity for estimation of the areal reduction factor. Natural Hazards and Earth System Sciences, 6(3) :377–386.

Lovejoy, S. and Mandelbrot, B. (1984). Fractal properties of rain, and a fractal model. Tellus, Series A- Dynamic Meteorology and Oceanography, 37 :209–232.

Mandelbrot, B. (1984). Les objets fractals.

Marchi, L., Borga, M., Preciso, E., and Gaume, E. (2010). Characterisation of selected extreme flash floods in europe and implications for flood risk management. Journal of Hydrology, 394(1) :118 – 133. Flash Floods : Observations and Analysis of Hydrometeorological Controls.

Mélèse, V., Blanchet, J., and Creutin, J.-D. (2019). A regional scale-invariant extreme value model of rainfall Intensity-Duration-Area-Frequency relationships. Water Resources Research, submitted.

Mélèse, V., Blanchet, J., and MoliniÃl', G. (2018). Uncertainty estimation of Intensity-Duration-Frequency relationships : A regional analysis. Journal of Hydrology, 558 :579 – 591.

Mineo, C., Ridolfi, E., Napolitano, F., and Russo, F. (2018). The areal reduction factor : A new analytical expression for the lazio region in central italy. Journal of Hydrology, 560 :471 – 479.

Miniscloux, F., Creutin, J. D., and Anquetin, S. (2001). Geostatistical analysis of orographic rainbands. Journal of Applied Meteorology, 40(11) :1835–1854.

Molinié, G. (2013). L'électrisation des orages ; La structure spatio-temporelle de la pluie à l'échelle aérologique. habilitation Ãă diriger des recherches, Université Joseph-Fourier - Grenoble I.

Molinié, G., Ceresetti, D., Anquetin, S., Creutin, J. D., and Boudevillain, B. (2012). Rainfall regime of a mountainous mediterranean region : Statistical analysis at short time steps. Journal of Applied Meteorology and Climatology, 51(3) :429–448.

Muller, A., Bacro, J.-N., and Lang, M. (2008). Bayesian comparison of different rainfall depth–duration–frequency relationships. Stochastic Environmental Research and Risk Assessment, 22(1) :33–46.

Nelder, J. A. and Mead, R. (1965). A simplex method for function minimization. The Computer Journal, 7(4) :308–313.

Nguyen, V., Nguyen, T., and Wang, H. (1998). Regional estimation of short duration rainfall extremes. Water science and technology, 37(11) :15–19.

Nhat, L. M., Tachikawa, Y., Sayama, T., and Takara, K. (2007). A simple scaling charatesristics of rainfall in time and space to derive intensity duration frequency relationships. Annual journal of hydraulic engineering, 51 :73–78.

Nicolet, G., Eckert, N., Morin, S., and Blanchet, J. (2017). A multi-criteria leave-two-out cross-validation procedure for max-stable process selection. Spatial Statistics, 22(Part 1) :107 – 128.

Norbiato, D., Borga, M., Sangati, M., and Zanon, F. (2007). Regional frequency analysis of extreme precipitation in the eastern Italian Alps and the August 29, 2003 flash flood. Journal of Hydrology, 345(3) :149 – 166.

Nuissier, O., Ducrocq, V., Ricard, D., Lebeaupin, C., and Anquetin, S. (2008). A numerical study of three catastrophic precipitating events over southern france. i : Numerical framework and synoptic ingredients. Quarterly Journal of the Royal Meteorological Society, 134(630) :111–130.

Olivera, F., Choi, J., Kim, D., and Li, M.-H. (2008). Estimation of average rainfall areal reduction factors in texas using nexrad data. Journal of Hydrologic Engineering, 13(6) :438–448.

Omolayo, A. (1993). On the transposition of areal reduction factors for rainfall frequency estimation. Journal of Hydrology, 145(1) :191 – 205.

Overeem, A., Buishand, A., and Holleman, I. (2008). Rainfall depth-duration-frequency curves and their uncertainties. Journal of Hydrology, 348(1) :124–134.

Overeem, A., Buishand, T., Holleman, I., and Uijlenhoet, R. (2010). Extreme value modeling of areal rainfall from weather radar. Water Resources Research, 46(9).

Padoan, S. A., Ribatet, M., and Sisson, S. A. (2010). Likelihood-Based Inference for Max-Stable Processes. Journal of the American Statistical Association, 105(489) :263–277.

Panthou, G., Vischel, T., Lebel, T., Quantin, G., and Molinié, G. (2014). Characterising the space–time structure of rainfall in the Sahel with a view to estimating IDAF curves. Hydrology and Earth System Sciences, 18(12) :5093–5107.

Papalexiou, S. M., AghaKouchak, A., and Foufoula-Georgiou, E. (2018). A Diagnostic Framework for Understanding Climatology of Tails of Hourly Precipitation Extremes in the United States. Water Resources Research, 0(0).

Papalexiou, S. M. and Koutsoyiannis, D. (2013). Battle of extreme value distributions : A global survey on extreme daily rainfall. Water Resources Research, 49(1) :187–201.

Papalexiou, S. M., Koutsoyiannis, D., and Makropoulos, C. (2013). How extreme is extreme ? An assessment of daily rainfall distribution tails. Hydrology and Earth System Sciences, 17(2) :851–862.

Pauli, F., Racugno, W., and Ventura, L. (2011). Bayesian composite marginal likelihoods. Statistica Sinica, 21(1) :149–164.

Pavlovic, S., Perica, S., Laurent, M. S., and Mejía, A. (2016). Intercomparison of selected fixed-area areal reduction factor methods. Journal of Hydrology, 537 :419 – 430.

Peleg, N., Marra, F., Fatichi, S., Paschalis, A., Molnar, P., and Burlando, P. (2018). Spatial variability of extreme rainfall at radar subpixel scale. Journal of Hydrology, 556 :922 – 933.

Penot, D. (2014). Cartography of the extreme rain falls and use of the SCHADEX method for ungauged sites. Theses, Université de Grenoble.

R Core Team (2019). R : A Language and Environment for Statistical Computing. R Foundation for Statistical Computing, Vienna, Austria.

Ramos, M. H., Creutin, J.-D., and Leblois, E. (2005). Visualization of storm severity. Journal of Hydrology, 315(1) :295–307.

Rantz, S. (1971). Precipitation depth-duration-frequency relations for the san francisco bay region, california. US Geological Survey, Prof. Paper, pages 237–241.

Ribatet, M., Cooley, D., and Davison, A. C. (2012). Bayesian inference from composite likelihoods, with an application to spatial extremes. Statistica Sinica, 22(2) :813–845.

Ribatet, M. and Sedki, M. (2012). Extreme value copulas and max-stable processes. Journal de la Société Française de Statistique, 153(3) :138–150.

Ribes, A., Thao, S., Vautard, R., Dubuisson, B., Somot, S., Colin, J., Planton, S., and Soubeyroux, J.-M. (2018). Observed increase in extreme daily rainfall in the French Mediterranean. Climate Dynamics.

Ruin, I., Lutoff, C., Boudevillain, B., Creutin, J.-D., Anquetin, S., Rojo, M. B., Boissier, L., Bonnifait, L., Borga, M., Colbeau-Justin, L., Creton-Cazanave, L., Delrieu, G., Douvinet, J., Gaume, E., Gruntfest, E., Naulin, J.-P., Payrastre, O., , and Vannier, O. (2014). Social and Hydrological Responses to Extreme Precipitations : An Interdisciplinary Strategy for Postflood Investigation. Weather, Climate, and Society, 6(1) :135–153.

Salvadori, G. and De Michele, C. (2001). From generalized Pareto to extreme values law : Scaling properties and derived features. Journal of Geophysical Research : Atmospheres, 106(D20) :24063–24070.

Sarhadi, A. and Soulis, E. D. (2017). Time-varying extreme rainfall intensity-duration-frequency curves in a changing climate. Geophysical Research Letters, 44(5) :2454–2463.

Schellander, H. and Hell, T. (2018). Modeling snow depth extremes in austria. Natural Hazards, 94(3) :1367–1389.

Schertzer, D. and Lovejoy, S. (1987). Physical modeling and analysis of rain and clouds by anisotropic scaling multiplicative processes. J. Geophys. Res, 92(D8) :9693–9714.

Sebille, Q., FougÃÍres, A.-L., and Mercadier, C. (2017). Modeling extreme rainfall. Spatial Statistics.

Sénési, S., Bougeault, P., Chèze, J.-L., Cosentino, P., and Thepenier, R.-M. (1996). The vaison-la-romaine flash flood : Mesoscale analysis and predictability issues. Weather and Forecasting, 11(4) :417–442.

Sivapalan, M. and Blöschl, G. (1998). Transformation of point rainfall to areal rainfall : Intensity-duration-frequency curves. Journal of Hydrology, 204(1) :150–167.

Stedinger, J. R., Vogel, R. M., and Foufoula-Georgiou, E. (1993). Handbook of Hydrology, chapter Frequency Analysis of Extreme Events. McGraw-Hill, New-York.

Stephenson, A. G., Lehmann, E. A., and Phatak, A. (2016). A max-stable process model for rainfall extremes at different accumulation durations. Weather and Climate Extremes, 13 :44 – 53.

Svensson, C. and Jones, D. (2010). Review of methods for deriving areal reduction factors. Journal of Flood Risk Management, 3(3) :232–245.

Te Chow, V. (1988). Applied hydrology. Tata McGraw-Hill Education.

Tung, Y.-k. and Wong, C.-l. (2014). Assessment of design rainfall uncertainty for hydrologic engineering applications in hong kong. Stochastic Environmental Research and Risk Assessment, 28(3) :583–592.

Van de Vyver, H. (2012). Spatial regression models for extreme precipitation in belgium. Water Resources Research, 48(9). W09549.

Van de Vyver, H. (2015). Bayesian estimation of rainfall Intensity-Duration-Frequency relationships. Journal of Hydrology, 529, Part 3 :1451 – 1463.

Van de Vyver, H. and Demarée, G. R. (2010). Construction of Intensity–Duration–Frequency (IDF) curves for precipitation at Lubumbashi, Congo, under the hypothesis of inadequate data. Hydrological Sciences Journal–Journal des Sciences Hydrologiques, 55(4) :555–564.

Varin, C., Reid, N., and Firth, D. (2011). An overwiew of composite likelihood methods. Statistica Sinica, 21(1) :5–42.

Veneziano, D. and Langousis, A. (2005). The areal reduction factor : A multifractal analysis. Water Resources Research, 41(7).

Veneziano, D., Langousis, A., and Furcolo, P. (2006). Multifractality and rainfall extremes : A review. Water Resources Research, 42(6). W06D15.

Venugopal, V., Foufoula-Georgiou, E., and Sapozhnikov, V. (1999). Evidence of dynamic scaling in space-time rainfall. Journal of Geophysical research, 104(D24) :31599–31610.

Wasko, C., Sharma, A., and Westra, S. (2016). Reduced spatial extent of extreme storms at higher temperatures. Geophysical Research Letters, 43(8) :4026–4032. 2016GL068509.

Wright, D. B., Smith, J. A., and Baeck, M. L. (2014). Flood frequency analysis using radar rainfall fields and stochastic storm transposition. Water Resources Research, 50(2) :1592–1615.

Wright, D. B., Smith, J. A., Villarini, G., and Baeck, M. L. (2013). Estimating the frequency of extreme rainfall using weather radar and stochastic storm transposition. Journal of Hydrology, 488 :150 – 165.

Yoo, C., Kim, K., Kim, H. S., and Park, M. J. (2007). Estimation of areal reduction factors using a mixed gamma distribution. Journal of Hydrology, 335(3-4) :271 – 284.

Zellner, A. (1998). Past and recent results on maximal data information priors. Journal of Statistical Research.

Zhou, Z., Smith, J. A., Wright, D. B., Baeck, M. L., Yang, L., and Liu, S. (2019). Storm catalog-based analysis of rainfall heterogeneity and frequency in a complex terrain. Water Resources Research, 0(0).

–

Modélisation multi-échelle de l'aléa pluviométrique et incertitudes associées - Application à la région des Cévennes.

La thèse présentée s'intéresse à la modélisation de l'aléa pluviométrique dans la région du Sud-Est de la France centrée sur les Cévennes. Cette région connait régulièrement des crues rapides et très localisées appelées crues éclair qui ont des impacts socio-économiques considérables. Une mesure statistique de l'aléa est la fréquence d'occurrence ou, de manière équivalente, la période de retour. La pluie étant un phénomène qui s'accumule non uniformément dans le temps et dans l'espace, l'aléa pluviométrique est une variable multi-échelle. Ainsi, cette thèse vise à en proposer une modélisation intégrée pour la région du Sud-Est de la France, c'est à dire valide pour le continuum d'échelles spatio-temporelles.

La première partie de ces travaux permet de comprendre quel cadre d'inférence est le plus adapté à cette modélisation. La seconde partie propose un modèle permettant d'exprimer l'aléa pluviométrique sur le continuum d'échelles spatio-temporelles. Enfin, le troisième partie propose un cadre de quantification multi-échelle (en temps et en espace) de fréquence d'occurrence d'un événement pluviométrique donné ainsi que la quantification des incertitudes associées.

Mots clés : Précipitation surfacique extrême ; période de retour ; Intensité-Durée-Aire-Fréquence ; Bayésien ; Région montagneuse Méditerranéene.

Multi-scale modelling of rainfall hazard and related uncertainties - Application to the Cévennes region.

This thesis aims at modelling the rainfall hazard in a mountainous region of southeastern France centered on the Cévennes massif. This region undergoes intense rainfall events leading to flash floods, which have considerable socio-economics impacts. A statistical measure of hazard is the frequency of occurrence, or equivalently the return period. Since rainfall accumulates in both time and space, rainfall hazard in a multi-scale variable. This thesis propose a generic framework for rainfall hazard modelling over the continuum of spatio-temporal scales.

The first part of this work allows to determine which is the most relevant statistical framework. The second part proposes a multi scale modelling of rainfall hazard for the region. Finally, the third part allows the multi-scale quantification of the frequency of occurrence of a given storm and of the related uncertainties.

Keywords : Extreme areal rainfall ; return period ; Intensity-Duration-Area-Frequency ; Bayesian ; Mediterranean mountaineous region.